Galaxy evolution in the William Herschel deep field

Henry Joy McCracken

McCracken, Henry Joy (1999) Galaxy evolution in the William Herschel deep field. Doctoral thesis, Durham University.

Galaxy Evolution in the William Herschel Deep Field

by

Henry Joy McCracken

January, 1999

A Thesis submitted to the University of Durham in accordance
with the regulations for admittance to the
degree of Doctor of Philosophy

Books you have read will be of use no more.
You searched for an answer but lived without an answer.

You will walk in the streets of southern cities,
Restored to your beginnings, seeing again in rapture
The whiteness of a garden after the first night of snow.

from “Youth”, by Czeslaw Milosz

Preface

The work detailed in the pages of this Thesis was carried out by the author while he was a research student at the Department of Physics, University of Durham, between July 1995 and December 1998. This work has not been submitted for any other degree at the University of Durham or at any other University.

Acknowledgements

It's the usual cast of suspects in here — friends and family, supervisors and fellow astronomers. I'll mention some of you, at least, and in no particular order: Tom Shanks, for being a continual source of ideas and er, lively discussions, and for also teaching me how to be critical in an astronomical sense; Austin, Caspar, Dave and Jon for teaching me how to be critical in a non-astronomical sense, and also for saving me from Durham at regular intervals; Nigel Metcalfe for being unfailingly English and helpful at all the right moments; David Schlegel, Ben Moore, Richard Dodson and all my other fellow bean worshippers — I couldn't have made it without the beans; Dick Fong for reminding me about the dangers of specialization — like I needed reminding; Ana Campos and Steve Gwyn for the patatas bravas and the margaritas respectively; Mister Burn for the midnight discussions about reclusive American writers; and Barbara, for the Sunday afternoons. Thanks must definitely go to my mother and father, above all — never once was it suggested that astronomy was not the ideal calling for the son of a monumental sculptor.

These three years would have been a whole lot longer without you all. Thanks.

Henry Joy McCracken, January 1999

Abstract

In this Thesis we investigate the evolutionary histories of faint field galaxies using extremely deep optical and near-infrared photometry. Our work is centred on a 50 arcmin^2 region at high galactic latitude which we call "The William Herschel Deep Field" (WHDF). In this work we describe three new near-infrared surveys of this field. In considering both this infrared data and the existing optical data, our broad aims are to increase our understanding of both the growth of galaxy clustering in the Universe and also to determine the star-formation histories of the field galaxy population. We consider our observations primarily in the context of luminosity evolution models in low density universes, but alternative scenarios are considered.

Near-infrared galaxy counts derived from our catalogues are consistent with the predictions of our models, without the need for a steep faint-end slope for the galaxy luminosity function. We find that optical-infrared colour distributions of infrared-selected galaxies in the WHDF are deficient in red, early-type galaxies. This is consistent with the predictions of evolutionary models in which these systems have a small amount of on-going star-formation.

We measure the amplitude of galaxy clustering in the WHDF for galaxies selected in optical and near-infrared bandpasses using the projected two-point correlation function. By comparing our measured clustering amplitudes with the predictions of our models we find that in *all* bandpasses the growth of galaxy clustering is approximately fixed in proper co-ordinates, again assuming a low density Universe. Finally, an analysis of errors on the correlation function measurements suggest that discrepancies between our work and those of other authors may be explained by an underestimation of statistical errors.

Contents

Acknowledgements **vii**

Abstract **ix**

Table of Contents **xi**

1 Seeing further **1**

1.1 Preliminaries 1

1.2 Some history 3

1.3 Recent developments 8

1.4 The "two cultures" – semi-analytical modelling and pure luminosity evolution 12

1.5 Plans and intentions 14

2 Surveying the WHDF in the Near-Infrared **15**

2.1 Introduction 15

2.2 Observations and data reductions 17

2.2.1 Reducing the "wide" survey 17

2.2.2 Reducing the "deep" survey 20

2.2.3 Object detection and photometry 22

2.2.4 Confusion corrections 24

2.3 Results 26
2.3.1 $K-$ band galaxy number counts 26
2.3.2 Optical-infrared colours 28
2.4 Interpretation and modelling 32
2.4.1 Outline of the models 32
2.4.2 Counts and colour distributions 38
2.4.3 $(I-K)$ distributions and extremely red galaxies 46
2.5 Conclusions and summary 49

3 Deep galaxy counts with MARTINI **52**

3.1 An introduction to adaptive optics 52
3.2 Specifics: The MARTINI Adaptive Optics System 56
3.3 Observations and data reductions 58
3.4 The deep image 61
3.5 Lessons and conclusions 65

4 Calar Alto Observations of the WHDF **67**

4.1 Introduction: a wide-field near-IR array 67
4.2 Observations and Data Reductions 69
4.3 Object detection and photometry 74
4.4 Results 76
4.4.1 $H-$ band galaxy number counts 76
4.4.2 Optical-infrared colours 81
4.5 Interpretation and discussion 84
4.5.1 Colour distributions and red outliers 84

4.6 Conclusions 90

5 Galaxy clustering in the WHDF 92

5.1 Introduction 92

5.1.1 Surveying the Universe 92

5.1.2 Deep pencil beam surveys 93

5.1.3 The growth of structure 94

5.1.4 Investigating galaxy clustering with the WHDF 96

5.2 Methods and Techniques 96

5.2.1 Catalogue generation and star-galaxy separation 96

5.2.2 Determining the angular correlation function 99

5.2.3 Modelling the correlation function 101

5.2.4 Photometric redshifts and galaxy clustering 104

5.3 Results 109

5.3.1 Measured correlations 109

5.3.2 Quantifying errors in the correlation function 120

5.4 Interpretation and discussion 126

5.4.1 Predicting $\omega(\theta)$ from the evolutionary models 126

5.4.2 The growth of clustering 129

5.4.3 Clustering of high redshift galaxies 132

5.4.4 A consistent picture? 135

5.5 Conclusions and summary 138

6 Conclusions 140

6.1 Preliminaries 140

6.2 Photometric evolution 140
6.3 Clustering evolution 141
6.4 Concluding remarks 142
6.5 Future prospects 144

Chapter 1

Seeing further

1.1 Preliminaries

The quest to see further has driven progress in astronomy throughout its long history. When Galileo turned his telescope to the night skies over renaissance Italy, man's reach increased immeasurably; suddenly moons could be seen around nearby planets, intricate details observed on Earth's satellite, objects peered at and examined which before had only been dim specks in the sky. Galileo's observations, combined with the insight of Johannes Kepler and his rigorous application of mathematical principles, displaced the Earth from its comfortable location at the centre of the Universe and sent it adrift through the cosmos. And in this century, observations of the three-degree microwave background by Penzias and Wilson provided a crucial confirmation of one promising theory for the origin of the Universe itself – and once again, this discovery was the result of our gaze extending to unexplored regions, our grasp increasing.

We are entering an exciting period for astronomy. The intersection of several crucial technologies is once again increasing dramatically our ability to see deeper and more distantly. From its opening in 1948 until only a few years ago, the Hale 200-inch telescope at Mount Palomar was the world's largest; now, in the space of a few years, almost a *dozen* telescopes will be constructed which dwarf it. And the exponential increase in computing power means that it is now possible to survey and catalogue vast swathes of the sky in a way which has never been attempted before. The first of these new surveys is just starting: in the next three years, two ambitious projects – the Sloan Digital Sky Survey and the Two Degree Field Survey – will map millions of galaxies in our local universe. Two more will extend our reach into the distant Universe which the new generation of 8-metre telescopes is just opening up to us. The amount of information produced will be immense; the Sloan Digital Sky Survey alone will produce an volume of data equivalent to that produced by mapping of the human genome.

Our aims in this Thesis are narrower than those of the grand survey projects outlined above; our project is not primarily a cosmographic one. Instead, we focus on the photometric evolution of galaxies. Our technique involves imaging as deeply as possible a single, undistinguished patch of sky located near the north galactic pole. This means it is relatively uncluttered with foreground stars. This region of sky, which we call the William Herschel Deep Field (WHDF), has over the past four years been subjected to a thorough observing campaign conducted using four different telescopes at three different observatories. The WHDF has been imaged in six different bandpasses, from the ultraviolet to the infrared, to the deepest limits possible with ground-based telescopes.

In October 1995 the Hubble Space Telescope (HST) undertook a similar project, when it integrated on one single very small field in four separate filters for over one hundred orbits. Over thirty hours of exposure time was accumulated in each of filter (which roughly corresponding to the ground-based UBRI filters), making the deepest image of the distant Universe ever taken. The immediate release of the data over the Internet prompted a concerted ground-based followup program. Now, as these words are being written, the Hubble Deep Field South – a southern deep field – has just been released to an anxiously waiting astronomical community. In this project the same program was carried out as in 1995, but this field will serve as a focus for follow-up programs conducted from the several 8m-class telescopes which are opening in the southern hemisphere. Imaging data was also taken using the HST's near-infrared camera, which we will compare with our own observations in Chapter 4.

Although both the northern and southern Hubble deep fields surpass the WHDF in terms of depth, we cover approximately a ten times larger amount of sky. Our near-infrared imaging, moreover, is currently the deepest, widest survey yet conducted, covering the entire ~ 50 arcmin^2 of the WHDF to $H < 22.5$. Our large area also permits us to investigate the clustering properties of the faint galaxy population to great depths. Together, these two topics form the main themes of this Thesis – the photometric and clustering evolution of the faint galaxy population. But before we embark on our work, we will present a brief review of the subject, and highlight some of the recent exciting advances. In this introduction we will focus on the general subject of faint galaxy evolution, and touch only briefly on the equally large topic of galaxy clustering and the growth of structure. The historical context of this subject is discussed fully in Chapter 5.

1.2 Some history

A number of articles (Ellis 1997; Koo & Kron 1992) have extensively reviewed the subject of faint field galaxies; however, progress in the field has been extremely rapid and so here we will outline some of the more recent advances which are relevant to this work, as well as providing a brief sketch of the historical framework.

With the advent of large telescopes like the Hale 200 inch, it was hoped that investigating distant galaxies might constrain the parameters of the cosmological world model – the matter density of the Universe and the Hubble constant. Sandage (1988) provides a comprehensive review of the various techniques applied. However, it was soon realised that the situation was complicated by the fact that the stellar lifetime of some of the stars in galaxies is *much shorter* than any cosmological time-span. The implication of this is that for any observations at cosmologically significant distances (and therefore at large look-back times), the evolution of the stars in the galaxies would substantially alter their luminosities. In short, ordinary galaxies are not good tracers of the underlying cosmic geometry because their luminosities change appreciably with look-back time. In attempting to determine the likely form of the cosmic geometry it was necessary to "correct" for this evolution, and "evolutionary correction" is a term which persists until this day.

Towards the end of the 1970s, the focus began to shift from determining the cosmological parameters by directly imaging faint galaxies and measuring their redshifts and towards quantifying and understanding the nature of the "evolutionary correction" itself. The theoretical groundwork for understanding the evolution of galaxies was supplied by population synthesis models which made it possible to produce quantitative predictions of the colours of galaxies at high redshift (Tinsley 1972; Bruzual & Kron 1980). In these models, changes in galaxy colour and luminosity are understood as a result of the stellar evolution of its constituent stars. By assuming an initial mass function (IMF), which describes how stars are distributed as a function of their mass, and a star formation history, one may produce an integrated colour for an entire galaxy by summing over all the stellar evolutionary tracks. As we shall see, these "pure luminosity evolution" (PLE) models have been remarkably successful in accounting for a wide variety of properties of the faint galaxy population.

4m-class telescopes combined with prime-focus photographic plates and automated image detection and photometry led to a rapid acceleration of our knowledge of the faint galaxy population and provided a rich opportunity to test these new ideas. Early works (Jones et al. 1991; Infante, Pritchet, & Quintana 1986; Shanks et al. 1984; Kron 1980; Peterson et al. 1979; Tyson & Jarvis 1979) soon identified that the number-counts of faint galaxies exceeded the predictions of simple models in which galaxy properties remain fixed with time (the "non-evolving" model). However, considerable debate existed over *how much* evolution was occurring, and over which magnitude ranges; in fact one group argued that uncertainties in the local luminosity function meant that the "non-evolving" hypothesis could not be convincingly rejected (Koo, Gronwall, & Bruzual 1993).

It was soon realised that the crucial question centered around the magnitude limit the model counts were normalised at; in order to discuss galaxy evolution we must specify with respect to *which* population one measures this evolution. Results from numerous studies of brighter ($B < 19$) galaxy counts based on data from wide-area Schmidt plates (Heydon-Dumbleton, Collins, & Macgillivray 1989; Shanks et al. 1984) emphasized this. The largest of these was the Automated Plate Measuring machine (APM) galaxy survey of Maddox et al. (1990a). Covering $\sim$ 4300deg^2, this work revealed that the slope of the galaxy counts even at these bright magnitudes was steeper than the non-evolving prediction, which led the authors to suggest that galaxy evolution was occurring at low redshift (Maddox et al. 1990c). However, by normalizing the counts at brighter magnitudes, one was then faced with accounting for a *second* steep upturn in the counts occurring at $B \sim 24$. Alternatively, normalizing at fainter magnitudes reduced the amount of evolution required (at least to $B \sim 25$) to amounts which could be explained in terms of PLE-type models. [1]

---

[1] In this work we follow the suggestions of Shanks (1989) and Metcalfe et al. (1991) and normalise the galaxy counts at intermediate magnitudes ($B \sim 18$) and seek to explain the steep slope at $B \sim 15$) by non-evolutionary process such as large-scale clustering or photographic

At the beginning of the 1980's efficient charge-coupled device (CCD) array detectors arrived, which marked a significant advance over their photographic predecessors. As a consequence of the much higher dynamic range and inherent linearity of CCDs in comparison with photographic plates, it was possible to accurately calibrate the magnitude scale at the faint end using much brighter reference stars, which had always been problematic with plate-based data. Moreover, the much higher quantum efficiencies of these electronic detectors meant that the faint limit of the galaxy counts could be extended by several magnitudes (Tyson et al. 1986; Tyson & Seitzer 1988; Metcalfe et al. 1991; Lilly, Cowie, & Gardner 1991). These works revealed a steep increase in slope the $B-$band galaxy counts at $B \sim 24$, with even steeper slopes reported in ultraviolet bandpasses. The high precision of CCD photometry made the interpretation of these works less problematic than the earlier photographically-based datasets, although the much smaller area of CCD detectors meant that field-to-field scatter amongst different works was a significant problem. With the arrival of near-infrared detectors at the start of the 1990s, another fact became clear; counts for near-infrared selected galaxy samples closely followed the non-evolving model predictions (Gardner, Cowie, & Wainscoat 1993; Cowie et al. 1994), a topic which is discussed in detail in this Thesis.

Clearly, imaging data alone was not enough to provide a clear picture of the properties and evolutionary characteristics of the faint galaxy population; redshifts were required in order to make the connection between apparent magnitudes and observed colours to rest-frame spectral energy distributions and physical luminosities. By the mid-1980s, a number of *local* redshift surveys had been conducted (Peterson et al. 1986; Metcalfe et al. 1989), and these were essential in defining the properties of the local galaxy population. But probing to fainter

---

non-linearities at bright magnitudes. This issue is discussed fully in the context of the $K-$band galaxy counts in Section 2.3.1.

magnitudes would require a new class of instrument like the Canada-France-Hawaii telescope's Multi Object Spectrograph (MOS) (Le Fevre et al. 1994) and the Low Dispersion Survey Spectrograph (Allington-Smith et al. 1994). These instruments made measuring the redshifts of several tens of galaxies simultaneously a possibility. Combined with the much higher efficiency of CCD detectors in comparison with photographic plates (at least a factor of five) it became feasible to increase the limiting magnitude of the redshift surveys to $B < 20$ and thereby allow the question to be directly addressed – where in redshift did the population of objects corresponding to the faint galaxy excess reside? Were they, as some claimed, really intrinsically faint objects at low redshift (Babul & Rees 1992; Ferguson & McGaugh 1995)? Or did they represent a population of luminous galaxies at high ($z > 1$) redshift, as required by the predictions of the luminosity evolution models (Metcalfe et al. 1991)?

The results from the early surveys (Broadhurst, Ellis, & Shanks 1988; Colless et al. 1990) were inconclusive, however. The redshift distribution from Broadhurst, Ellis, & Shanks' $20.0 < b_J < 21.5$ survey comprising 181 galaxies followed closely the predictions of the non-evolving model. The deeper survey of Colless et al. surveyed 87 galaxies to $B = 22.5$ and again found a redshift distribution which matched the non-evolving models. The $22.5 < B < 24.0$ survey using the LDSS-2 instrument (Allington-Smith et al. 1994) conducted by Glazebrook et al. (1995a) contained 73 redshifts; once again the observed redshift distribution was well matched by the non-evolving predictions. These results seemed paradoxical at it was expected that luminosity evolution would be detectable at these depths, which led to a profusion of alternative models being proposed to explain the faint blue excess. These have included luminosity-dependent luminosity evolution (Broadhurst, Ellis, & Shanks 1988) or significant density evolution (Rocca-Volmerange & Guiderdoni 1990).

The $I-$ selected Canada-France redshift survey (CFRS) provided the first complete survey spanning a large baseline in redshift ($0 < z < 1$) with substantial numbers (~ 1000) of galaxies (Lilly et al. 1995a). A work of this size allowed for the first time evolution to be characterised *within* the survey, and without reference to any external datasets, with all their attendant problems. By segregating their sample by redshift, colour and luminosity, Lilly et al. (1995b) were able investigate the evolution of the luminosity function to $z \sim 1$. Their results indicated that red-selected luminosity functions showed little evolution in either number density or luminosity from $z = 0$ to $z = 1$. However, the blue-selected luminosity functions showed ~ 1 mag of brightening in the $0.2 < z < 0.5$ interval. This work was complemented by that of Ellis et al. (1996), who investigated evolution of the luminosity function with a sample of 548 galaxies limited at $19.7 < b_J < 22.0$. They rejected a luminosity function which is constant with redshift and moreover found (as LeFevre et al. (1996) did) that the bulk of the changes occur in the subsample of their galaxies which have strong [OII] emission.

These studies of luminosity function changes with redshift address a very important question – does number density evolution occur? PLE models are number conserving; the total numbers of galaxies remains fixed. Density evolution would corresponds to a change in ϕ^*, the normalisation of luminosity function, whereas luminosity changes result in a change in L^*. However, the statistical nature of faint galaxy studies means that the changes observed in the CFRS and AUTOFIB luminosity functions could be interpreted *either* as density or luminosity evolution.

1.3 Recent developments

In the past two years events have progressed rapidly, with some of the most important contributions being made by the first of the large aperture telescopes, the Keck I and II, which have proved invaluable in extending the spectroscopic limit to $B \sim 24$ and $K < 20$ using the high spectroscopic throughput of the Low Resolution Imaging Spectrograph (Oke et al. 1994). The Keck redshift survey of Cowie, Songaila, & Hu (1996) reached depths of $B < 24$ with $\sim 100\%$ completeness *and revealed a high-redshift component to the redshift distribution.* With this work it became apparent that many of the objects which Glazebrook et al. (1995a) had missed in their survey (which was 70% complete) were probably [OII]-strong star-forming galaxies at high redshifts which had not been detected because of the poor blue response of the LDSS-2 spectrograph.

The high angular resolution of the HST has provided insight into the morphology of the faint galaxy population. Images from the Medium Deep Survey (Griffiths et al. 1994), a parallel observing program conducted with the HST's Wide Field/Planetary Camera, has allowed the construction of galaxy counts subdivided by type to $I < 22$ (Glazebrook et al. 1995b; Driver, Windhorst, & Griffiths 1995); similar studies have been carried out with the Hubble Deep Field to $I < 25$ (Abraham et al. 1996; Driver et al. 1998). All these authors conclude that "irregular" or "peculiar/merger" galaxy types dominate the faint galaxy population, but identifying these objects with their local counterparts is not a straightforward affair. A number of effects contribute to this, not the least of which is the bandpass-shifting effect arising as consequence of the high redshift of the sources.

Other morphological studies have concentrated on identifying changes in structural parameters (for example, disk scale lengths or central surface brightnesses) in spectroscopically identified galaxies: Schade et al. (1995) investigated 32 galaxies from the CFRS with secure redshifts in the range $0.5 < z < 1.2$ and claimed to have detected ~ 1 mag of surface brightness evolution in spiral galaxy central surface brightness at these redshifts. Similar results are claimed for a much larger sample of ~ 300 galaxies drawn from Canadian Network for Observational Cosmology (CNOC) survey and imaged at high resolution from ground-based telescopes (Schade et al. 1996a). These results, whilst interesting, may be subject to surface-brightness selection effects which can make interpretation of high-redshift features problematic. More recently, Lilly et al. (1998) and Brinchmann et al. (1998) investigated morphology at intermediate redshifts using a large sample of ~ 400 galaxies with spectroscopic redshifts. They found that the disk scale length stays roughly constant to $z \sim 1$, and speculate that the observed changes in the galaxy luminosity may be due to smaller galaxies.

Kinematic studies of disks at intermediate redshifts have also been attempted (Simard & Pritchet 1998; Vogt et al. 1996). By probing the Tully-Fisher (TF) relation at intermediate redshifts and comparing observations to local values, these studies hope to investigate luminosity evolution *directly*, on a galaxy-by-galaxy basis. However, once again the results appear to be dependent on sample selection; Simard & Pritchet, selecting [OII] emitters for their sample objects, find they are ~ 1.5 magnitudes brighter than expected from local TF samples. The Vogt et al. sample, however, was selected without regard to [OII] strengths; they find only ~ 0.6 mag brightening to $z \sim 1$.

Perhaps the most exciting discovery in the past two years has been the identification of a population of "normal" star-forming galaxies at $2.5 \lesssim z \lesssim 3.5$ (Steidel et al. 1996). These objects have been located using Lyman-break imaging, a technique which is described in Section 5.2.4; briefly, objects are located on the basis of having very red ultraviolet-optical colours, and optical-optical colours which are approximately zero. Early works indicated correctly that the fraction of the galaxy population at $z > 3$ was probably small (Guhathakurta, Tyson, & Majewski 1990). In recent years, the development of CCD cameras with high UV quantum efficiencies led to the direct detection of these objects

(Steidel & Hamilton 1993). Most important of all, spectroscopic follow up on the Keck telescopes has been able to confirm these photometrically estimated redshifts (Steidel et al. 1996). Several hundred of these galaxies have now been identified. The first and most controversial finding stemming from their discovery centered around the estimation of the star-formation rate at these redshift ranges and comparing it with values inferred from lower-redshift samples like the CFRS (Madau et al. 1996).

Madau et al.'s star-formation history diagram delineated a picture where the star-formation rate rose steeply in the redshift range $0 < z < 1$, reached at peak at $1 < z < 2$, and then steadily declined at $z > 2$. Theorists (White & Frenk 1991) hailed this as a vindication of their models of galaxy formation. However, it soon became apparent that the situation at $z > 2$ was less than straightforward; calculations of the UV luminosity density (and therefore star-formation rate) depend sensitively on assumptions concerning the amount of high redshift dust (Campos & Shanks 1997; Metcalfe et al. 1996). Finally, a very recent paper (Steidel et al. 1998b) has extended the dropout technique to redder wavebands and thereby higher redshifts. From a study of 244 galaxies (48 with spectroscopic confirmation) in the redshift range $3.61 < z < 4.81$ they concluded that was *no evidence* for the steep decline in star-formation density seen in earlier studies. However, the importance of this result is tempered somewhat by the small fraction of cosmic time this redshift interval represents and the correspondingly small contribution to the total metal production of the Universe. Shanks et al. (1998) point out that a steeply increasing star-formation rate $0 < z < 1$, follwed by a near-constant star-formation rate at $z > 1$, is consistent with exponential star-formation histories commonly found in PLE models.

1.4 The "two cultures" – semi-analytical modelling and pure luminosity evolution

The pure luminosity evolution models mentioned in the previous section have proved extremely resilient when confronted with an increasing variety of observations. Remarkably – for such a simple class of model – they successfully match a broad range of observations and can provide important insight into the evolutionary histories of the faint galaxy population. Most of the observations presented in this paper will be discussed primarily in the context of these models. However, in the thirty years since the principles of stellar evolution were elucidated by Tinsely and others, our knowledge of the physical processes at work in the Universe have expanded immensely, and alternative and more physically motivated schemes for modelling the evolution of galaxies have been developed.

Large numerical simulations (which are discussed in Chapter 5) have successfully followed the growth of structure in the Universe as traced by dark matter haloes from the Big Bang to the present day. In these models, Gaussian perturbations in the density field of the early Universe grow under the influence of gravity into rotating aggregates of dark matter. Onto these objects baryonic matter falls and is shocked, heated, and eventually forms stars over a timescale governed by how rapidly the gas can cool. Moreover, these objects are not isolated systems; over the course of cosmic time they undergo numerous merging events with similar systems, in the end producing a final halo which is many times more massive than its many progenitors. This process has been termed "hierarchical merging". However, fully modelling this sequence of events in a numerical simulation is an unrealistic proposition, because of the extremely large dynamic range and high force resolution which would be required to trace each halo; this would tax the capabilities of even the world's largest computers. Furthermore, the exact physics governing the formation of stars and galaxies is not fully understood and would be difficult to specify fully in a purely numerical simulation.

There is, however, an easier way: by using the formalism of Press & Schechter (1974) one may compute the distribution of halo masses for a given final halo mass. The extensions to the model (Bower 1991; Bond et al. 1991) allows the use of Monte-Carlo techniques to compute sets of *merger trees* containing a distribution of sizes for each of the final halo masses, and follow them from their origin at high redshift to the present day. Next, for each halo of a given mass and circular velocity one may then apply several *analytic* scaling relations which describe how much star-formation occurs over the history of the merger tree. Finally, the addition of a stellar population synthesis model allows one to calculate observable quantites such as luminosities and colours. "Mock catalogues" may then be drawn from this simulation based on any desired selection criterion in order to make comparisons with observations.

This semi-analytic model of galaxy formation has been described in detail in several papers (Cole et al. 1994; Cole 1991; White & Frenk 1991; White & Rees 1978). More recently it has been applied to several specific problems, for example galaxy counts (Baugh, Cole, & Frenk 1996; Kauffmann, Guiderdoni, & White 1994), Lyman-break galaxies (Baugh et al. 1998b) and galaxy clustering (Baugh et al. 1998a; Kauffmann et al. 1998). Typically, the model parameters are adjusted so they correctly reproduce the observed $B-$ and $K-$ band luminosity functions. Overall, the most significant difference between these models and their PLE predecessors is that galaxies are assembled relatively recently and more gradually, in the redshift range $1 < z < 2$. As we shall see, these differences lead to significant discrepancies between PLE and semi-analytical models in certain key areas, such as the timescale for the formation of field ellipticals and the redshift-distributions of $K-$ selected galaxies. The pure luminosity evolution model still maintains the virtue of simplicity over its semianalytic successors.

However, the greater predictive power of the new models of galaxy formation may ultimately be more successful when the model practitioners succeed in reducing further the number of free parameters used to describe their models

1.5 Plans and intentions

In the course of this Thesis we will present data which will allow us to investigate the evolution of faint field galaxies. This data consists primarily of deep imaging data collected in five different bandpasses. Using our near-infrared datasets, we will investigate the star-formation history of field ellipticals. By investigating the clustering evolution of galaxies in *all* bandpasses we will attempt to investigate the redshift distributions of galaxies in our catalogues to the faintest limits we measure, and also to investigate the growth of structure as traced by the galaxies in the WHDF.

Chapter 2

Surveying the WHDF in the Near-Infrared

2.1 Introduction

In this Chapter we present near-infrared observations of the William Herschel Deep Field, and combine this data with our ultra-deep optical observations. Limiting magnitudes are given in Table 2.1. Near-infrared observations have many advantages which are oft-quoted in the literature; among them, the insensitivity of the $k-$ correction to type or star-formation history at intermediate redshifts is perhaps the most relevant in a cosmological setting.

As described in the Introduction, we consider our observations in the context of pure luminosity evolution (PLE) models. Recently, additional support for these models has come from fully complete, blue-selected, redshift surveys (Cowie, Songaila, & Hu 1996) which have revealed the presence of an extended tail in the redshift distribution, partially resolving the paradox that non-evolving models could be used to fit the results of the early faint redshift surveys (Glazebrook et al. 1995c; Broadhurst, Ellis, & Glazebrook 1992). These luminosity evolution models are able to reproduce all the observable quantities of the faint

Table 2.1: Photometric Limits of the Herschel Deep Field.

Filter	U	B	R	I	K
Limit (3σ)	26.8	27.9	26.3	25.6	20.0/22.75
Area (arcmin^2)	48.5	48.5	48.5	53.0	47.2/1.78

field galaxy population (counts, colours, redshift distributions) at least for low Ω_0 Universes and within current observational uncertainties. High Ω_0 Universes can be accommodated by the model if we add an extra population of low luminosity galaxies with constant star-formation rates which boost the counts at faint ($B > 25^m$) magnitude levels (Campos 1997). In the PLE model, galaxies form monolithically at high redshift. Changes in luminosity and colour after the formation event are modelled with stellar population synthesis models. $K-$ selected galaxy samples, at least until $K \sim 20$, are expected to be dominated by early-type galaxies; therefore, changes in optical-infrared galaxy colours are particularly sensitive to evolution of this galaxy class. By investigating near-infrared number counts and colour distributions we can potentially address questions concerning the formation and evolution of elliptical galaxies.

The two surveys presented here are complementary. The "wide" survey covers a large, ~ 50 arcmin^2 area to a shallow, $K(3\sigma) = 20^m$, depth, whilst the "deep" survey covers a much smaller area of ~ 1.8 arcmin^2 to a much fainter $K(3\sigma) = 22.75^m$ limiting magnitude. In combination, both surveys provide a $K-$ limited sample extending from $K = 16^m$ to $K = 22^m.75$.

This Chapter is organized as follows: Section 2.2 describes the data reduction techniques used in both the "wide" and the "deep" surveys; in Section 2.3 number counts and colour distributions for our both data sets are presented; in Section 2.4 we discuss these results in terms of our modelling procedure; and finally, in Section 2.5 we summarize the main conclusions we draw from our work.

2.2 Observations and data reductions

2.2.1 Reducing the "wide" survey

The observations were made over four nights in July 1995 at the 3.8m United Kingdom Infrared Telescope (UKIRT) using the IRCAM3 near-infrared detector with a standard $K-$ (2.2 μm) filter. Conditions were photometric on two of the four nights. The mean seeing was $\sim 1''$ FWHM. The centre of the region we imaged, RA 0h 19m 59s Dec $+0^o\ 4'\ 0''$ (J2000), corresponds to the centre of our deep optical fields which are described in Metcalfe et al. (1998). For this region we have imaging data complete to the limiting magnitudes listed in Table 2.1 The observations were made at the 4.2m William Herschel and the 2.5m Isaac Newton telescopes (WHT and INT hereafter) and cover approximately ~ 50 arcmin^2. These data sets greatly increase the utility of our $K-$ observations. Our data reduction technique for both surveys follows the methods outlined in Gardner (1995).

The IRCAM3 detector, a 256×256 element InSb chip, has a pixel scale of $0.286''$ and consequently each image covers only ~ 1.5 arcmin^2. For this reason we observed a mosaic of 6×6 frames which completely overlapped the previously-observed optical fields. As a partial aid to registration, each sub-field overlapped its neighbour by ten pixels.

The entire mosaic was observed in each pass for two minutes at each sub-raster, and offset slightly for each observation from the previous pointing. In total, the entire survey area was covered fifteen times, giving a total integration time at each sub-raster of 30 minutes. The short exposures at each of the sub-rasters is an unavoidable consequence of high near-infrared sky brightness.

Preparation of the final image can be divided into two main sections –

removing the instrumental signature (sky subtraction and flat-fielding) and registration and stacking of the calibrated images.

Firstly, a dark frame is subtracted from each night's images, calculated from the median of the dark frames taken that particular night. Next, the images are sorted in order of time of exposure. Then, a *running sky* is constructed. This running sky consists of the median of the six images (three before, and three after) nearest in time to the frame being processed. This is necessary as the sky background varies on exceedingly short time-scales (i.e., under 30 minutes). This running sky is then *subtracted* from the current image and the procedure repeated for all the images in the mosaic. Next, for each night a "superflat" is constructed by medianing together *all* the observations for that night. (The superflat is necessary to correct for the pixel-to-pixel gain variations in the detector, whereas the "running sky" image corrects for the varying additive contribution of the sky level). Each image is then divided by the superflat after sky subtraction.

Once all the images have been dark- and sky-subtracted and flat-fielded they are arranged into groups which contain each pointing on the same part of sky (there are fifteen images – from each of the fifteen passes in the mosaic – in each of the 36 groups). Each pointing is slightly offset from the previous one and as a consequence must now be re-aligned and combined. This was accomplished using the task IMALIGN in IRAF (a cross-correlation technique was tried, but it was found that the signal in each of the two-minute exposures was too low to produce a satisfactory result). This task operates by means of a marginal centroiding algorithm; one picks a set of pointings for one pass in the mosaic and then marks objects on each of the subrasters in that pass. The program then attempts to locate these objects on subrasters from successive passes in the mosaic and uses them to determine offsets between each pass. This method was found to work on all of the 36 subrasters, except for two cases where there were no sources visible. In these cases the shifts calculated from adjacent subrasters were used. Finally, the images were shifted and averaged together using the IRAF IMCOMBINE task.

Next, masks were constructed from each of the stacked images by flagging all pixels more than 3σ from the sky background. This is necessary as bright sources present in each of the individual exposures will affect the flat-fields (this is visible as a series of dark patches in the stacked images). The masks constructed for each of the stacked images were then un-shifted so they matched each of the fifteen images which make up the thirty-six stacks. Then the self-flattening procedure outlined above was repeated, but using the masks to remove bright sources from each of the images during the construction of the running flat. Then the alignment and stacking procedure was repeated to produce a final set of stacked images.

The next (and most difficult step) involved arranging the 36 stacked subrasters into a single image. This was accomplished by a two-step procedure. First, on each of the 36 subrasters three images were located which also appear on the $B-$ band frame (these data are described in Metcalfe et al. (1998); as this is an extremely deep image almost all the images present in the stacks also appear in the $B-$ band frame.) Next the second-order (i.e., translation, rotation, scale-change) polynomial transformation between the $K-$ band frame and the $B-$ band frame was determined for all the subrasters using the IRAF task GEOMAP. All rotations and magnifications calculated for each of the subrasters were examined and those that were divergent from the median value were discarded and re-measured. These median values for the image rotation and magnification were then fixed for all the subrasters and the transformation recomputed. This gives a final list of offsets for the centres of each of the 36 subrasters in the $K-$ band image. To produce the final image, 36 blank images the size of the entire field were produced; onto each of these images each of the stacked subrasters was placed at the correct position as determined from the transformation process. These 36 images were then median combined. The final image, after trimming, covers an area of 47.2 arcmin^2, overlapping our WHT deep optical fields. We calibrated this data by repeatedly ($\sim$ 30 times) observing the faint UKIRT Standards (Casali & Hawarden 1992) each night at a range of airmasses. Fortuitously, as the mean airmass of the standards and of the program field was approximately the same, no airmass correction was necessary.

2.2.2 Reducing the "deep" survey

Observations for the "Deep" survey were made over six nights in 1994 September at UKIRT using IRCAM3 with a $K-$ band filter. Conditions were photometric during the first two nights, and the remainder of the data was scaled to the photometry of bright objects in the field made on those nights. The seeing ranged from $0.8''$ to $1.4''$. The total observing time on the field was just over 100 ksec (27.9 hours), and was made up of 838 individual exposures of 120 seconds each. Each individual exposure was made up of 12 co-adds of 10 seconds each. The telescope was dithered using the offset guide camera in a diamond pattern of 13 positions, each position separated by $5.25''$ in both Right Ascension and Declination. Data reduction proceeded generally in the manner described above. Dark frames were made several times each night, and were subtracted from the images. A running sky was constructed, using the median of 12 images (six before and six after). The running sky was subtracted (after applying the two-pass object masking system described above), and a "superflat" was constructed for each night and divided into the data.

The input dither pattern was recovered and adjusted by a centroid of the brightest object in the field. The data taken each night were shifted and co-added.

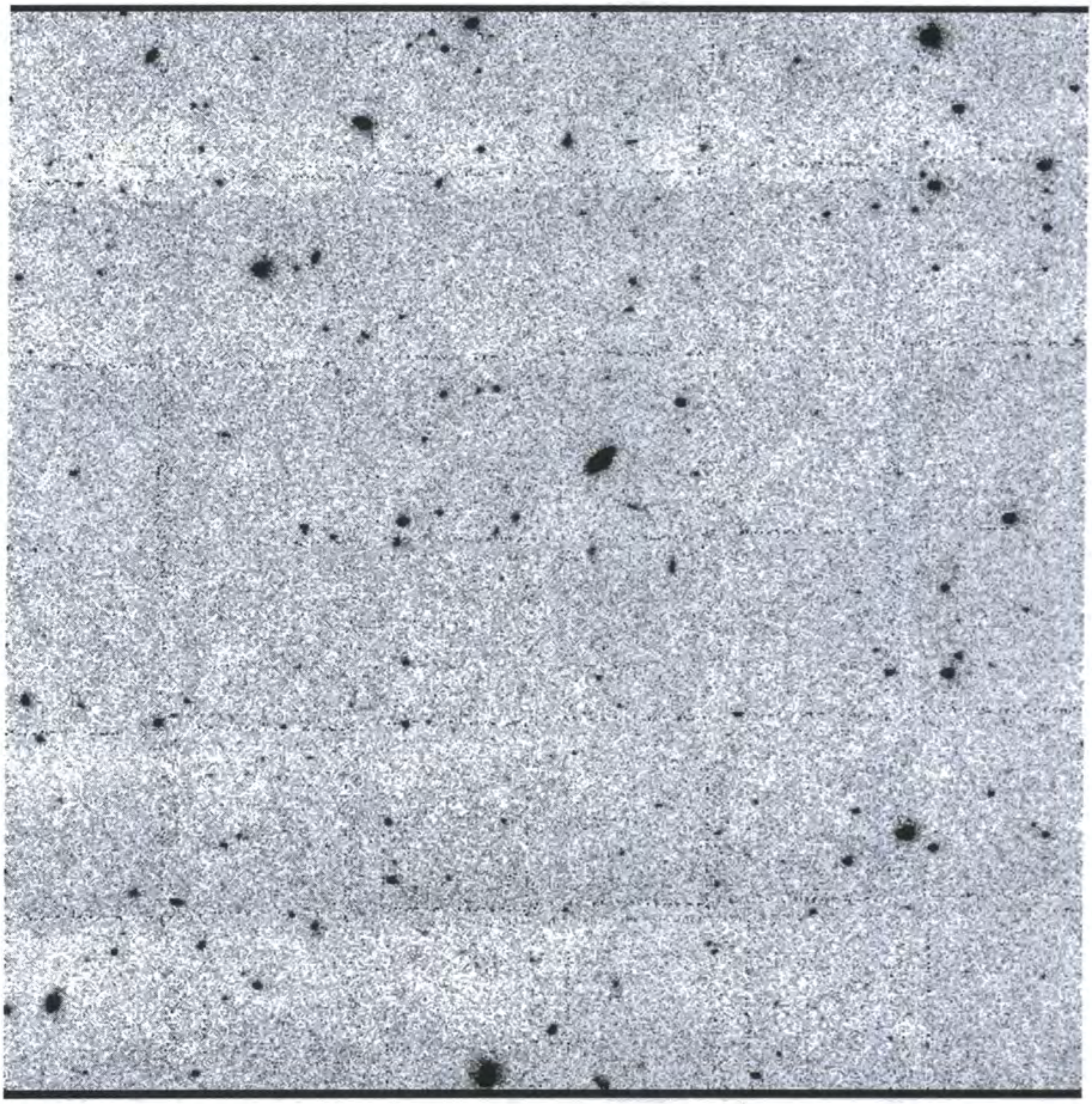

Figure 2.1: An greyscale image of the final reduced wide-field K- image. This image has a scale of $0.286''$ pixel^{-1}, and covers (6.9×6.9) arcmin^2. Before object detection and photometry was carried out on this image, residual sky gradients were removed and the image binned up 2×2.

The photometry of each night's data were scaled to that of the photometric first two nights (which were themselves consistent). The final image covers an area of 1.78 arcmin^2, and has a limiting depth of 3σ (inside 2 FWHM)= 22.75. The deep field is centred at 00 19 59.6 +00 02 56 (1950.0) and covers $81''$ square (140x140 0.58" pixels).

2.2.3 Object detection and photometry

For both the deep and wide images we use the same prescription for object detection and photometry as in our optical studies (Metcalfe et al. 1995; Metcalfe et al. 1998). Note that to improve the reliability of image detection both images were binned 2×2 (IRCAM3's $0.286''$ pixels, combined with median seeing of $\sim 1''$ FWHM mean that our images are oversampled). We fit the sky background approximately with a 3rd order polynomial and then subtract it from the frame. Deep isophotal image detection is then undertaken (to a magnitude about 1^m deeper than the 3σ limit for the frame – see column one of Table 2.2) and the objects removed from the frame (and replaced by a local sky value). The resulting image is heavily smoothed (with several passes with box smoothing up to 10 pixels on a side) and then subtracted from the original. The result is an extremely flat image on which the isophotal detection is then rerun. At this stage, in order to reduce false detections, any images within a few pixels (depending on image scale) of one another are recombined into one. A Kron-type magnitude (Kron 1980) is then calculated for each image using a local sky value. This is essentially an aperture magnitude calculated to mR_k, where R_k is the Kron radius and m is the multiplying factor given in Table 2.2. [1] It is necessary to set a minimum aperture equivalent to that for an unresolved object, and to correct to apply a

---

[1] The Kron radius, R_k, is defined as $\int_0^\infty rI(r)/\int_0^\infty I(r)$, where $I(r)$ represents the radial intensity profile of the source. In practice, the integration is not carried out infinitely far, but to some fixed fraction above the sky level; in this work it is 1%.

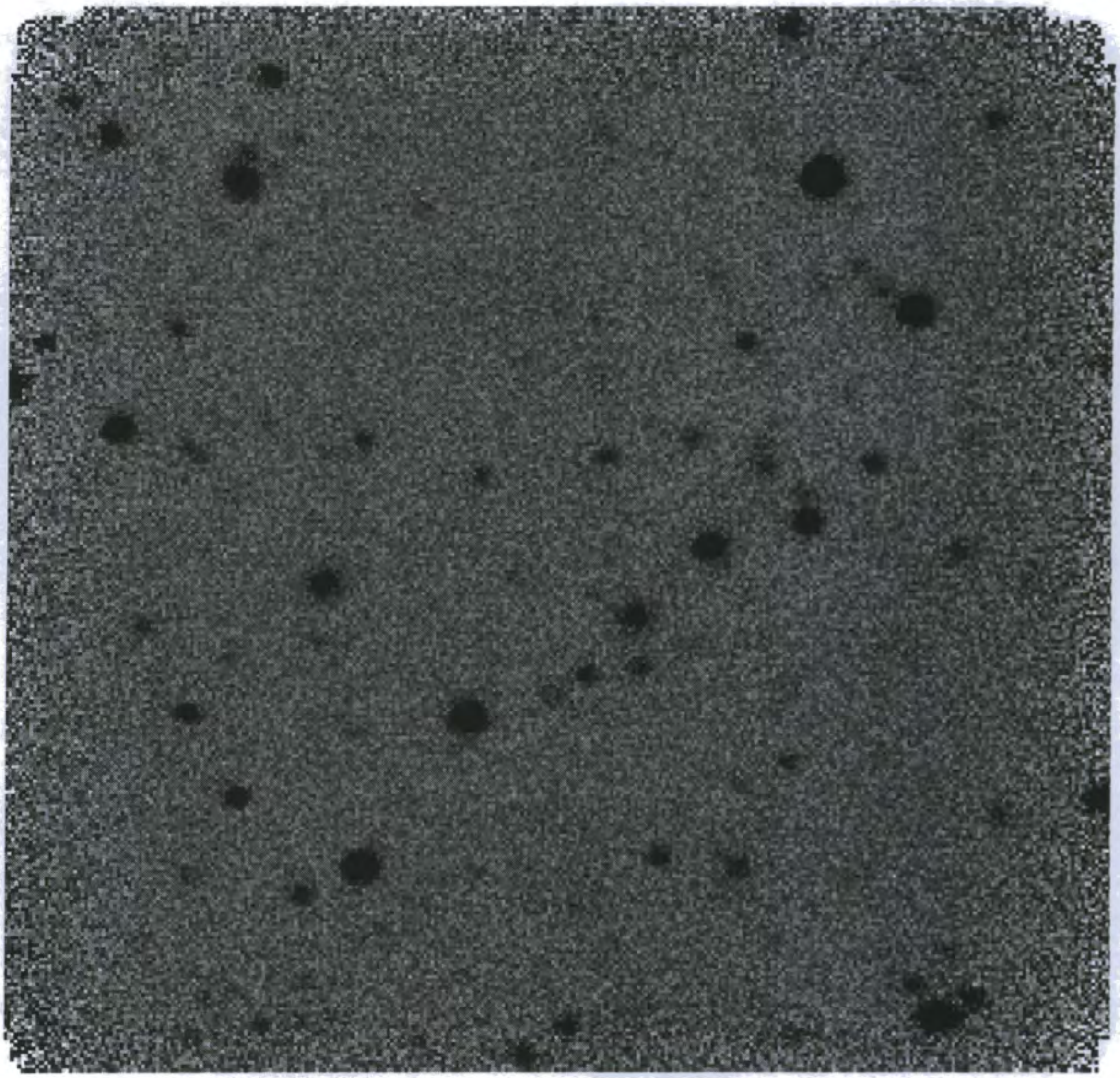

Figure 2.2: An greyscale image of the ultra-deep $K-$ IRCAM-3 image. This image has a scale of $0.286''$ pixel^{-1}, and covers ~ 1.5 arcmin^2.

Table 2.2: Detection and measurement parameters used in both surveys.

Frame	Limiting isophote ($\mathrm{mag/arcsec^2}$)	Limit (K mag)	Min. radius ($''$)	Kron factor	Correction (mag)
Deep K	24.50	23.50	1.25	1.40	0.32
Wide K	21.50	22.00	1.35	1.50	0.25

correction to total magnitude. These are also listed in Table 2.2. A more detailed discussion of this technique is given in Metcalfe et al. (1991).

2.2.4 Confusion corrections

The deeper the ground-based number-counts are extended the more important the corrections for confusion become. This is of particular relevance for the deep K-band data. To make an estimate of the completeness of our counts on this frame we have added numerous artificial stars of various known magnitudes to the real data frame and then reanalysed the resulting images using the normal data reduction procedure. We then compare the measured magnitudes with those which we input. Table 2.3 gives the mean magnitudes, scatter, and detection rate for these stars. Note that an image is considered undetected if it is merged with another image and the combined brightness is a factor two or more greater than the true magnitude, or if it is not found within ±2 pixels of its true position. As expected the detection rates in the real data drop as the magnitude falls. This is almost entirely due to objects being merged with other, brighter objects—isolated objects are recovered with almost 100% efficiency. Note, however, that the mean recovered magnitudes are close to the true values. Although most objects at the limit of our data are galaxies, they are in general close to being unresolved, and so we correct our counts by the detection rates implied by our artificial stars.

Due to the much wider mean separation between objects, the shallower $K-$band data do not suffer from confusion, and no correction is made.

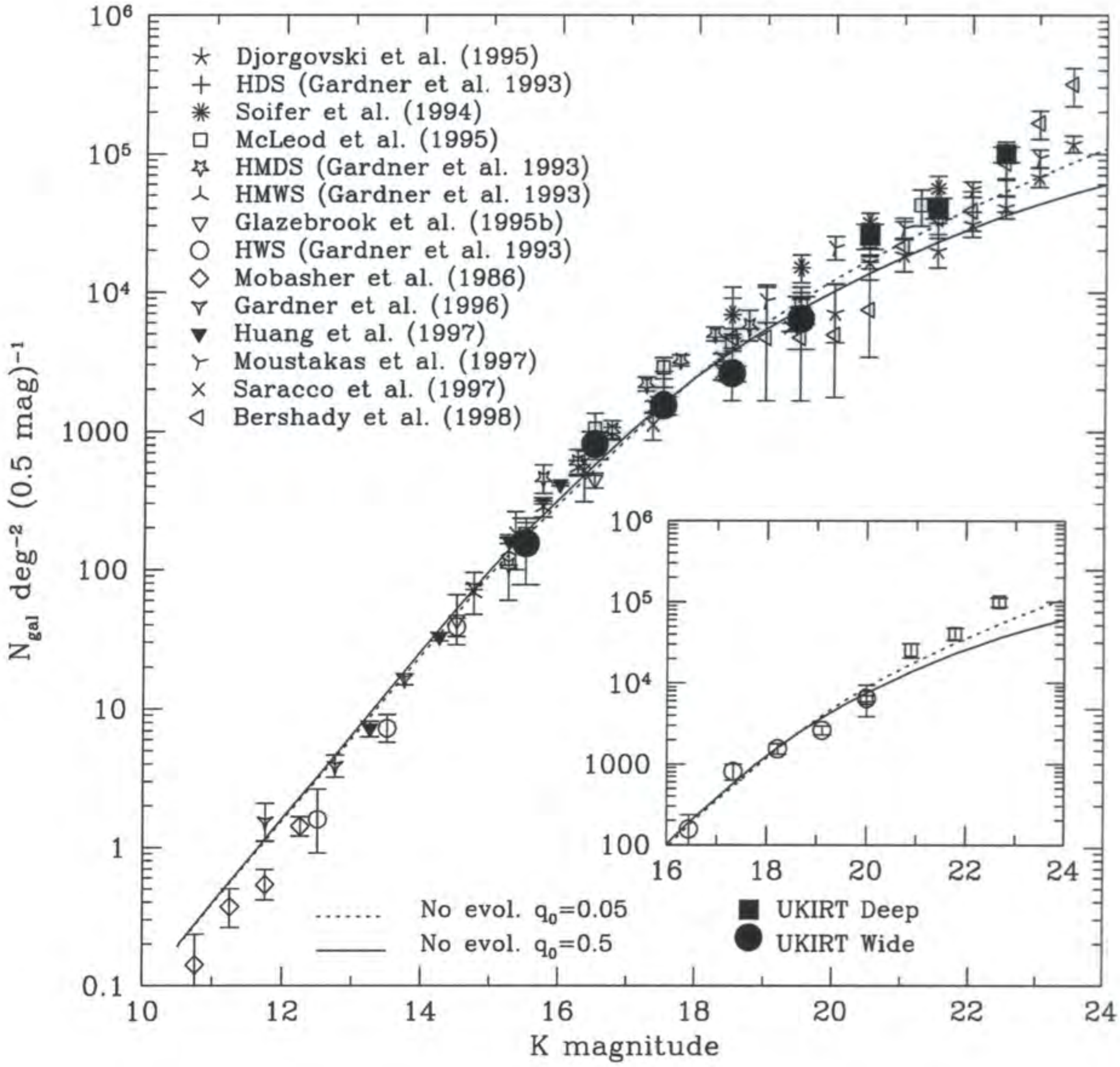

Figure 2.3: Differential galaxy number counts in half-magnitude intervals as a function of $K-$ limiting magnitude as measured from our UKIRT wide survey (filled circles) and from our UKIRT deep survey (filled squares). Also plotted is a compilation of published $K-$ band number counts and the predictions of the two non-evolving models described in the text for $q_0 = 0.05$ (dotted line) and $q_0 = 0.5$ (solid line). Error bars are calculated from the number of galaxies in each magnitude bin using Poisson $\sqrt{n}$ counting statistics. The inset shows the number counts from both surveys (this time with open symbols and without the counts from the literature) compared to the non-evolving predictions.

Table 2.3: Results of adding artificial stars to the deep K data.

True magnitude	Measured magnitude	Detection rate (%)
20.75	20.70 ± 0.17	90
21.25	21.22 ± 0.21	88
21.75	21.76 ± 0.26	85
22.25	22.36 ± 0.36	76
22.75	22.83 ± 0.37	51

2.3 Results

The final "wide" catalogue contains 298 galaxies to a $K(3\sigma) = 20.0^m$ over an area of 47.2 arcmin^2. The deep catalogue contains 86 galaxies to a $K(3\sigma) = 22.75^m$ over an area of 1.8 arcmin^2.

2.3.1 $K-$ band galaxy number counts

Number counts derived from both our catalogues are presented in Figure 2.3, which shows our data (with error bars calculated using Poisson counting statistics) and a compilation of published number counts. At bright magnitudes ($16^m < K^m < 20^m$) we agree well with the counts from the literature, whereas at fainter magnitudes ($20^m < K < 22^m$) our data favours the higher counts found by Bershady, Lowenthal, & Koo (1998) as opposed to the lower counts measured by Djorgovski et al. (1995). Bershady, Lowenthal, & Koo find that the aperture corrections employed by Djorgovski et al. (1995) results in an overestimation of the depths of the latter survey by $\sim 0.5^m$. Applying the same correction as used in Bershady, Lowenthal, & Koo makes Djorgovski et al.'s results consistent with BLK's, and, therefore, ours.

It is worth noting that in our last bin, as in Bershady, Lowenthal, & Koo, our counts are only approximately 50% complete and therefore subject to large corrections. Furthermore, given the small areas of surveys at this magnitude level (where areas covered are typically ~ 1 arcmin^2) it is also possible that cosmic variance could account for the large observed field-to-field variations between the different groups.

Considering the slope of our number counts, we derive a value of $d(\log N)/dm = 0.37 \pm 0.03$ (1σ errors) over the magnitude range covered by both wide and deep catalogues (namely, $K \sim 16 - 24$). This value is in good agreement with $d(\log N)/dm = 0.36 \pm 0.02$ found by (Bershady, Lowenthal, & Koo 1998). We do not find the count slope for the deeper survey to be significantly different for the shallower one (however, as pointed out by Gardner, Cowie, & Wainscoat (1993) the compiled $K-$ band number counts show a slope change at $K \sim 17$).

On Figure 2.3 we also plot the predictions of two non-evolving galaxy count models: one with deceleration parameter $q_0 = 0.5$ (solid line) and one with $q_0 = 0.05$ (dotted line). Both models give a good fit the observations over at least eight magnitudes. This non-evolving model was computed from the $k-$ corrections of Bruzual & Charlot (1993) and the $z = 0$ luminosity function parameters given in Table 2.4. These luminosity function paramters are derived from the Durham-AAT Redshift Survey (DARS,Broadhurst, Ellis, & Shanks (1988)). To compute $K-$ band number we transform M_B^* to M_K^* using rest-frame $(B-K)$ colours (also given in Table 2.4). Our models are normalized at $B \sim 18^m$. As we and others have noted before (Metcalfe et al. 1991; Shanks 1989), normalizing galaxy counts at brighter ($B \sim 16^m$) magnitudes requires that substantial amounts of evolution must take place at relatively low ($z < 0.1$) redshift. Conversely, by normalizing at $18^m < B < 20^m$ we allow a better fit at intermediate magnitudes and reduce the amount of evolution required to fit the counts at fainter magnitudes, but over-predict counts at brighter magnitudes.

Could substantial galaxy evolution be occurring at these redshifts? Bright,

$K < 20^m$ samples are dominated by early-type galaxies. Morphologically-segregated number counts from the Medium Deep Survey (Griffiths et al. 1994) and the Hubble Deep Field (Williams et al. 1996) indicate that counts for elliptical galaxies at intermediate magnitude levels ($18^m < I_{816W} < 22^m$) follow the predictions of a non-evolving model (Driver et al. 1998; Driver, Windhorst, & Griffiths 1995; Glazebrook et al. 1995b). This would argue against an evolutionary explanation for the steep slope observed in the range $10^m < K < 22^m$. We are then faced with finding an alternate explanation for the number counts' under-density; one suggestion comes from the findings of Metcalfe, Fong, & Shanks (1995) and Bertin & Dennefeld (1997) who both show how scale errors (i.e., non-linearities) in the APM photometry of Maddox et al. (1990c) could result in anomalously low galaxy counts at brighter magnitudes in $B-$ selected surveys. Another suggestion is that our galaxy may reside in a locally under-dense region of the Universe (Shanks 1989); however, to produce the observed discrepancy in the number counts would require that this void would be $\sim 150h^{-1}$ Mpc, and have an under-density of $\sim 30\%$; fluctuations on this scale are difficult to understand in terms of current cosmological models and also measured large-scale bulk flows. Some evidence for a local void has come from studies of peculiar velocities of type Ia supernovae (Zehavi et al. 1998) although the size of the void they detect ($\sim 70h^{-1}$ Mpc) is not large enough to explain the low number counts.

2.3.2 Optical-infrared colours

Figure 2.4 shows the $(B-K)$ *vs* K colour-magnitude diagram for galaxies in both the "wide" (open triangles) and the "deep" survey (open circles). Additionally the median $(B-K)$ colour computed in one-magnitude bins is shown (filled squares) and compared to the values given in Gardner, Cowie, & Wainscoat (1993) (filled triangles). Error bars on the median colours were calculated using a bootstrap resampling technique.

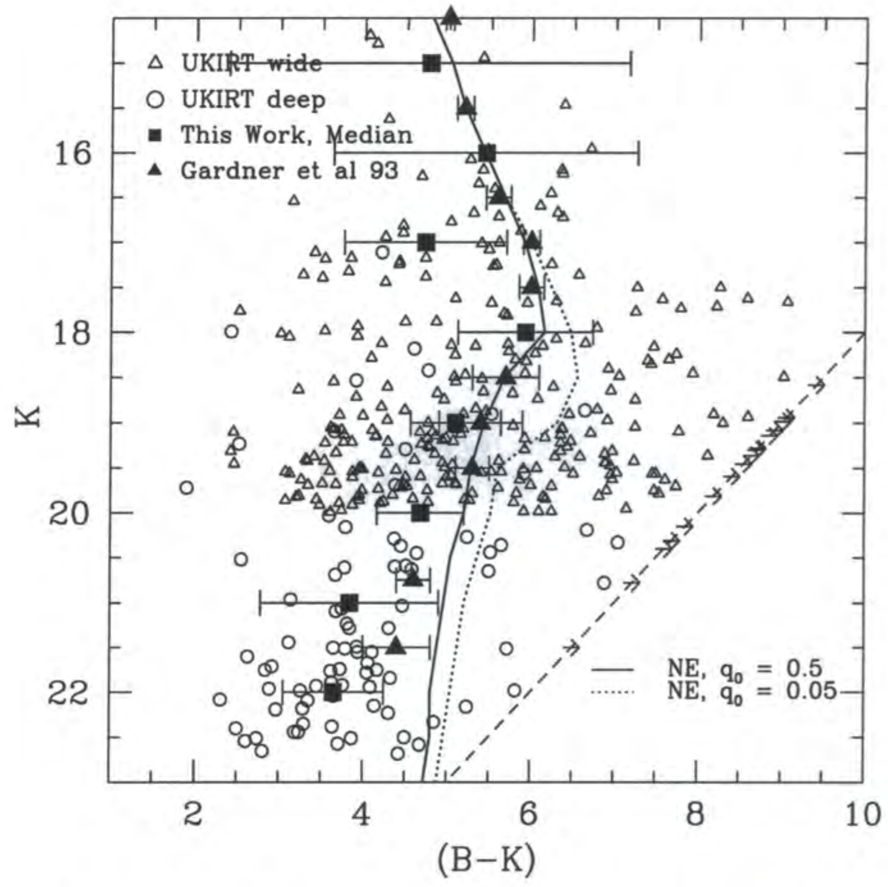

Figure 2.4: $K-$ magnitude against $(B-K)$ colour for galaxies in the wide survey (open triangles) and the deep survey (open circles). Also plotted are the median $(B-K)$ colours in one-magnitude bins for our survey (filled squares), with 1σ error bars calculated by a bootstrap resampling technique. Triangles show median colours from the compilation of Gardner et al. 1993. The dotted line represents the region of incompleteness; galaxies below this line have $B < 28^m$. Drop-outs are plotted at the upper limit of their colours as right-pointing arrows. Heavy arrows are "certain" drop-outs whilst light arrows are "probable". For comparison, predictions from two non-evolving models are plotted; one for $q_0 = 0.05$ (dotted line) and one for $q_0 = 0.5$ (solid line).

Incompleteness is represented by the dashed line; objects to the right of this line have $B > 28^m$. Several objects have been identified in both surveys which are undetected in $B-$ but are detected in $K-$ and these are plotted in the figure as right-pointing arrows and are discussed in Section 2.4.3. Considering the median $(B-K)$ colour we see that it increases steadily until around $K \sim 18^m$ where it reaches a maximum value of ~ 6. After this, it sharply becomes bluer and this blueward trend continues to the faintest limits we have measured $(K < 22.5^m)$. Our median colours agree well with those in Gardner, Cowie, & Wainscoat (1993), even for brighter bins where the number of galaxies in our sample is much smaller. Finally, it is worth noting the extremely large spread in colour in this Figure – at $K \sim 20$ $(B-K)$ ranges from 2 to 9.

Additionally, the predictions of the two non-evolving models shown in Figure 2.3 are plotted. In general, the $q_0 = 0.5$ model gives a slightly better fit to the observed colours, at least until $K \sim 20^m$; at fainter magnitudes, galaxies are significantly bluer than both model predictions.

Another interesting feature in Figure 2.4 is the apparent deficit of galaxies with magnitudes in the range $20^m < K < 22.75^m$ and colours from $4 < (B-K) < 6$. The different areal coverages and depths of the two surveys doubtless exacerbates this effect but its presence is consistent with a population of galaxies which turns rapidly blueward faintwards of $K \sim 20$. We discuss the origin of this feature in Section 2.3.2.

In Figure 2.5 we plot $(B-R)$ *vs.* $(R-K)$ colour for all the galaxies in the wide survey (open circles) and the deep survey (filled circles). Fainter galaxies are plotted with smaller symbols. As expected, the fainter, $K < 22.75^m$ sample is much bluer than the brighter, $K < 20^m$, sample, which reaches $(R-K) \sim 6$. We also plot colour-colour tracks representing the different galaxy classes in our evolutionary models. We defer discussion of these tracks until the following

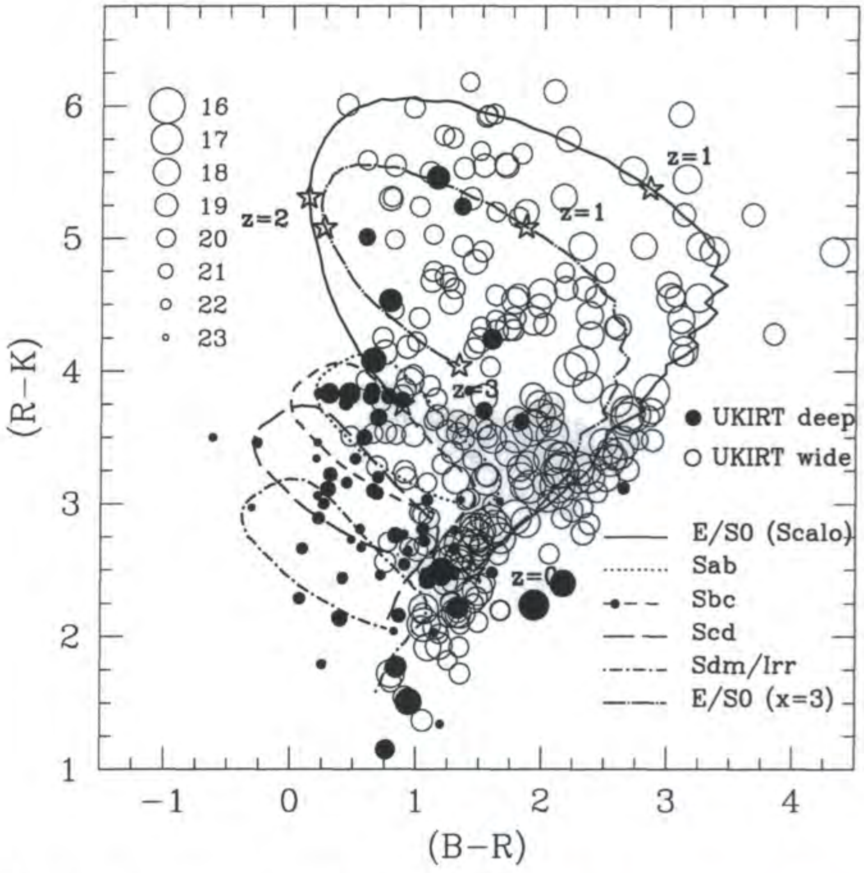

Figure 2.5: $(B-R)$ colour against $(R-K)$ colour for galaxies in the wide survey (open circles) and the deep survey (filled circles). Fainter galaxies are plotted with smaller symbols. Also shown are evolutionary tracks for the five classes of galaxy in our model, as computed from the population synthesis code of Bruzual and Charlot (93,95). The solid line represents type E/S0, the dotted line Sab and the dashed, long dashed and dash-dotted lines types Sbc, Scd and Sdm respectively. The dot-dashed line shows the path in the colour-colour plane of an elliptical galaxy which has an IMF slope, x, of 3. For the elliptical tracks, the labelled stars indicate the redshift. The star-formation e-folding time τ, is 2.5 Gyr for the $x = 3$ model, 1.0 Gyr for the Scalo model, and 9.0 Gyr for all the spiral types.

section.

2.4 Interpretation and modelling

2.4.1 Outline of the models

To interpret our results we investigate variants of a pure luminosity evolution (PLE) model in which star-formation increases exponentially with look-back time (Metcalfe et al. 1991; Metcalfe et al. 1995; Metcalfe et al. 1996). In this chapter, we consider only cosmologies in which $\Lambda = 0$ and take $H_0 = 50$ kms^{-1}Mpc^{-1}, although changing the value of H_0 does not affect any of the conclusions of this paper. Two values of the deceleration parameter, q_0, $q_0 = 0.05$ and $q_0 = 0.5$, are adopted, corresponding to open and flat cosmologies respectively. The input parameters to our models (given in Table 2.4) consist of observed *local* galaxy parameters (namely, rest-frame colours and luminosity functions) for each of the five morphological types (E/S0, Sab, Sbc, Scd and Sdm) we consider in our models. These morphological types are divided into elliptical (E/S0) and spiral (the remainder) and these two classes are each given a separate star-formation history. We normalize to the observed rest-frame $(B - K)$ colours. As we have already explained in Section 2.3.1 we normalize at $B \sim 18$ and seek to explain the low number counts at bright magnitudes from a combination of photometric errors and anomalous galaxy clustering, rather than substantial evolution at low redshift. Our models also include the effects of the Lyman-α forest, and, for spiral types, dust extinction corresponding to the Large Magellanic Cloud as described in Pei (1992). In these models, the addition of dust reduces the amount of evolution produced in the $B-$ band and allows the models to fit the observed number counts at faint magnitudes.

PLE models have difficulty in correctly reproducing the $K-$ band redshift distribution. Even essentially passive evolution over-predicts the numbers of galaxies at $1 < z < 2$, and this fact has been used by several authors (most recently Kauffmann & Charlot (1998)) to argue for the hierarchical, merger-driven galaxy formation models in order to reduce the mean redshift of $K-$ selected galaxy redshift distributions. However, Metcalfe et al. (1996) showed how PLE models *could* produce a $K-$ band redshift distribution compatible with the observations of Cowie, Songaila, & Hu (1996) by assuming a very steep slope ($x = 3$) for the stellar initial mass Function (IMF). This steep, low-mass-star dominated IMF reduces the amount of passive evolution observed in $K-$ and allows us to reproduce the observed redshift distribution, which is close to the predictions of the non-evolving model. Conversely, the $B-$ band redshift distribution from the same survey has a large fraction of high redshift ($z > 1$), high luminosity ($L > L^*$) galaxies. Our steep luminosity function slope for spiral types combined with a small amount of internal dust extinction (corresponding to $A_B = 0.3^m$ at $z = 0$) allows our models to produce this result.

In Figure 2.6 the effect that changing the IMF slope for early types has on the predicted redshift distributions is illustrated. The dotted line shows a model computed using $\tau = 1.0$ Gyr and a Scalo IMF, whereas the solid line shows the $x = 3$ model which has $\tau = 2.5$ Gyr. Also plotted are the redshift distributions taken from Table 2 of Cowie, Songaila, & Hu (1996). Objects which were marked as unidentified in each band in this table are shown in their respective incompleteness boxes. We have normalized both model predictions to the total number of *observed* objects (i.e., unidentified objects are included). We take $q_0 = 0.05$ and $z_f = 6.4$. The $x = 3$ model, as it dominated by dwarf stars produces *much smaller* amounts of passive evolution in the $K-$ band and as a consequence the median redshift of galaxies in this model is much lower than in the "Scalo" model, which produces an extended tail in the redshift distribution.

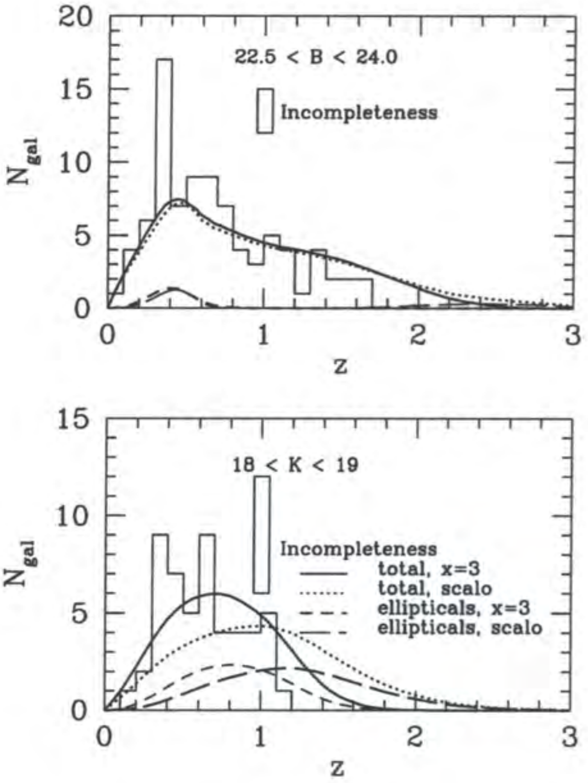

Figure 2.6: Predicted redshift distributions for both "Scalo" ($\tau = 1.0$ Gyr) and "x=3" ($\tau = 2.5$ Gyr) models (solid and dotted lines) compared with the results of the $K-$ (lower panel) and $B-$ (upper panel) redshift distributions taken from Table 2 of Cowie et al. (1996). Incompleteness is represented by the open boxes. Also plotted are the predicted redshift distributions for elliptical types (short dashed and long dashed lines) for the "Scalo" and "x=3" models respectively.

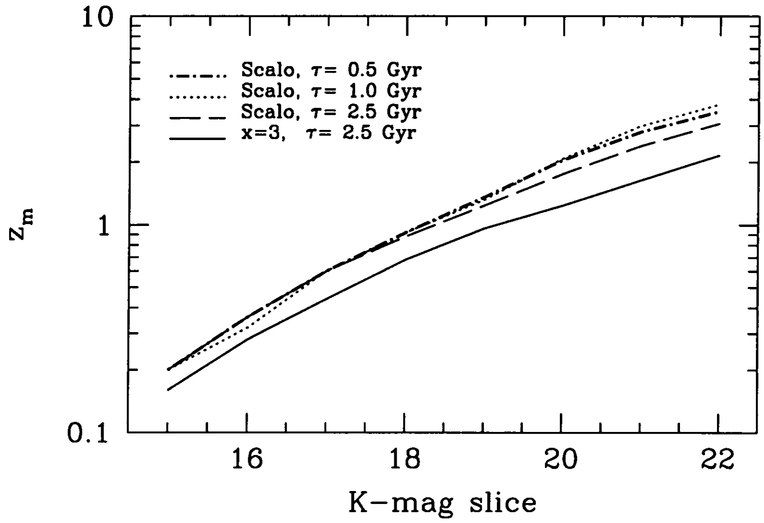

Figure 2.7: The median redshift, z_{med} of elliptical galaxies in our model populations for the magnitude slices used in Figure 2.11 and Figure 2.12.

This point is further illustrated in Figure 2.7 where we show the median redshift of elliptical galaxies with the same star-formation histories as galaxies in Figure 2.8 for several $K-$ selected magnitude slices. This panel shows that, in all magnitude ranges, elliptical galaxies in the "Scalo" model have a higher median redshift than in the "x=3" model. This point is discussed further in Section 2.4.2.

In Figure 2.8 we illustrate the effect which varying the IMF slope and τ has on the colour-redshift relation. The dot-dashed, dotted and long-dashed lines shows Scalo (Scalo 1986) IMF tracks with $\tau = 0.5$ Gyr, $\tau = 1.0$ Gyr and

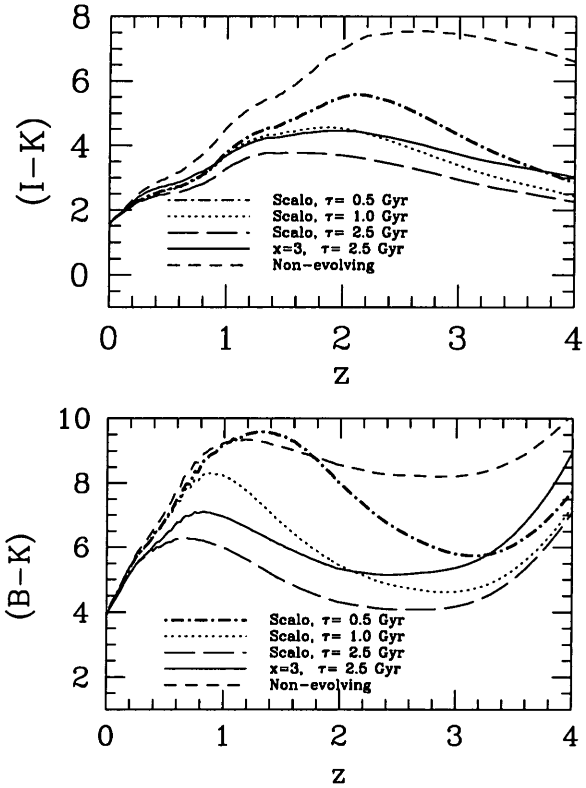

Figure 2.8: **a:** (lower panel) $(B - K)$ colour against redshift, z, for an elliptical galaxy with an $x = 3$ IMF and $\tau = 2.5$ Gyr (solid line), and for the Scalo IMF and for three values of τ; $\tau = 0.5$ Gyr (dot-dashed line), $\tau = 1.0$ Gyr (dotted line) and $\tau = 2.5$ Gyr (long dashed line). Also plotted is a non-evolving model (short dashed line). **b:**(upper panel) As for the lower panel, but with $(I - K)$ colour.

Table 2.4: Luminosity function parameters and rest-frame colours used in all models

Parameter / Type	E/S0	Sab	Sbc	Scd	Sdm
ϕ^* ($\mathrm{Mpc}^{-3} \times 10^{-4}$)	10.2	5.09	6.82	3.0	1.5
α	-0.7	-0.7	-1.1	-1.1	-1.5
M_B^*	-21.0	-21.0	-21.32	-21.44	-21.45
$(B-K)$	3.93	3.78	3.51	2.90	2.26
$(I-K)$	1.57	1.63	1.7	1.47	1.0

$\tau = 2.5$ Gyr respectively, whereas the solid line shows an $x = 3$ model with $\tau = 2.5$ Gyr. As is apparent from the plot, at $z \sim 1$ $(B-K)$ colour depends *very sensitively* on the assumed value of τ and the slope of the IMF. For a given IMF, longer τ's cause the peak in the $(B-K)$-z relation to shift to progressively higher redshifts, a point we will return to in Section 2.4.2. Finally, the $x = 3$ IMF model track, as it is dominated by low-mass stars, is in general redder (for a given value of τ) than the Scalo IMF track.

We now return to Figure 2.5 where we have over-plotted on our $(B-R)-(R-K)$ diagram evolutionary tracks for each of the galaxy types in our model. The solid and dot-dashed lines shows the path of an elliptical galaxy with $\tau = 2.5$ Gyr and $\tau = 1.0$ Gyr and with Scalo and $x = 3$ IMFs respectively, whereas the remaining tracks show the four spiral types in the models, all of which have $\tau = 9.0$ Gyr and Salpeter IMFs. On the elliptical tracks, the labelled stars indicate the redshift at selected intervals.

Generally, there is good agreement between the model tracks and the observed colours. The low redshift $(0 < z < 0.5)$ elliptical track is populated by the brightest galaxies in our sample. Generally, we do not find a large fraction of objects have colours which cannot be reproduced by the tracks (in contrast with the findings of Moustakas et al. (1997) who claimed there was a significant population of objects whose colours could not be reproduced by the models). There are *some* objects which appear to be redder than the tracks, but these do not constitute a significant fraction of the observed galaxy population. We interpret the broad range of $(B-K)$ colours of objects with $(R-K)>4$ as evidence of the diverse range of star-formation histories present in the elliptical population.

2.4.2 Counts and colour distributions

In Figure 2.10 we present a compilation of all published galaxy number counts in $B-$ and $K-$ bandpasses, as well as the predictions from our two evolutionary models. What is immediately apparent is that both the models discussed provide a good fit to the number counts over a wide magnitude range for the low q_0 case. Furthermore, in both $B-$ and $K-$ bandpasses the differences between the Scalo and "x=3" models is *much smaller* than the differences between the high- and low-q_0 models. It is also apparent, as has been noted by many others (Metcalfe et al. 1996; Campos 1997; Babul & Rees 1992) that, unless another population (such as bursting dwarfs) is added to the models, the $q_0 = 0.5$ model under-predicts the observed $B-$ band galaxy counts (and is marginally excluded at the faint end of the $K-$ counts).

Number counts are a coarse test of any model; the extremely deep optical photometry covering the Herschel Field is one of the main virtues of this work. So, to test our models more stringently we now investigate our observed optical-infrared colour distributions.

In Figure 2.11 we compare in detail our model predictions with our observations for $K-$ selected $(B-K)$ colour distributions and compare these with the data (shown as the shaded histograms) in six one-magnitude slices from $K=17^m$ to $K=22^m$. We have also found our $K<18$ $(B-K)$ distributions to be in good

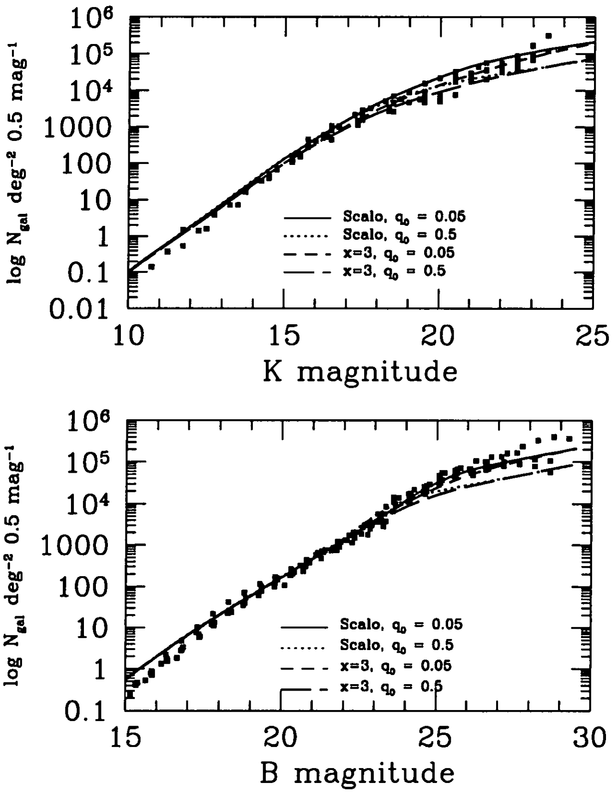

Figure 2.9: Galaxy number counts for two evolutionary models – the "Scalo" model, (dotted and solid lines), and the "x=3" model, (long-dashed and short-dashed), for low and high values of q_0 respectively.

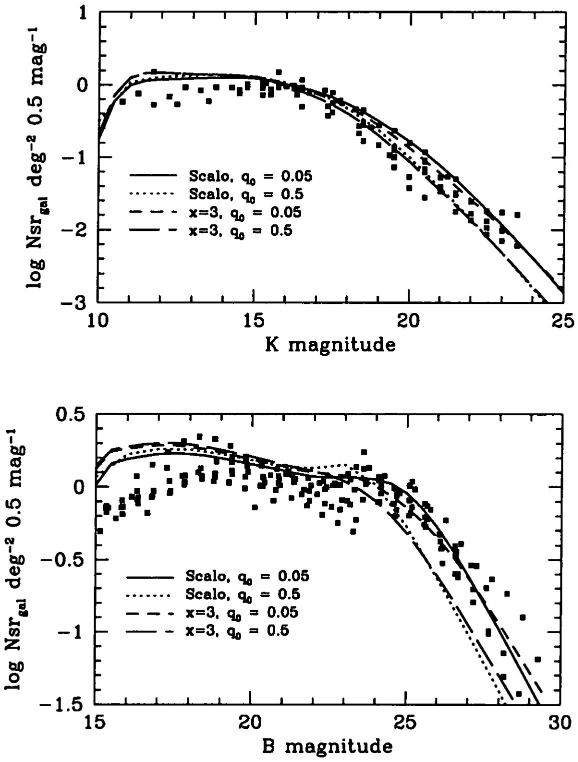

Figure 2.10: This is identical to the previous figure, except in this case an arbitary linear slope has been removed from both plots: $0.5\text{mag}_B - 7.88$ (for B) and $(0.62\text{mag}_K - 7.28)$ for K.

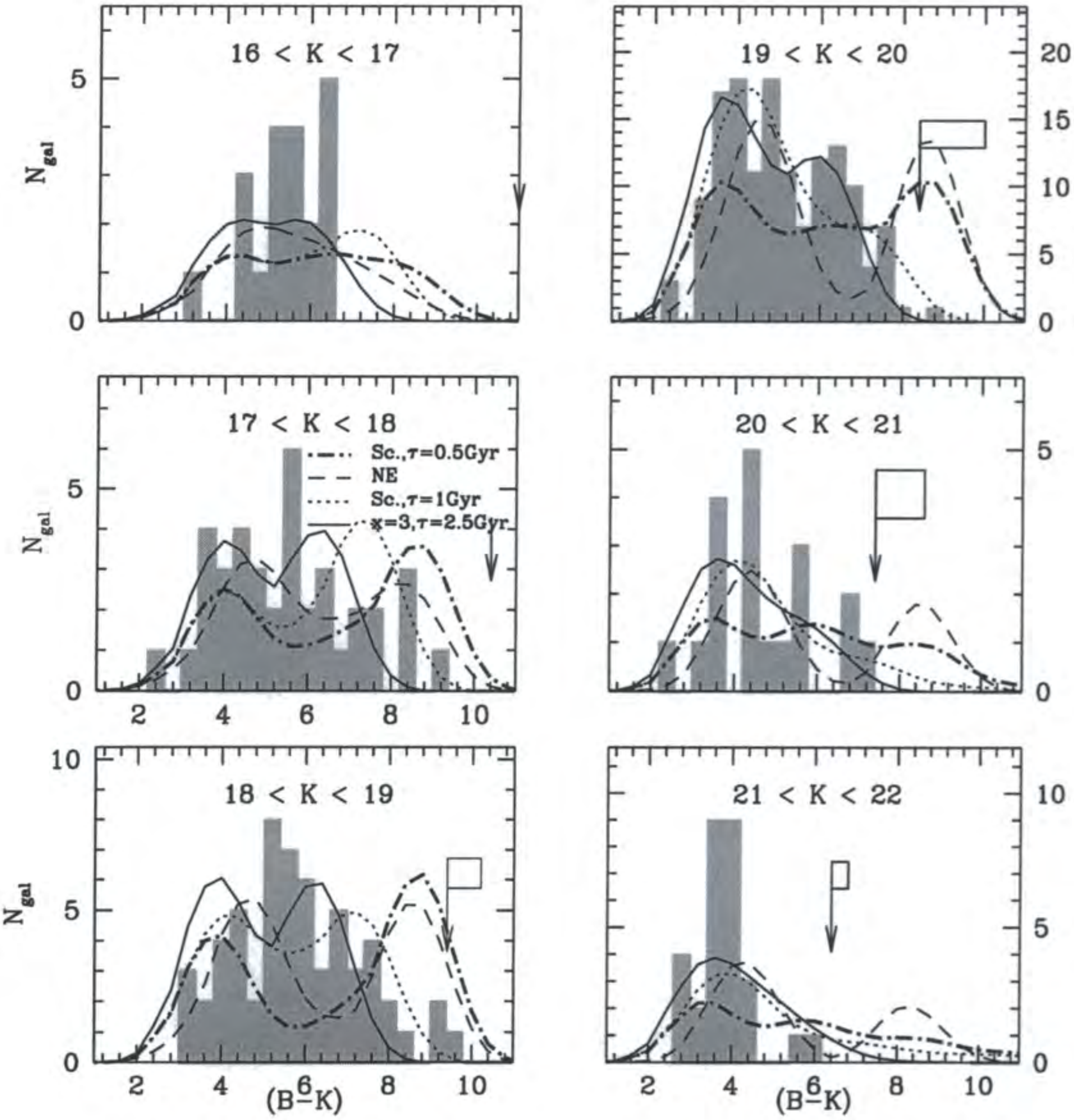

Figure 2.11: $K-$ selected $(B-K)$ colour distributions in six magnitude slices for both the "wide" (brightest four slices) and the "deep" survey (faintest two slices) (solid histogram). Also shown are predictions from four models: "x=3" (solid line), "Scalo" (dotted and dot-dashed lines) and "non-evolving" (long dashed line). The two "Scalo" models have differing star-formation histories; the dotted and heavy-dashed line has $\tau = 1.0$ Gyr whilst the heavy dot-dashed line has $\tau = 0.5$ Gyr. The $x = 3$ models has $\tau = 2.5$ Gyr. The model predictions have been normalized to the *total* number of galaxies in each slice. In the fainter $(K > 18^m)$ bins this includes the $B-$ band non-detections discussed in Section 2.4.3 and the number of such objects in each magnitude slice is represented by the incompleteness boxes. These non-detections were all verified by eye. The position of the downward-pointing arrow represents the colour of the *reddest* object at the centre of each magnitude slice which could be detected; objects in the incompleteness boxes must lie rightwards of this arrow. For all models in this plot we adopt $q_0 = 0.05$.

agreement with the brighter survey of Saracco et al. (1997). In Figure 2.11 the "Scalo" model is shown as a dotted and a dot-dashed line and the "x=3" model is represented by a solid line. All models have been convolved with a conservative 0.3^m colour measurement error (overestimating errors in the brighter magnitude slices). For the non-evolving model, as for the evolving models, $k-$ corrections are calculated from the models of Bruzual & Charlot (1993).

Incompleteness in the histograms was determined by counting how many galaxies had $K-$ magnitudes but were not detected in $B-$ in each magnitude slice (and consequently have undetermined colours). The colour of the *reddest* object which could be detected is represented by the downwards-pointing arrow, which is plotted at the colour corresponding to the $K-$ magnitude at the centre of each magnitude slice (these objects have $B > 28.2^m$). The number of non-detections is shown by the box. Models have been normalized to the total number of galaxies in each slice; in the latter panels this includes $B-$ band non-detections. In these plots we consider only low-q_0 cosmologies, as these models fit the observed numbers counts and (in the case of the $x = 3$ model) redshift distributions.

The non-evolving model predictions (dashed line) rapidly diverge from the data. Faintwards of the $K = 18.0^m$ magnitude slice a bump appears in the model colour distributions, corresponding to the unevolved, red $(B - K) \sim 8$ elliptical population. At approximately the same magnitude limit and at bluer colours (this time at $(B - K) \sim 4$) a second peak becomes apparent. This corresponds to the model spiral population, and at fainter magnitudes this peak becomes the more prominent of the two. This is a consequence of these models where, for $K-$ selected samples, the elliptical counts peak at $K \sim 20^m$; at fainter magnitudes, spiral types form the bulk of the galaxy population.

Qualitatively, the evolutionary models follow the pattern of the non-evolving model, as they also contain two galaxy tracks (for five types in total), though the

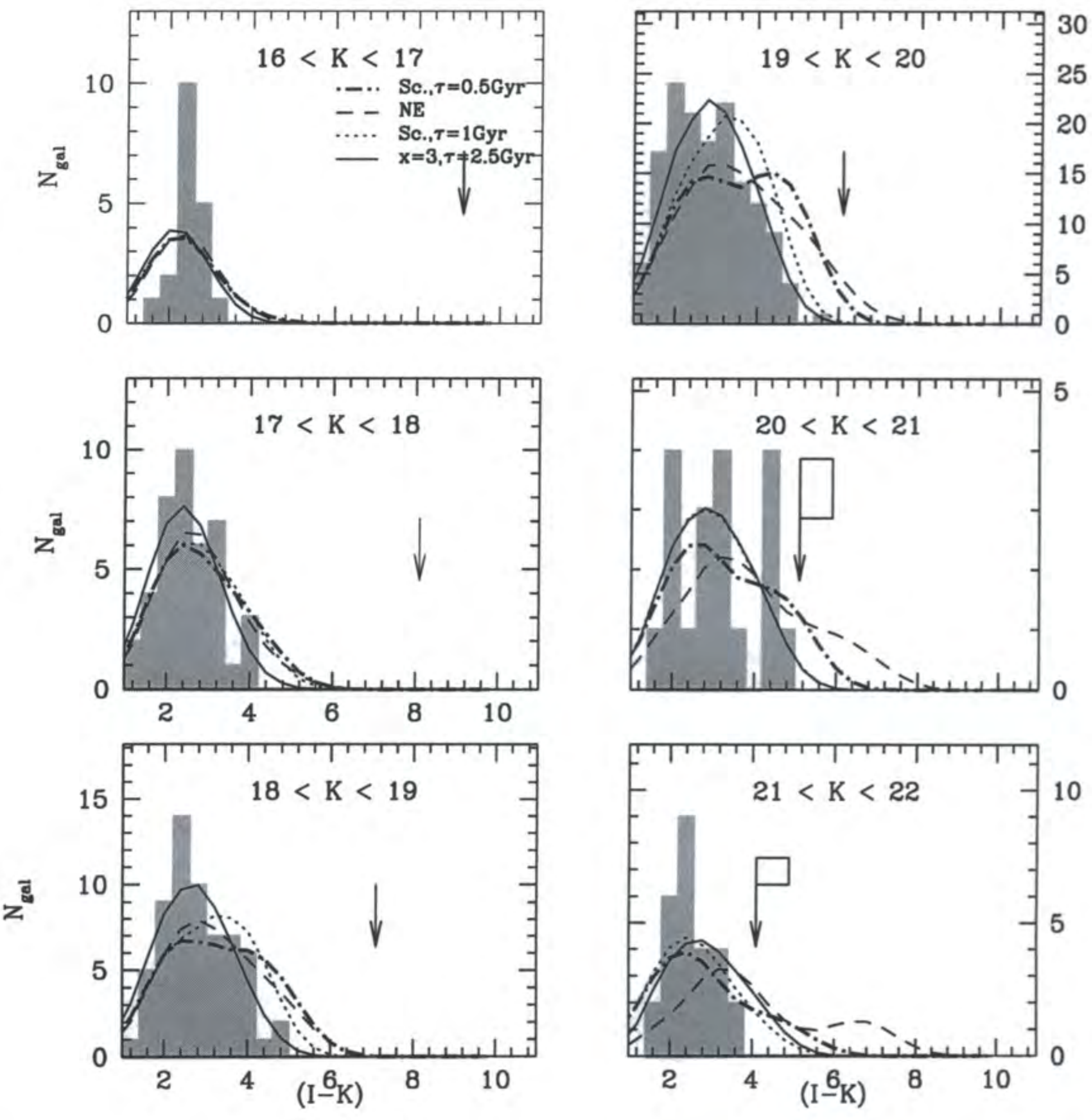

Figure 2.12: $K-$ selected $(I-K)$ colour distributions for a combined catalogue comprising both the "wide" and "deep" surveys (solid histogram). All symbols are as in Figure 2.11.

location and amplitude of the colour distribution peaks depends sensitively on the choice of IMF and τ. Referring to figure 2.8 it is apparent that beyond $z \sim 0.3$, the $(B-K)$ colour for the $\tau = 0.5$ Gyr model is redder than the $\tau = 1.0$ Gyr model; furthermore, as the median redshift of both populations is almost the same (Figure 2.7), changes in the colour distributions are almost completely a product of differences in the $(B-K)$-z relation. In general Bruzual & Charlot (1993)-type models for elliptical galaxies with short τ's for a given IMF slope predict a $(B-K)-z$ relation in which galaxies are at their reddest at $z \sim 1$, and become bluer thereafter until $z \sim 3$ at which point they turn redder once more as a result of Lyman-α forest reddening. The position of this turn-over depends on the assumed τ, the IMF and the redshift of formation z_f.

Now we consider the "x=3", $\tau = 2.5$ Gyr model and we see that its colour distributions are in general *bluer* than those predicted from the "Scalo" $\tau = 0.5$ or $\tau = 1.0$ Gyr models. This is a consequence of the longer τ adopted in this model, but also of the fact that (as we have seen in Figure 2.7) galaxies lie at a lower redshift than the "Scalo" model and consequently are sampling a bluer region of the $(B-K)$-z relation. So, despite the $x = 3$ model being low-mass star dominated, the larger value of τ allows us to produce colours which are blue enough to match the observations.

Returning to Figure 2.11 we can now understand the origin of the differences between the $(B-K)$ colour distributions predicted by the models. Considering first the brighter magnitude slices in Figure 2.11, at $K = 17.0^m$ we see that the "Scalo" $\tau = 1.0$ Gyr model predicts a peak at $(B-K) \sim 7$ which does not appear in the "x=3" model. At this magnitude, elliptical galaxies in the "Scalo" model have $z_{med} \sim 0.6$, whereas for the "x=3" model $z_{med} \sim 0.4$ (from Figure 2.7); as a consequence "Scalo" model colours are redder than "x=3" ones. Furthermore, the essentially passively-evolving Scalo $\tau = 0.5$ Gyr model contains insufficient star-formation to shift the peak at $(B-K) \sim 9$ blueward; as we have seen from our considerations of the non-evolving model, this peak is from unevolved ellipticals. At fainter $(K > 20^m)$ magnitudes, both the $x = 3$ model and the Scalo $\tau = 1.0$ Gyr model turn sharply blueward; the Scalo $\tau = 0.5$ Gyr model colour distribution, however, has a extended tail which reaches $(B-K) \sim 9-10$.

Through a process of trial and error we have determined the combination of IMF and τ for the elliptical tracks which best reproduces the $(B-K)$ $K-$ selected colour histograms *and* allows us to fit the observed $B-$ and $K-$ band number counts. This is a Scalo IMF with a $\tau = 1.0$ Gyr and an $x = 3$ IMF with $\tau = 2.5$ Gyr. In both models, spiral types have a Salpeter IMF and $\tau = 9$ Gyr. These models reproduce the main features of the data histograms, including the broadening of the colour distribution at the $K < 18^m$ slice, and its subsequent narrowing and blueward trend in the fainter slices. Furthermore, as we will see in the following Section, these models are consistent with the redwards limits of our data. Of these two models, the $x = 3$, $\tau = 2.5$ Gyr model, as commented in Section 2.4.1, gives a much better fit to the observed $K-$ band redshift distributions. As is apparent from Figures 2.7 and 2.8 distinguishing between the effects of changes in IMF slope or the star-formation history on the colour-redshift relation is difficult. Making this choice requires additional information such as the redshift distribution of $K-$ selected galaxies.

Finally, this picture also allows us to understand the origin of the deficit of galaxies in the colour-magnitude relation at $(B-K) > 5$ and $K > 20^m$ which we first commented upon in Section 2.3.2. This feature is consequence of the turn-over in elliptical counts and rapid blueing of elliptical galaxies faintwards of $K \sim 20$, which happens in all models regardless of our choice of IMF or τ.

2.4.3 $(I-K)$ distributions and extremely red galaxies

In the previous section we discussed the broad characteristics of the $K-$ selected $(B-K)$ colour distribution and showed how these features can be understood in terms of our models; in this section we turn our attention to very red objects which are at the outskirts of the colour distributions. The red colours of these objects imply they are E/S0 galaxies at moderate $(z > 1)$ redshift and consequently it is interesting to see if their observed number density is consistent with current galaxy formation scenarios. As previous workers (Barger et al. 1998; Moustakas et al. 1997; Zepf 1997; Cowie et al. 1994) who focussed their attentions upon these galaxies discussed them in terms of $K-$ selected $(I-K)$ distributions here we introduce our observations in these bandpasses. Following these workers we define an "extremely red galaxy" as an object with $(I-K) > 4$; from Figure 2.8 we see that at $z \sim 1$, $(I-K) \sim 4$. In this section we will make comparisons with models generated using the same set of parameters as the $K-$ selected $(B-K)$ distributions discussed previously. In interpreting $(I-K)$ colours one faces some significant differences to $(B-K)$ observations; as is apparent from Figure 2.8, $(I-K)$ colour is relatively insensitive to the amount of star-formation; at $z \sim 1$ the difference in $(I-K)$ between elliptical galaxies with $x = 1.35$ (Scalo) $\tau = 0.5, 1, 2.5$ Gyr is 0.5; by comparison, at this redshift $(B-K)$ ranges from ~ 3 to ~ 5. This difference is reflected in the $K-$ selected $(I-K)$ distributions which are plotted in Figure 2.12. This insensitivity makes $(I-K)$ distributions relatively poor probes of the elliptical star-formation history. However, it is precisely this behaviour which makes $(I-K)$ colours useful in detecting high-redshift, evolved ellipticals; Figure 2.8 shows that until $z \sim 2$ $(I-K)$ colour is approximately proportional to z, and is insensitive to variations in τ or the IMF.

Turning to work from the literature, Cowie et al. (1994), in a 5.9 arcmin^2 survey detected 13 objects with $(I-K) > 4$ to $K < 20.9^m$, and concluded that these galaxies do not dominate the faint $K > 20^m$ population. They also concluded that less that 10% of present day ellipticals could have formed in single-burst events. Moustakas et al. (1997) found 8 galaxies with $(I - K) > 4$ and $K < 22^m$ over a small, 2 arcmin^2 area. They also isolated a population of objects with blue optical ($(V-I) < 2.5$) and red near-infrared colours and argued that these colours could not be reproduced with Bruzual & Charlot (1993)-type models. Although we do not have $V-$ band photometry the top middle and top left of Figure 2.5 roughly corresponds to the regions highlighted in the colour-colour plot shown in Figure 9 of Moustakas et al.. These "red outlier" objects, as Moustakas et al. describe them, viewed in the context of the models discussed here are most likely elliptical galaxies at $1 < z < 2$. Finally, both Zepf (1997) and Barger et al. (1998) investigated extremely red objects in the Hubble Deep Field (HDF). Zepf (1997), using publicly-available Kitt Peak near-infrared imaging data covering the 5 arcmin^2 of the HDF, found that to a 50% completeness limit of $K < 22^m$ there were ~ 2 objects with $(V_{606} - K) > 7$. Barger et al. (1998), in a much larger ~ 60 arcmin^2 infrared survey comprising both the HDF and the HDF flanking fields, found 12 galaxies with $(I - K) > 4$ and $19 < K < 20$.

Table 2.5 presents a compilation of observations from these papers as well as our current work. We also show the predictions of the $x = 3$ and Scalo $\tau = 0.5$ model (our model which most closely approximates a single burst), normalized to the total numbers of objects each magnitude slice. Generally, in the brighter bin ($19 < K < 20$) the only substantial comparison that we can make is with Barger et al.. We see a factor ~ 3 more objects than they do, although this represents only a 2σ discrepancy. In the fainter bin $20 < K < 22$ our numbers of red objects agree well with Moustakas et al.. Although our numbers are higher than Cowie et al. (1994) in this range there is still no significant discrepancy due principally to our small area.

Table 2.5: Numbers of objects with $(I-K)>4$ per arcmin^2 with $\pm 1\sigma$ errors. The survey area in arcmin^2 is shown in parentheses. In the "deep" survey ($20<K<22$) there are 7 objects which are undetected in I and therefore only lower limits can be placed on their colours. They are included in their respective bins. The number quoted from Moustakas et al. (1997) covers the magnitude range $20<K<22$.

Author	$19<K<20$	$20<K<21$	$21<K<22$
Model ($x=3$)	0.3	1.4	1.8
Model (Scalo, $\tau=1.0$ Gyr)	0.6	1.4	1.2
Model (Scalo, $\tau=0.5$ Gyr)	1.1	3.1	2.8
This work	$0.5^{+0.1}_{-0.1}$ (47)	$3.9^{+2.1}_{-1.4}$ (1.8)	$1.1^{+1.5}_{-0.7}$ (1.8)
Barger et al. (1998)	$0.2^{+0.1}_{-0.1}$ (62)	$1.2^{+0.5}_{-0.4}$ (7.8)	–
Cowie et al. (1994)	$0.3^{+0.4}_{-0.3}$ (7.1)	$1.5^{+0.7}_{-0.5}$ (5.9)	$0.3^{+0.5}_{-0.2}$ (5.9)
Moustakas et al. (1997)	–	$4.0^{+2.0}_{-1.4}$ (2)	

Barger et al. compared their observations to the predictions of a passively-evolving $\tau=0.1$ Gyr model elliptical population, and concluded that the numbers of $(I-K)>4$ objects observed disagreed with the predictions of this model. Our $\tau=0.5$ Gyr distribution (solid dot-dashed line) in Figure 2.12 is quite similar to this model, and in the $19<K<20$ magnitude slice we can see from Table 2.5 that it does indeed produce a large number of objects with $(I-K)>4$ which are not seen in our observations. We therefore conclude, as Barger et al. did, that the low numbers of objects with $(I-K)>4$ observed at $19<K<20$ disfavour non-evolving and single-burst passively evolving models (the constraints on the models which can be obtained from the distributions at fainter magnitudes are less significant). However, we note that the $x=3$, $\tau=2.5$ Gyr and $\tau=1.0$ Gyr Scalo models do correctly reproduce the observed colour distributions. This is because both these models contain enough on-going star-formation to move galaxy colours sufficiently blueward to match the observations.

Finally, could a merging model, like those adopted by Kauffmann & Charlot

(1998), produce these results? It is not possible to rule this model out and it may even be said that the difficulty that models with standard Salpeter/Scalo IMF's have in fitting the $K < 19$ redshift distribution is evidence in favour of the merging scenario. We therefore consider whether the $K-$ selected $(B-K)$ and $(I-K)$ colour distributions presented here can discriminate between a PLE $(x=3)$ model and a merging model. The $K-$ selected $(B-K)$ distributions in Figure 2.11 are equally well fitted by either model; the red galaxies that are missing at $17 < K < 22$ may either be due to them becoming blue at high redshift due to continuing star-formation or passive evolution – or because they are fainter than expected due to de-merging. However, as we have already noted the $(I-K)$-z relation for E/S0 galaxies is insensitive to changes in τ or the IMF. Furthermore, in the range $18 < K < 20$ some galaxies with the $I-K > 4$ colour expected of $z=1$ elliptical galaxies are detected (Figure 2.12). Indeed the numbers of these galaxies $\sim \times 2$ of what is predicted on the basis of the passive Salpeter/Scalo, $\tau = 0.5$ model and in even better agreement with the other Salpeter/Scalo $\tau = 1$ and $x = 3$, $\tau = 2.5$ models. If the merging model is the explanation of the large deficiency of red galaxies in $(B-K)$ compared to passively evolving models, then it might be expected that a similar deficiency should be seen in $(I-K)$. Since the deficiency in $(I-K)$ is less, then this might be taken to be an argument *against* merging and *for* the $x=3$ PLE model.

2.5 Conclusions and summary

In this Chapter we have presented the results of two near-infrared surveys to $K \sim 20$ and $K \sim 23$ which cover our ultra-deep $(B \sim 28)$ optical fields. We draw the following conclusions from this work:

- Our K number counts are consistent with the predictions of non-evolving models with $0 \leq q_0 \leq 0.5$.

- As previously noted by (Cowie, Songaila, & Hu 1996; Metcalfe et al. 1996; Kauffmann & Charlot 1998) the $18 < K < 19$ $n(z)$ of Cowie, Songaila, & Hu (1996) is also well fitted by non-evolving models. However, passively evolving models with a Salpeter/Scalo IMF predict too many galaxies with $z > 1$. Dynamical merging is one possible solution to reduce the numbers of these galaxies but (Metcalfe et al. 1996)have also suggested that a dwarf-dominated IMF for early-types could offer an alternative explanation.

- Our $K-$ selected $(B-K)$ colour distributions display a strong bluewards trend for galaxies fainter than $K \sim 20$, confirming results previously observed in the shallower surveys of Gardner, Cowie, & Wainscoat (1993)

- At brighter magnitudes ($K < 20$) our $K-$ selected $(B-K)$ distributions indicate a deficiency of red, early-type galaxies at $z \sim 1$ compared to the predictions of passively evolving models. This implies either a PLE model where star-formation continues at a low level after an initial burst or dynamical merging.

- At fainter magnitudes ($20 < K < 22.5$) the continuing bluewards trend observed in $(B-K)$ can be explained purely in terms of passively evolving PLE models with no need to invoke any additional mechanisms.

- Our $(I-K)$ data at $K \sim 20$ show less evidence for a deficiency of red galaxies than passively evolving models or PLE models with a low-level of continuing star-formation, suggesting that at least part of the larger deficiency observed in $(B-K)$ at $K \sim 20$ may be due to star-formation rather than dynamical merging.

- In the range $19 < K < 20$, where our statistical uncertainties are lowest, we detect 0.5 ± 0.1 red galaxies arcmin^{-2} with $(I-K) > 4$. We see a factor

$\sim$ 3 more objects than Barger et al. do although this represents only a 2σ discrepancy. The PLE models discussed here suggest these galaxies will have redshifts $1 < z < 2$. The low numbers of these galaxies is consistent with the predictions of PLE models with small amounts of ongoing star-formation.

Chapter 3

Deep galaxy counts with MARTINI

3.1 An introduction to adaptive optics

The twinkle of starlight, although appealing, has been a source of much consternation for astronomers. In the absence of the atmosphere (as is the case with the Hubble Space Telescope) the resolution of a telescope is limited only by the size of the primary mirror. This limit is called the "diffraction limit". However, light arriving at ground-based telescopes must first pass through the thick soup of the Earth's atmosphere. As the refractive index of hot and cold air is different, and as this air is constantly in circulation, this means that a point source like a star does not appear as a stationary point source at ground level; instead it moves around very rapidly and also moves in and out of focus– all as a consequence of the turbulent motion of the atmosphere. Over an exposure of a few minutes, these effects cause astronomical sources viewed from the ground to appear more extended than they would be viewed from space.

The "seeing" of a astronomical image, usually measured in seconds of arc, describes how much the light from a point source is spread out. Formally, it is the full-width at half maximum (FWHM) of a Gaussian fitted to the radially-averaged light profile of a point source. Excellent astronomical sites, like Mauna Kea in Hawaii have a median seeing of typically $\sim 0.6''$. By contrast, the diffraction-limited Hubble Space Telescope returns images with $\sim 0.04''$. The importance of attaining the best possible seeing was demonstrated in 1995 with the Hubble Deep Field (Williams et al. 1996) which showed how even a comparatively small 2.5m telescope like Hubble could produce images of the distant universe which reached limiting magnitudes as faint or fainter than anything then achievable with (much larger) ground-based telescopes – as well as providing a wealth of morphological information concerning the faint galaxy population. The essence of this advantage is that the time required to reach a given signal-to-noise value (for a point source) depends on the *square* of the FWHM. Furthermore, the high resolution afforded by Hubble allows one avoid the problems of source crowding which afflict deep ground-based astronomical images (Metcalfe et al. 1998; Metcalfe et al. 1995). Ideally one would like to be able to combine the advantages of space-based observations (i.e., high resolution) with the large collecting areas possible with ground based observatories. Correcting for atmospheric turbulence using adaptive optics is one such approach in realising this goal. The aim of this Chapter is provide a broad overview of the techniques of adaptive optics, and to describe an application of these methods to a project to carry out deep near-infrared galaxy counts. The author is not an expert on adaptive optics and nor is this a Thesis concerned primarily with such instrumental details, and so our coverage of these matters will be necessarily brief.

The basic idea behind adaptive optics lies in measurement of the distortions in the incoming wavefront and correcting these distortions with a mirror which can be moved very rapidly. In the future, it is envisioned that all large telescope facilities either nearing completion or completed (The European Southern Observatory's Very Large Telescope, the Gemini telescopes, the Keck I and

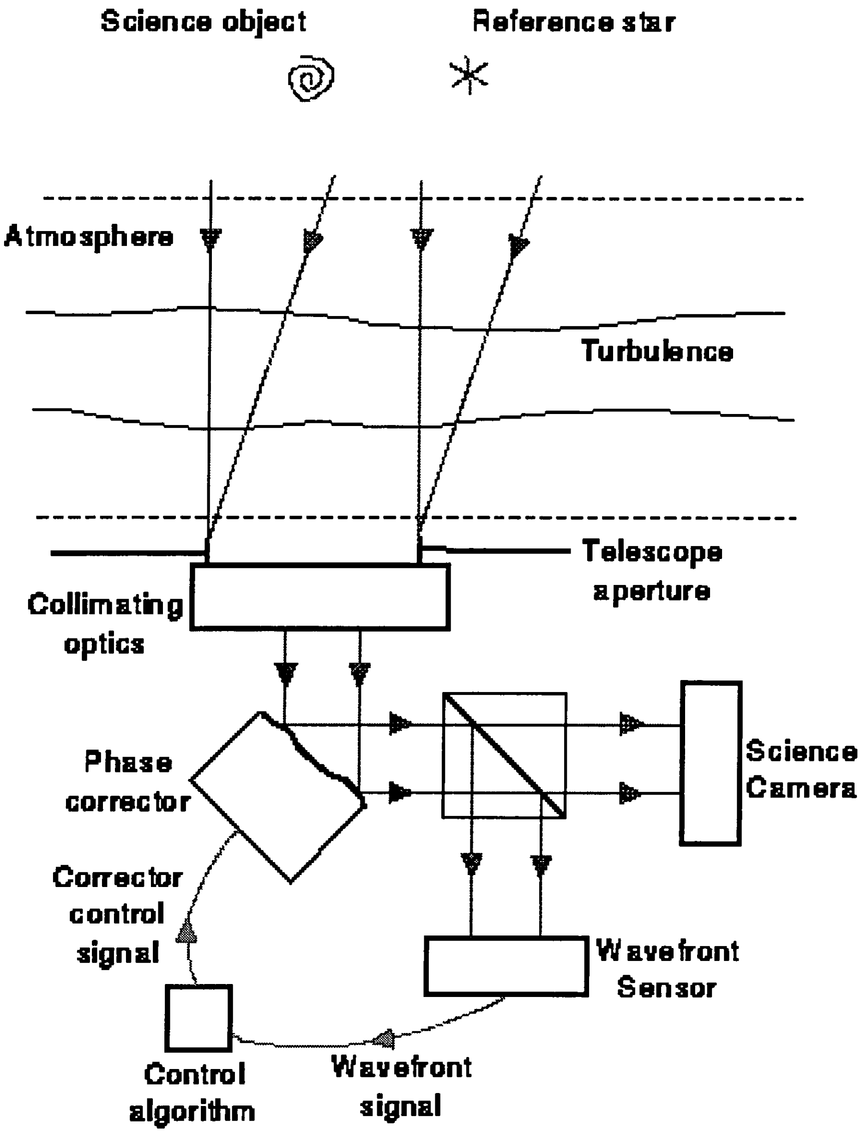

Figure 3.1: A schematic of an adaptive optics system. Light from the reference star and science target pass through atmospheric turbulence and arrive at a telescope. After passing through a phase-correcting device the light is split between the science camera and a wavefront sensor. The output from the wavefront sensor is used to compute the corrections needed to restore the incoming wavefront to its undistorted state. This figure has been taken from the web pages of the applied optics group at Blackett Laboratory, Imperial College, London.

II telescopes amongst others) will have some form of adaptive optics correction available. Additionally, adaptive optics systems have already been retrofitted onto several existing telescopes (for example, the UKIRT upgrades program). At this stage in the discussion it is useful to distinguish between *active* optics and *adaptive* optics. For example, the Gemini North telescope nearing complete on Mauna Kea, Hawaii will have an extensive active optics system. These systems generally correct for mirror deformities or other defects intrinsic to the telescope system. These corrections are applied to the telescope optics once or twice during a typical observing period. By contrast, adaptive optics involves applying corrections to the incoming wavefront at much shorter timescales, typically 10-15 times per second.

This negative-feedback operation – measurement and correction over a short timescale – is a common characteristic of all adaptive optics systems. It can also put stringent limits on the kinds of objects which can be investigated with such a system. In order to apply corrections to the incoming wavefront, a *reference star* must be selected which is sufficiently bright so that wavefront measurements can be made over very short timescales (less than the atmospheric correlation time, denoted by t_0, which is typically the time taken for a turbulence cell to pass over the telescope). If one fails to correct on these timescales then the turbulence pattern will change and the applied corrections will be rendered ineffective. Secondly, this reference star must be close on the sky to the object which is under investigation. The corrections applied to the incoming wavefront from the reference star are in general effective over a very small amount of the sky, related to the size of a turbulent cell in the atmosphere. This scale, known as the seeing size, is denoted by r_0 and is typically $\sim$ 20 cm for a good site, in optical wavebands; the immediate implication of this fact is that, without correction, a telescope with an 8 metre mirror will have the same resolving power as 20cm backyard reflector.

The requirement that the reference star be bright and sufficiently near to the object under investigation has led to a number of alternative approaches being investigated to generate a reference signal. In one solution, artificial reference stars are generated using powerful lasers to excite a layer of sodium atoms $\sim$ 10 km high in the atmosphere. The amount of laser power required to produce such a signal is prohibitively large (typical power requirements are $\sim$ 20 watts of laser power on the atmosphere) and in fact the group with the most experience in this field (the Starfire Optical Range Group) is using leftover technology from the now-defunct Strategic Defence Initiative. Another more serious drawback of laser guide star systems is that, since a round trip is involved in the reference signal, no information is available concerning image motion (tip and tilt), only higher-order effects. For this reason, systems using laser guide stars must also incorporate natural guide stars to correct lower-order effects.

However, deep galaxy imaging is an ideal project to be carried out with adaptive optics. *Any* sufficiently bright reference star may be selected, provided galactic extinction is sufficiently low and there are no other nearby bright stars. Unfortunately, the William Herschel Deep Field, the subject of this Thesis, was carefully selected so there were no bright stars present, and so we were forced to select another field. This was one of the fields described in Roche et al. (1993).

3.2 Specifics: The MARTINI Adaptive Optics System

MARTINI (Multi-Aperture Real Time Image Normalisation Instrument) is an adaptive optics system which was designed to operate at the Naysmith focus of the William Herschel telescope in the Ground-based high-resolution imaging laboratory (GHRIL). The successor to MARTINI, ELECTRA, is in the final stages of testing and will eventually become part of the common-user adaptive

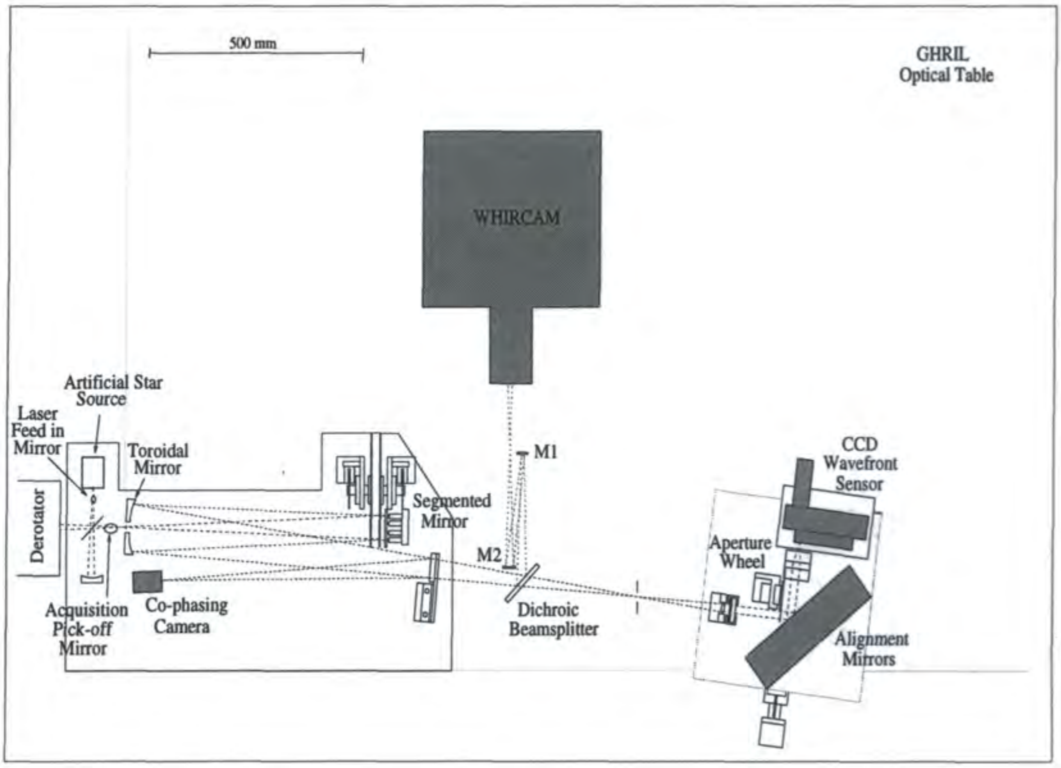

Figure 3.2: The optical layout of the MARTINI system (this diagram has been kindly supplied by A.P. Doel.)

optics system NAOMI on the WHT. All these systems use natural guide stars, with a laser guide-star upgrade option being retained for NAOMI for the future. The MARTINI system outlined here is in fact an upgraded version of an earlier instrument which operated at optical wavelengths and was successfully used to observe Cepheid variables in the Virgo cluster to determine the value of Hubble's Constant (Tanvir et al. 1991; Shanks et al. 1992).

The optical layout of the MARTINI system is presented in Figure 3.2. A dichroic beamsplitter passes infra-red wavelengths light to the science array, which in MARTINI is the WIRCAM detector, a 256 × 256 InSb near-infrared detector, very similar to the IRCAM3 detector described in Chapter 2. Wavefront sensing and correction is carried out with the optical radiation. The advantage of observing at infrared wavelengths is that r_0 is larger; for a seeing of $0.7''$ at

0.5μm it is $\sim$ 80 cm at $\sim 2\mu$m.

At the core of the instrument is a six-element segmented mirror. Before observations commence, each of these segments is carefully aligned so that the light from the reference sources produces six spots in a horizontal line on the corner of the wavefront sensor CCD (only a small fraction of the wavefront sensor detector area is used in order to minimize the readout time; the maximum frame rate the CCD may be read with this arrangement is $\sim$ 400 Hz). By measuring the $x-$ and $y-$ displacements of these spots the tip-tilt and higher-order distortions to the incoming wavefront may be measured; in the case of a pure tip-tilt distortion which is the same over all six sub-apertures then all the spots will be displaced in equal directions. The arrangement outlined above is known as a Shack-Hartmann sensor and has the essential quality that it measures the *slope* of the incoming wavefront. These measured displacements are then used to compute how much each of the mirror segments must be moved in order to return the wavefront to an undistorted state; the mirrors are moved by applying a voltage to a piezo-electric actuator under each segment. If only tip-tilt correction is required, then displacement of the spots can be used directly without further processing; to correct for "piston" of the wavefront (motion along the direction of the wavefront) the six elements of the mirror is operated in "co-phasing" mode. In this mode of operation, the shape of the distorted wavefront is recovered by fitting a numerical expression to the tilts registered by each of the six subapertures.

3.3 Observations and data reductions

Observations took place from 29th August — 2nd September 1996 at the William Herschel Telescope at Observatorio del Roque de los Muchachos, on La Palma in the Canary Islands. This run was at the end of a commissioning period for the MARTINI instrument (25th — 28th of August). The co-ordinates of the observed field was RA +23 hrs 2 min 46 sec and DEC +10° 16 min 48 sec (J2000). This field was selected from optical imaging data taken at the Isaac Newton Telescope by Roche et al. (1993), and has a 12.1 $V-$band magnitude star at its centre. Almost all of the first night was lost due to thick cloud and instrument problems. Total exposure time on the target field was 14.25 hrs. Seeing before correction was $\sim 1''$; throughout the run MARTINI was used only to correct for tip and tilt. The detector scale used was $0.24''$ pixel^{-1}, giving a total field of view of 1.05 arcmin^2.

Conventionally, infrared data reductions involve subtracting a sky frame consisting of a median of temporally adjacent frames; this is the technique adopted in Chapters 2 of this Thesis. This is necessary because the sky background is extremely large (typically $\sim 12-13$ magnitudes in $K-$) and varies on short timescales (on order of several minutes). Additionally, these frames are normally dithered to ensure that, when they are combined, as many pixels as possible are sky pixels and not object pixels.

The design of the MARTINI instrument is such that the guide star used to compute the adaptive optics correction must at all times be at the center of the target field. This means that the normal "dither-and-offset" technique outlined above cannot be used. However, as the WHT is an alt-azimuth telescope, it has a field de-rotator which ensures that the science field maintains the same orientation as the telescope tracks across the sky. Additionally, under the control of the telescope operator, the science field can be rotated to any arbitrary position angle (PA). The strategy adopted for these observations was to expose with MARTINI until the observation was sky-noise limited (typically this was 60 seconds) and then to rotate the field by 45°, realign MARTINI and to observe again. This procedure was repeated throughout the night, with occasional breaks to observe standard stars. As MARTINI and the WHT are not optimized for near-infrared observations and have significant thermal emissions, observations were conducted in the $H-$ band (1.5μm).

Data reductions start with subtracting a dark frame from all frames; next, for each night a flat frame is constructed which consists of all program observations scaled and then median combined. This flat is normalized by dividing it by its median value and each data frame is divided by this flat field. Next, a *running sky* frame is constructed by averaging and scaling six temporally adjacent sky frames, with sigma clipping to remove object flux. Before subtracting this sky frame from the data frame, the data frame is scaled to have the same median value as the sky frame. After subtraction, an arbitrary constant (2000 in this case) is added back to the frame.

The next stage in the procedure involves producing a stacked image; first the images must be slightly shifted, using a marginal centroiding algorithm on the bright reference star in the centre of the frame (the images are always rotated around the central reference star, but the central reference star is not always exactly in the centre of the frame). Following this, the images are all rotated so they have the same orientation, and then averaged together, again using sigma clipping, this time to remove transient hot pixels. A mask frame is next calculated from this image, flagging all pixels more than 3σ above the background. This mask frame is necessary as the presence of objects in the data frames will produce a biased determination of the sky. Additionally, as the number of different orientations of the detector on the sky is small (multiples of 45° degrees) it is essential that this masking procedure is carried out.

Following the generation of the mask, it is unshifted and rotated so that it is aligned with the data frames. The creation of the sky frames and the production of the stacked image outlined above is then repeated with these mask files. Finally, the five stacked frames from each of the five nights were combined using sigma clipping and averaging.

3.4 The deep image

The final image is shown in Figure 3.3. Several objects are apparent in this stacked image which are not evident in the individual exposures. Considering that an individual image has a variance in counts per pixel of $\sigma \sim 2.17$. Possion considerations indicate that 171 images should have a $\sigma \sim 0.17$. The sky noise should be constant over the central portion of the image, where there is the same amount of exposure time; however it is not, varying from $\sigma \sim 0.18$ to $\sigma \sim 0.27$. This would indicate a significant ($\sim$ 20%) non-Poissonian component to the image noise. This noise variation also implies that the limiting magnitude will vary across the frame, making object detection problematic. With this stated noise variation, the calculated 3σ detection limit of $H = 22.1$ mag will vary by $\sim$ 0.3 mag across the frame. A possible explanation for this effect is that the number of distinct orientations over all the images is quite small; there are eight positions from PA 0° to 270°. This means that over all $\sim$ 170 images, there are eight groups of 22 images which have identical orientations.

Another, more serious, deficiency in the final image is the poor seeing– although there is only one unsaturated stellar source near the centre of the image (and within the isoplanatic patch) this has a FWHM of $\sim 0.8''$. The infrared observations detailed in Chapter 4 have a seeing comparable to this, in the absence of *any* correction, whilst $J-$ band observations of the Herschel Deep Field taken at the Canada France Hawaii Telescope (as part of a programme not outlined in this Thesis) actually have *better* seeing. What is the reason for this? During the run, seeing was mediocre – $\sim 1''$. AO systems work best in conditions of moderate to good seeing – little can be done to improve mediocre conditions.

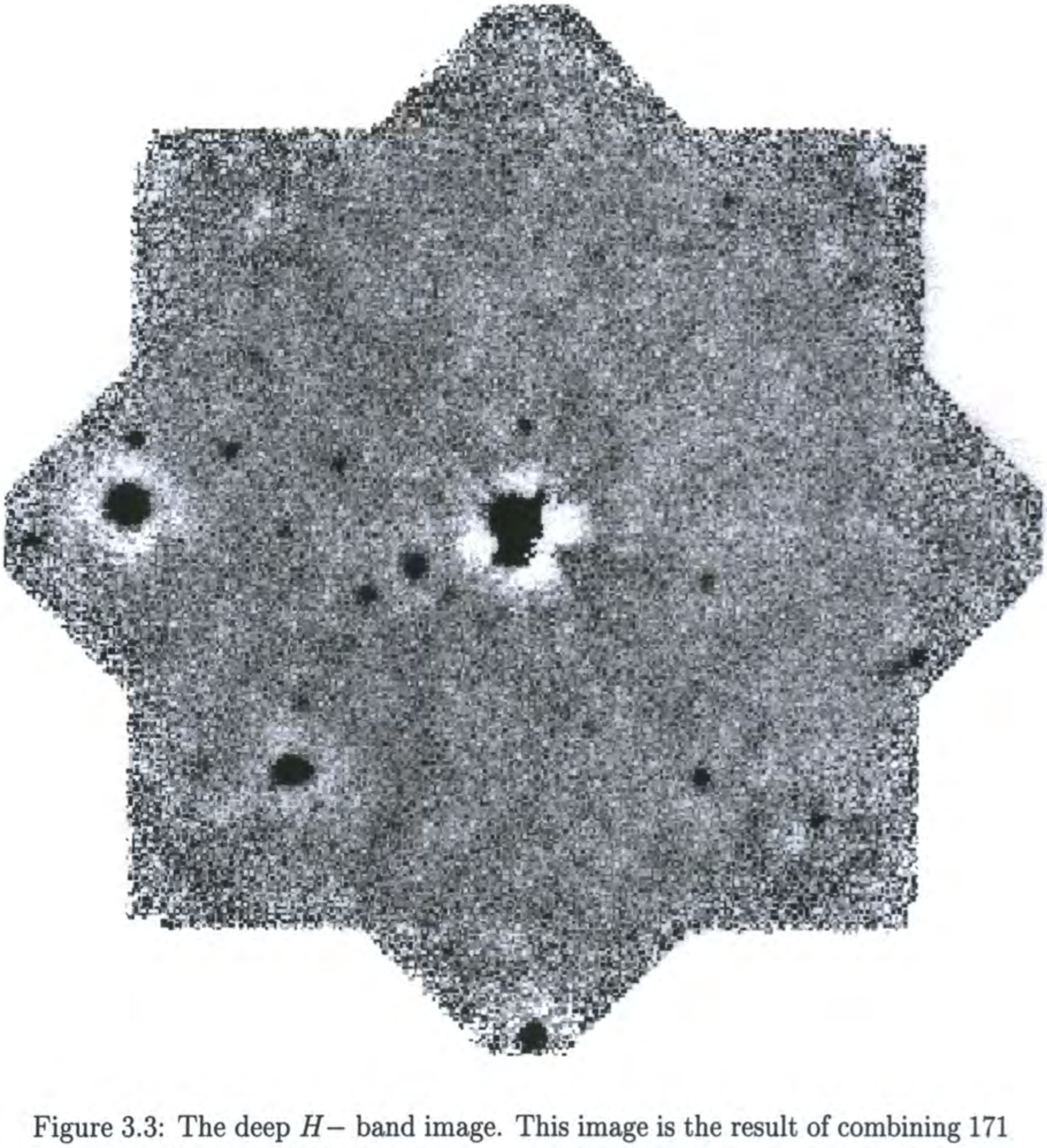

Figure 3.3: The deep $H-$ band image. This image is the result of combining 171 individual frames of 300 seconds exposure taken over four separate nights. This image has a scale of $0.24''$ pixel^{-1} and covers (after trimming to a square format) an area of 1.1 arcmin^2.

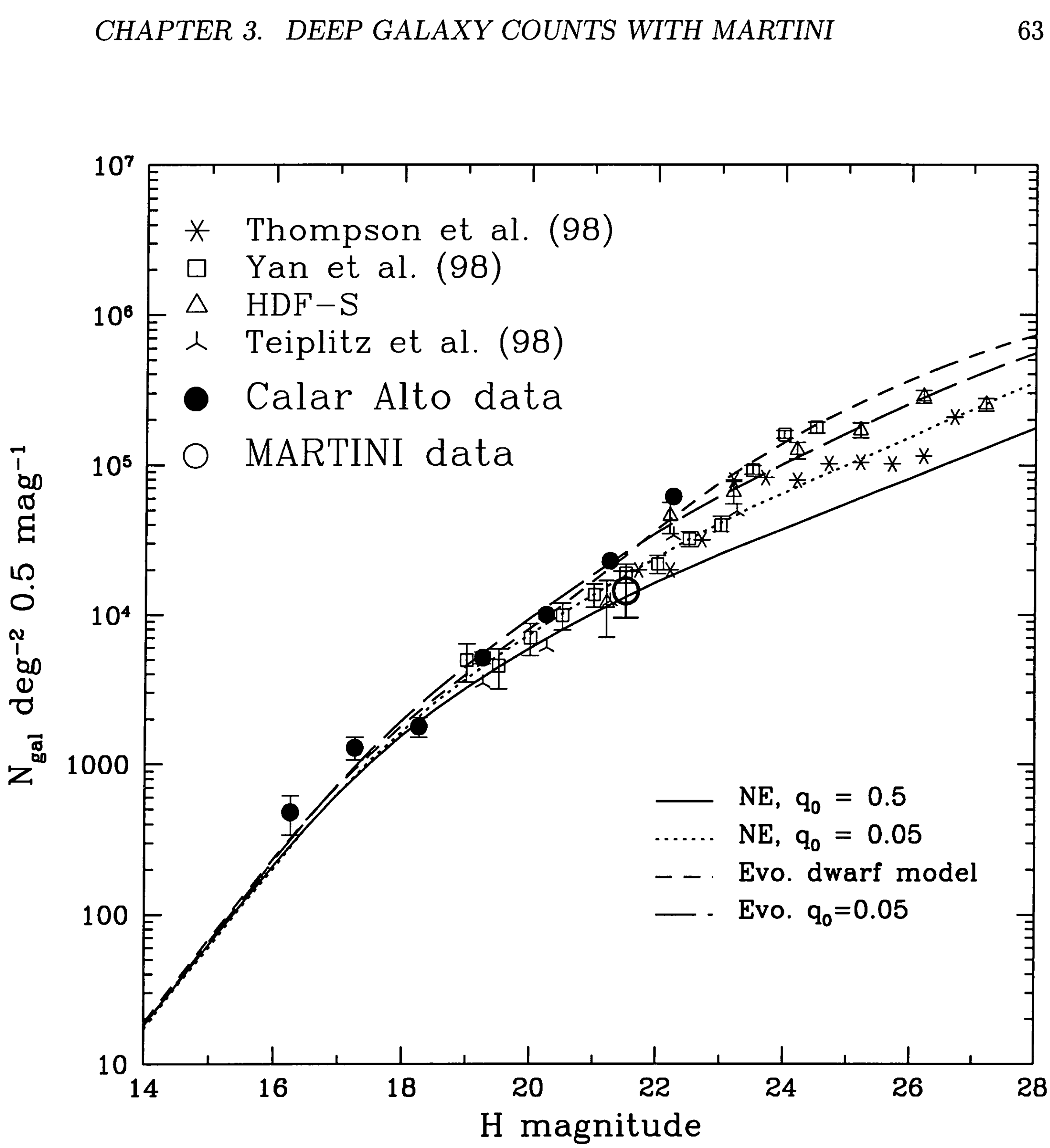

Figure 3.4: $H-$ band numbers counts from the literature (open symbols), from the Calar Alto observations described in the following Chapter (filled circles) and from MARTINI (open circle). The number counts of Thompson et al. have been adjusted using their supplied incompleteness corrections. Also shown are the predictions of four models – a low- and high- q_0 non-evolving model (solid and dotted lines respectively), and two evolutionary models, described in the text (long dashed and short dashed lines).

In Figure 3.4 we reproduce the compilation of deep $H-$ counts presented in Chapter 4 but with the number count from the deep $H-$ frame added (shown by the open circle). Using the SExtractor program (Bertin & Arnouts 1996) we detect 15 objects with $H < 22$. In the magnitude range $21 < H < 22$ there are 8 objects, and this corresponds to the point plotted on the graph.

Our point from our "deep" observation does not reach significantly fainter limiting magnitudes than our Calar Alto data. Was the actual magnitude limit reached in accordance with our expectations? Based on our measurements from standard stars, we derive an efficiency (from the top of the atmosphere and including the WHIRCAM detector) for the MARTINI system of 0.17, which is close to the value quoted in Doel et al. (1999), which was based on previous MARTINI observing runs. Furthermore we measure a sky background at H of 13.4 mag arcsec0^{-2}, comparable to the sky brightness of 12.8 mag arcsec^{-2} at K measured for our UKIRT run. Our final stacked frame consists of 171 exposures each of which is five minutes in duration, giving a total integration time of 14.25 hrs. In comparison, for our Calar Alto run we reached (3σ) limiting magnitudes of $H = 22.5$ after integrating for $\sim$ 13 hrs. The fainter limiting magnitudes for the Calar Alto data are consistent with higher efficiency of the Omega-prime instrument and the better seeing during this run. Based on these considerations, we conclude the limiting magnitude for the final stacked frame is within expectations.

It is also worth recalling the S/N variation across the frame commented on earlier. This difference will cause a corresponding variation in incompleteness; our stated 3σ limit only applies to the *lower* noise regions. This noise variation makes drawing conclusions from observations at or near even the 3σ limit a hazardous affair. A thorough investigation of the noise properties of this image would require adding in many artificial sources (or using the brighter images present in the frame itself) at random locations and measuring the recovery rate from the source detection program as a function of source brightness and position.

3.5 Lessons and conclusions

The main conclusions we draw from our attempt to use adaptively corrected optics to carry out deep number counts are as follows.

- It is clear that if *numbers* of objects is what is required — as is the case if one is performing classical statistical tests such as number counts and colour distributions, a detector which covers the widest possible area is to be preferred over one which delivers marginally better seeing over a much smaller area. Comparing our Calar Alto dataset against the dataset discussed in this Chapter makes this point especially clear.
- In designing any system which delivers adaptively corrected images, thought must given *at the design stage* as to how the data from the instrument will be turned into a scientifically useful format. The greatest difficulty in using the MARTINI instrument to perform our number counts program was that the guide star could not be moved from the centre of the frame; as we have seen in previous chapters, dithering is an essential aspect of any near-infrared observation program. The adopted solution of rotating the field of view about the guide-star for each exposure doubtless led to the observed (significant) noise variations across the frames.

There is no doubt that AO systems can provide an important contribution to the field of observational cosmology; already several papers have been published using adaptively corrected images to investigate the morphology of high-redshift galaxies. For example, Schade et al. (1996b) used the Canada-France-Hawaii telescope's HRCAM to investigate properties of disks at intermediate redshift. However, to effectively compete in statistical cosmology, which demands large sample sizes, the loss in throughput must be compensated by *significant* improvements in delivered FWHM.

Chapter 4

Calar Alto Observations of the WHDF

4.1 Introduction: a wide-field near-IR array

It is certainly the case that since the earliest days of their science, astronomers have attempted to make N as large as possible. N might be either the numbers of objects observed or the quantity of photons collected at the telescope. Such a strategy (either in an enterprise of cartography or in an attempt to make observations more accurate and thereby to test theories more rigorously) has led to many of the most important discoveries of modern cosmology. In observational cosmology, in which statistical astronomy is a major component, it is of paramount importance. For example, in Chapter 2 we presented results from a near-infrared survey of the William Herschel Deep Field using a 256^2 element detector; with the pixel scale used at UKIRT, this meant each exposure covered only 1.5 arcmin^2 of sky. Even at the very faintest limits we reached ($K \sim 23$) there are only ~ 80 objects on the sky in this area and at these depths. With these small numbers of objects, it can be difficult to draw many statistically significant conclusions. The reason for this is simply that in many cases in astronomy errors in measurement (provided N is at least in the few tens) are well described by Poisson errors, which means the fractional error decreases if more objects are observed. There are exceptions and complications of course; the observational cosmologist is often faced with the problem that only one bit of the Universe has been observed, or indeed only one Universe. If one attempts to cover a larger area — as we did in our UKIRT "wide" survey — one must accept probing to a much shallower depth as the telescope can observe a tiny part of the sky at one time. In the case of galaxy surveys like ours the N which we would like to make as large as possible is the volume of the universe we are surveying *and* the numbers of galaxies we observe.

The quest for ever larger and more sensitive detectors can present formidable technological challenges. Along the way, observations have spread out from the visible wavelengths to either end of the electromagnetic spectrum. Infrared arrays are a recent development and are currently several years behind optical CCD arrays in terms of available area and efficiencies. Their construction is a difficult problem in semiconductor process technology; one must bond together two separate and very different arrays — one to detect infrared photons and produce electrons and a second to amplify these electrons to measurable levels. Each pixel in each of these arrays must be connected with a tiny iridium wire. The observations in this Chapter were taken with a 1024^2 Rockwell "Hawaii" infrared array, currently the largest available such array. The Calar Alto 3.5m telescope in southern Spain is one of the few telescopes in the world which offers such an array on a common-user basis. With this detector in just over half an hour we reached a comparable limiting magnitude in K over the same an area of sky which at at UKIRT took us three nights with an array covering $\sim$ 30 times less sky. These observations will be the focus of this Chapter; we will compare them to our previous work and discuss what new conclusions we draw from them.

For pragmatic reasons outlined below the majority of our observations conducted at Calar Alto were in the near-infrared H-band (centred at 1.5μm) rather than the usual K-band filter. In our catalogue of H-selected galaxies there are ~ 3 times more sources than in the UKIRT wide catalogue we discussed previously.

4.2 Observations and Data Reductions

Observations took place at the 3.5m telescope of the Calar Alto Observatory in the Sierra de Los Filabres in Andalucia, southern Spain, from the 14th to the 19th of August 1997. Observations were made with the Omega-prime camera, which consists of a 1024^2 HgCdTe Rockwell "Hawaii" array. The scale on this detector is $0.3961''$ pixel^{-1}, giving a total areal coverage of 45.7 arcmin^2. Observations were photometric on the first and fourth of the five nights. Seeing FWHM was $\sim 0.8''$.

Our primary objective was to image the WHDF as deeply as possible, which meant maximizing our on-sky integration time. During the first night, we observed the WHDF in K' and measured a sky background in this waveband of ~ 11.5 mag arcsec^2. This K' filter, sometimes also known as K-short, cuts off slightly bluewards of the standard $K-$ filter in an attempt to reduce the sky background; it is described fully in Wainscoat & Cowie (1992). The high sky background means that only 30 second integrations were possible before Omega-prime saturated. This high background is a consequence of the design of the Omega-prime camera, which does not have a cold pupil stop and therefore sees significant thermal emission from the telescope. Combined with the substantial readout time of the Omega-prime array (typically 2-3 minutes) this means very high overheads are associated with K' observations as many short exposures must be co-added order to achieve long integrations.

In H the situation is somewhat different. In this waveband, the lower sky background of $\sim$ 13.5 mag arcsec^{-2} means exposures of up to 80 seconds are possible before array saturation sets in. Therefore, observing in H results in lower overheads and greater efficiencies. Additionally, our scientific objectives are not compromised if we observe at H as opposed to K as $(H - K)$ is only weakly dependent on K (Bershady, Lowenthal, & Koo 1998). For this reason, the majority of our observations were carried out at H. Only for the first night did we observe the WHDF in K', for a summed integration time of 45 minutes. Total H- integration time on the WHDF was $\sim$ 13 hrs. Observing at H has the added advantage, as we shall see, in that we may compare our observations directly with those of the NICMOS instrument on the Hubble Space Telescope.

Our K' observations were reduced in a manner very similar that outlined in Section 2.2. However, several aspects of the Omega-prime detector necessitated changes to this procedure. Firstly, the camera is not a contiguous array of pixels; instead it is composed of four separate 512^2 (butted) arrays, each of which is read out independently and each of which has separate controller electronics. The immediate consequence of this arrangement is that each quadrant can have significantly different background levels, which must be removed before any frames are combined. Also there are a number of bad rows and columns at the quadrant edges (and therefore at the centre of the detector) which also must be removed. For this reason, background subtraction was carried out on each of the four quadrants separately. Then the standard procedure outlined in Section 2.2 was carried out: sky frames derived from the median of temporally adjacent frames were subtracted from each image, and this sky-subtracted frame was divided by a 'superflat' frame produced by medianing together all observations from that night's data; the resulting stacked frame was used to produce object masks and the procedure repeated. In this way satisfactory results can be obtained for all the K' observations.

For calibration, we use the UKIRT faint standards (Casali & Hawarden 1992), with additional standards from Hunt et al. (1998). An additional complication is that the low altitude of the Calar Alto site in combination with a significant concentration of airborne particulates means that the extinction measured in K', unlike at UKIRT on Mauna Kea, is non-negligible. This is illustrated in Figure 4.2 where we plot the instrumental magnitude of a star in the WHDF against airmass; a clear correlation is observed. We correct our zero-points to correspond to the mean airmass of 1.2 of our program field. We have carried out a photometric comparison between our $K-$ observations from IRCAM-3 at UKIRT and the K' observations discussed here. This is shown in Figure 4.1. We found that at $K \sim 19$ our r.m.s scatter to be ~ 0.2 mag.

The amount of extinction measured at H is found to be negligible and we disregard it in what follows. Our derived zero-point at H is 26.2 ± 0.05 magnitudes per second. Comparing our Omega-prime observations (after zero-pointing them to K), with our IRCAM3 observations, we find the $(K - K')$ term to be undetectable and for the remainder of the Chapter these bandpasses are regarded interchangeably.

The nature of the near-infrared sky background necessitated a different reduction procedure for the $H-$ band observations. At shorter wavelengths ($\sim 1.5\mu$m), the near-infrared sky background is dominated by many intense, narrow and highly variable OH airglow lines, unlike at longer wavelengths (such as the range covered by our K' filter) where thermal emissions from the telescope and atmosphere are more important; these are expected to change over much longer timescales. Qualitatively, this is what we find in our observations; if the standard data reduction procedure used above is applied to the $H-$ data, large intensity variations are observed across the array, which vary in intensity and position from frame to frame. Furthermore as part of a recent design study

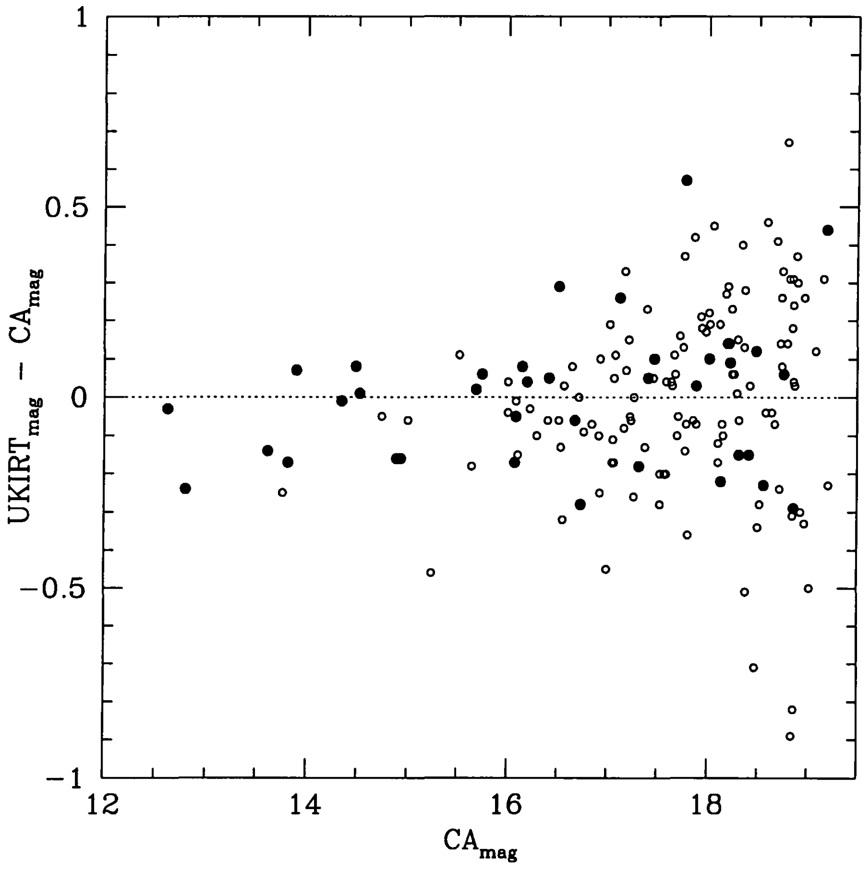

Figure 4.1: Photometric comparison between objects on our UKIRT IRCAM-3 $K-$ wide-area data described previously and on our Calar Alto image. Galaxies and stars are open and closed circles respectively.

for a proposed instrument (Raucher et. al 1998), B. Rauscher has carried out an independent, quantative analysis of the sky variations as measured from this Omega-prime data. He concludes that OH airglow, changing on timescales of ~ 1.5 minutes is responsible for the observed 0.5% variation in the sky background. It is the short timescale of these changes which demands that alternative data reduction techniques are investigated. To this end, a "self–flattening" method was developed in which each individual frame was used to estimate the overall sky background.

Such an approach is fraught with hazards. It is essential that the sky frame

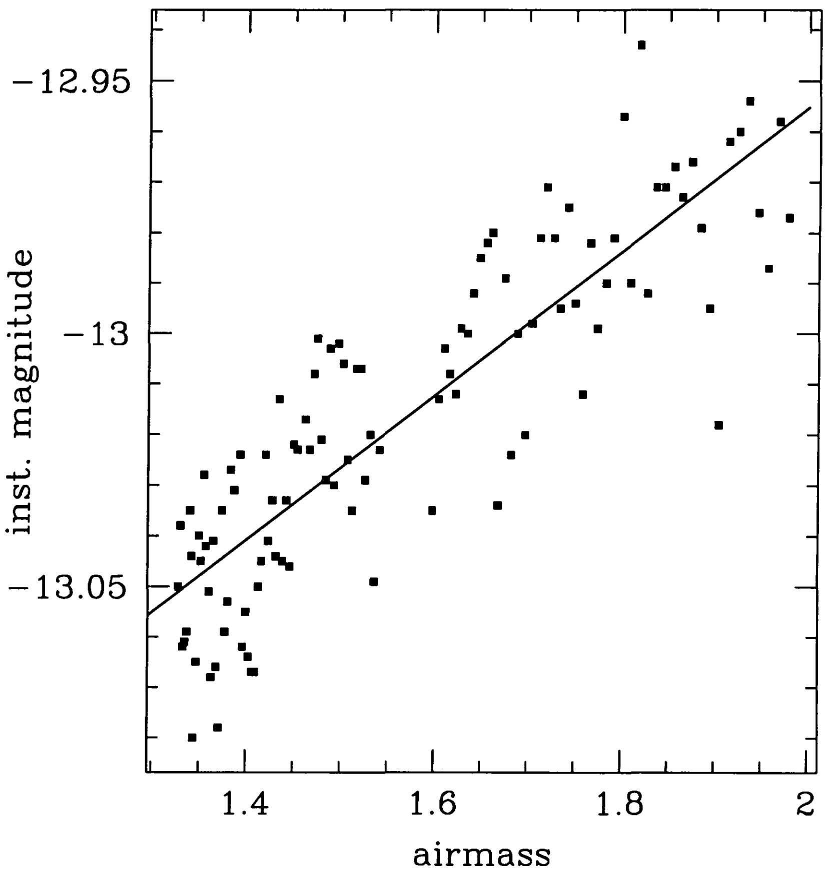

Figure 4.2: K' extinction at Calar Alto as determined from observations of an unsaturated star on our program field taken on the first night. Magnitudes were measured using a standard curve-of-growth analysis. The fitted slope of line shown is 0.14 magnitudes/airmass.

does not contain any object flux; if it does, then subtracting the constructed sky frame from the object frame will reduce object fluxes and change measured magnitudes. The technique which we have developed was found not to introduce any systematic biases into measured object magnitudes; reduction of the K' data-set using this procedure and comparing magnitudes with the IRCAM-3 observations revealed no detectable systematic effects.

The reductions proceed as follows: to start with, a flat field is constructed from that night's observations and divided through all the data frames. Each data frame is separated into its four component quadrants (to eliminate edge effects) and block-averaging and boxcar smoothing is carried out on each quadrant separately. The quadrants are then magnified back to their original size and subtracted off the science frame. These subtracted frames are re-aligned using bright reference stars (as they were dithered on the sky to allow bad pixel rejection) and mean-combined to produce a final stacked frame on which objects are identified and used to make a mask frame which flags all the object pixels. Each object mask image is then magnified by an arbitrary amount ($\sim 30\%$) to ensure that *all* the light from the objects is included in the mask. The construction of the sky frame outlined previously is then repeated for each frame, but this time (using a program code kindly supplied by R.F. Peletier) the mask frame is used to identify objects and to replace them with interpolated sky values before smoothing and block-averaging is carried out.

An additional complication with this dataset was that conditions varied dramatically from night to night; only the first and fourth nights were photometric, with light to heavy cirrus affecting the remainder of the run. To account for this, the magnitude of an unsaturated star present in all the frames and the noise in the sky were monitored throughout each night and this was used to weight each frame by signal/noise^2. The noise in the final frame agrees with the expectations of Poisson statistics, and the magnitude of the stacked reference star agreed well with the measurements from individual photometric observations, indicating that the photometric data had been included correctly in the final stack.

4.3 Object detection and photometry

To detect objects on our deep H-band image we use a procedure very similar to that outlined in Section 2.2.3. For our final catalogue, an object with a total magnitude of $H = 22.5$ give a 3σ signal inside a $0.9''$ radius aperture. There are

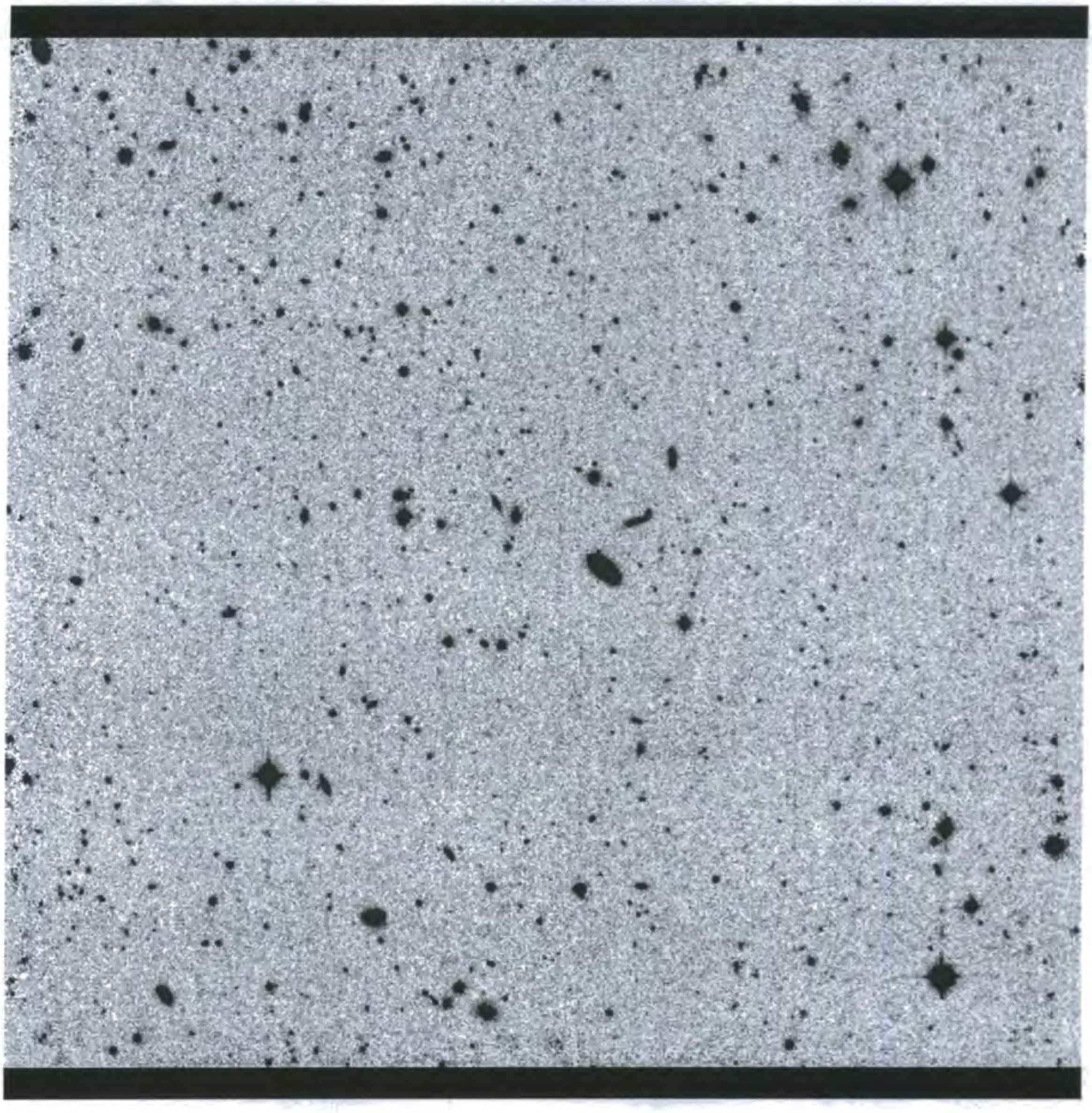

Figure 4.3: An greyscale image of the final reduced Calar Alto deep $H-$ band image. The 3σ detection limit in a $0.9''$ radius aperture on this frame $H = 22.5$. The scale is $0.40''$ pixel^{-1}. There are ~ 2000 sources to this limit, over an area, after trimming, of 45 arcmin^2. Seeing FWHM on this image is $\sim 0.8''$.

a total of 1979 galaxies in this catalogue which covers an area of 45 arcmin^2.

4.4 Results

4.4.1 $H-$ band galaxy number counts

In Figure 4.4 we show our H- band galaxy number counts measured in the WHDF (filled symbols) as well as counts from the literature. Currently, the deepest near-infrared number counts are not from ground-based observatories but from the Hubble Space Telescope. When the observatory was refurbished in 1997, a near-infrared capability was added to it in the form of the Near Infrared Camera and Multi-Object Spectrograph, NICMOS (Thompson et al. (1998a)). NICMOS is a "first-generation" infrared camera in that it has a relatively small field of view and a low pixel count; the camera consists of three 256^2 HgCdTe detectors. Unfortunately, because of a thermal short in the NICMOS dewar, the on-orbit lifetime has been shortened substantially, moreover this fault has also meant that it is not possible to focus all three cameras simultaneously, reducing the available field of view to < 1 arcmin^2. Also, because the HST is not a cooled telescope, the high thermal background means that observing at K is very inefficient; deeper observations at H are possible.

Space-based $H-$band observations do, however, have an important advantage over ground-based ones: because HST is above the Earth's atmosphere, the absence of night-sky OH lines in this wavelength range means the background is *much lower* than observed from ground-based telescopes. On-orbit sky brightnesses measured with NICMOS are typically $\sim$ 24 mag arcsec^{-2} (Yan et al. 1998). By comparison, with Omega-prime we measured a sky brightness of $\sim$ 14 mag arcsec^{-2}.

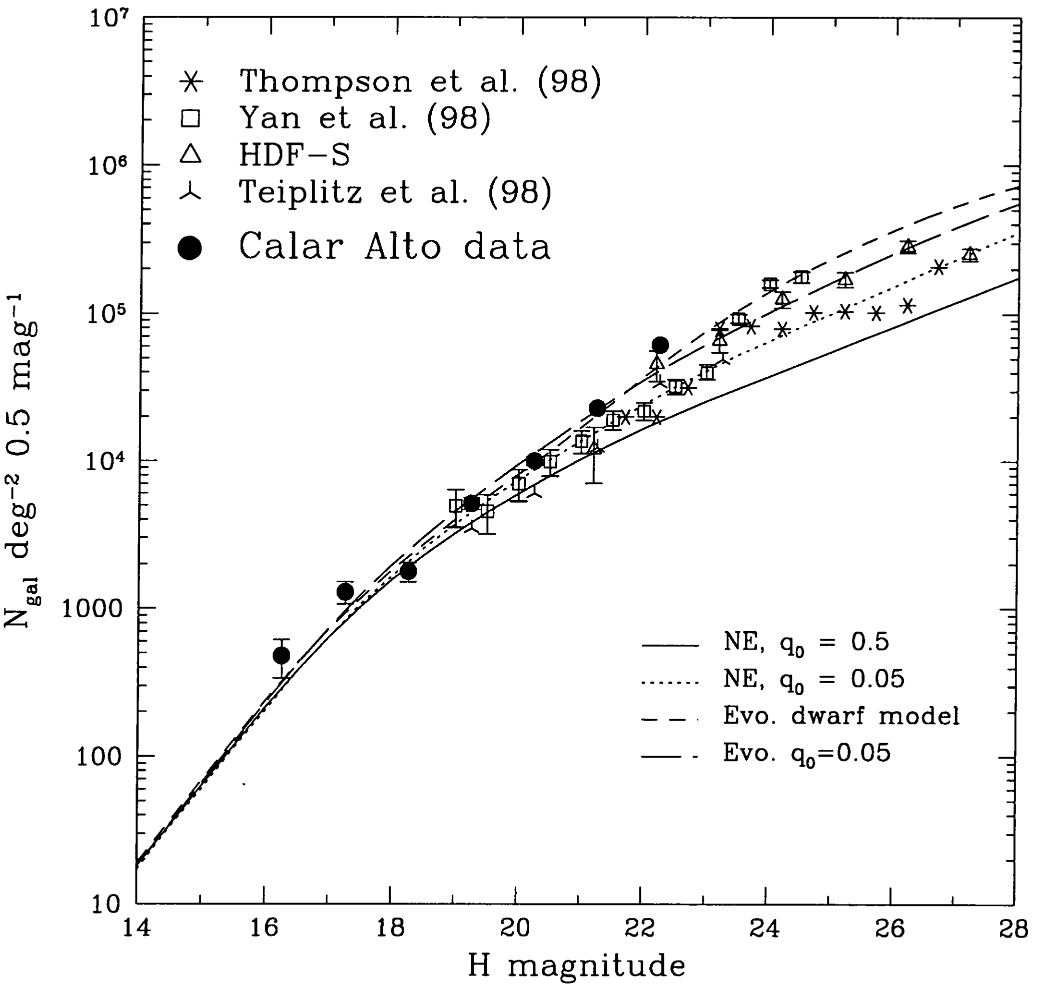

Figure 4.4: $H-$ band numbers counts from the literature (open symbols) and from our current work (filled symbols). A correction has been applied to the number counts of Thompson et al. using their supplied incompleteness corrections. Also shown are the predictions of four models – a low- and high- q_0 non-evolving model (solid and dotted lines respectively), and two evolutionary models, described in the text (long dashed and short dashed lines).

Both sets of H counts taken from the literature are derived from HST observations. The Yan et al. (1998) counts are based on NICMOS parallel mode imaging, and as such are taken in while other instruments on the telescope image a primary target. For this reason they span a variety of exposure times and galactic latitudes. The Yan et al. survey covers ~ 9 arcmin^2 with 3σ depths ranging from $H \sim 24$ to $H \sim 25.5$. In contrast, Thompson et al. (1998a) have a single pointing in a sub-area of the HDF and reach 3σ depths in a very small field of ~ 1 arcmin^2 of $H = 27$. We have adjusted their number counts by using their supplied incompleteness corrections. In Figure 4.4 we also plot H-band counts derived from the Hubble Deep Field South (HDF-S) observations. Object detection and photometry procedures identical to those used with the Calar Alto dataset were carried out with these observations. The HDF-S H-band observations consist of a single pointing of the NICMOS camera for a total integration time of 35.7 hours.

In Figure 4.4 we plot the predictions of several variants of our evolutionary and non-evolutionary models. In both cases, we adopt the normalizations and star-formation histories outlined in Section 2.4. The solid and dotted lines on this graph show the predictions of the $q_0 = 0.5$ NE model and $q_0 = 0.05$ NE models respectively. Our observations, as they have a much larger area than the HST-based counts, reach much brighter magnitudes ($H \sim 16$); our errorbars are also correspondingly smaller.

It is apparent from Figure 4.4 that faintwards of $H \sim 20$, our number counts are higher than the predictions of the $q_0 = 0.5$ NE model; beyond $H \sim 21$, our counts are above the $q_0 = 0.05$ NE model as well. The faint end of the $K-$selected counts has already hinted at a similar trend, as illustrated in Figure 2.3. Our current survey, however, covers a much greater area in comparison to these works - at $H \sim 22$ we have $\sim 20-30$ times the area of comparable studies in K.

At brighter magnitudes our work agrees with the published counts; until $H > 22$, the Yan et al. points track the NE $q_0 = 0.05$ model, before jumping abruptly at $H \sim 23$ after which point they agree with our observations; we speculate that at brighter magnitudes the variance on Yan et al.'s (and those of Thompson et al. (1998b) as well) measurements must be larger than the errorbars suggest. We also consider the alternative dwarf-dominated $q_0 - 0.5$ model proposed in Metcalfe et al. (1996). In this "disappearing dwarf" model, the dwarf population has constant star-formation rate at $z > 1$ and fades rapidly at $z < 1$. However, from the Figure, it appears that our standard evolutionary PLE model (long dashed lined) reproduces the observed number counts well.

Of course, the *optically* selected number counts diverge from the $q_0 = 0.5$ NE model too at around $B \sim 20$, when the effects of evolutionary brightening become significant. And at near-infrared wavelengths we expect the morphological mix to become spiral dominated faintwards of $K \sim 20$, so it is not too surprising that the counts should be above the predictions of the non-evolving $q_0 = 0.5$ model, which after all fails to reproduce the number counts correctly in all other bandpasses. The amount of passive evolution in H must still be small by $H \sim 22$ however, given that our observations are close to our $q_0 = 0.05$ evolutionary model which has been specially tuned to reduce the amount of passive evolution. Furthermore, the angular correlation function of this sample, discussed in Section 5.3.1, appears also to favour an essentially non-evolving redshift distribution at these depths. Finally, we note that none of our models require a steep slope to the faint end of the galaxy luminosity function in order to match the observed counts.

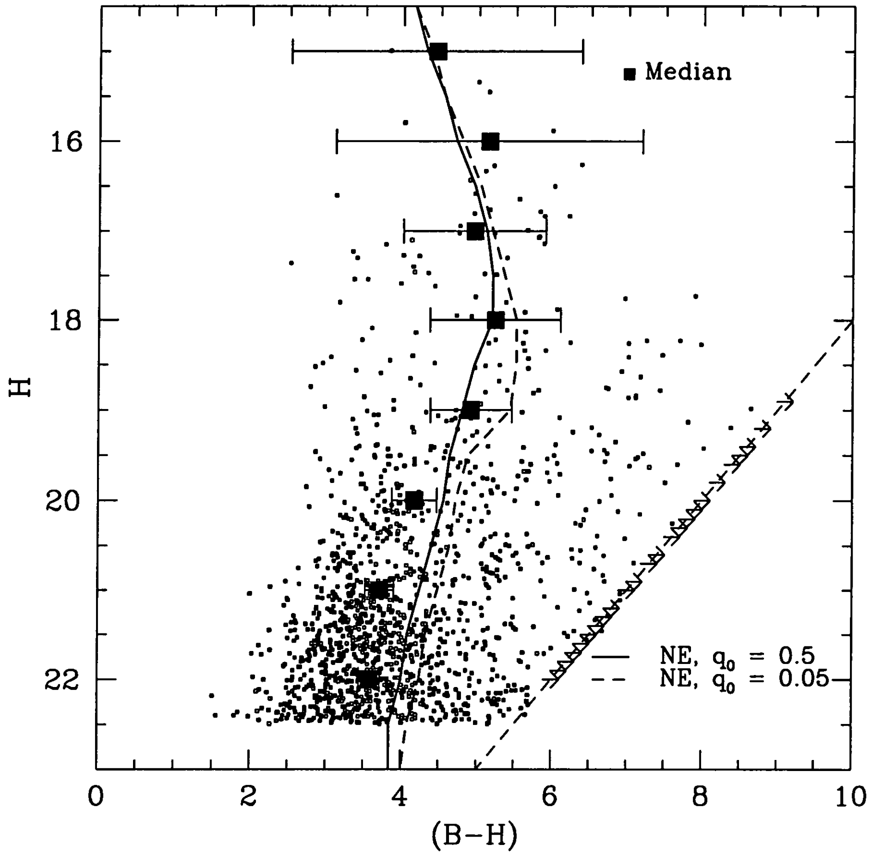

Figure 4.5: $H-$ magnitude against $(B-H)$ colour for galaxies in the WHDF, with median colours calculated in one magnitude bins with bootstrapped error bars. Two non-evolving models are shown; one for $q_0 = 0.05$ (dotted line) and one for $q_0 = 0.5$ (solid line). Right-pointing arrows show non-detections.

4.4.2 Optical-infrared colours

Figure 4.5 and Figure 4.6 show optical-infrared colours for $H-$selected objects in the WHDF. In Figure 4.5 we plot $(B-H)$ colour against H magnitude for all objects to $H < 22.5$; also shown are median colours (filled squares) with bootstrap errors, and the predictions of two non-evolving models for low and high q_0 (dotted and solid lines respectively). The dashed line shows the region of incompleteness. Figure 4.6 is identical to Figure 4.5 except that in this case we plot $(I-H)$ as a function of H magnitude. The right-pointing arrows on both plots indicate objects detected in H but not detected in I or B; in B there are 14 such objects, whereas in I there are 18.

In Figure 4.5 the same trend already observed in our $(B-K)$ vs K diagram (Figure 2.4) is apparent; the $(B-H)$ colour becomes steadily redder until $H \sim 18$ after which point it turns bluewards and this trend continues to the the limit of our survey. By $H \sim 22$, the data is ~ 0.5 mag bluer than the non-evolving prediction. The $H-$ vs $(I-H)$ plot follows a similar trend, with the median colours becoming bluer than the model predictions by $H \sim 18$. It is apparent from this graph that the Calar Alto dataset is a considerable advance over our old UKIRT wide survey, which was limited at $K \sim 20$. This work effectively extends our 3σ limit two magnitudes fainter with the same areal coverage and with reduced photometric errors.

Does this improved data-set allow us to comment on the possible existence of the "hole" in the optical-infrared colour-magnitude diagram, first commented in Chapter 2? There are very few galaxies in Figure 4.5 which have $H \sim 22$ and $(B-H) \sim 6$, which is the approximate location of this feature.

Figure 4.7 shows $(B-R)$ *vs* $(R-H)$ for all galaxies in the WHDF, as well as the colour tracks predicted by the models. In this plot, galaxies have

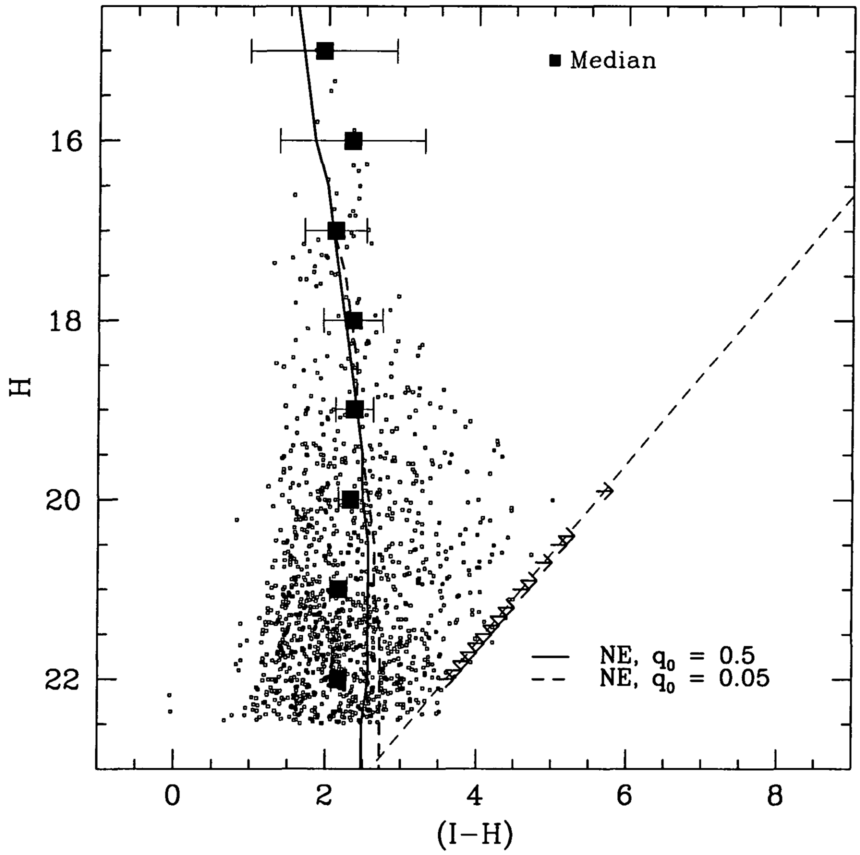

Figure 4.6: As in Figure 4.5, but instead H magnitude against $(I - H)$ colour is plotted.

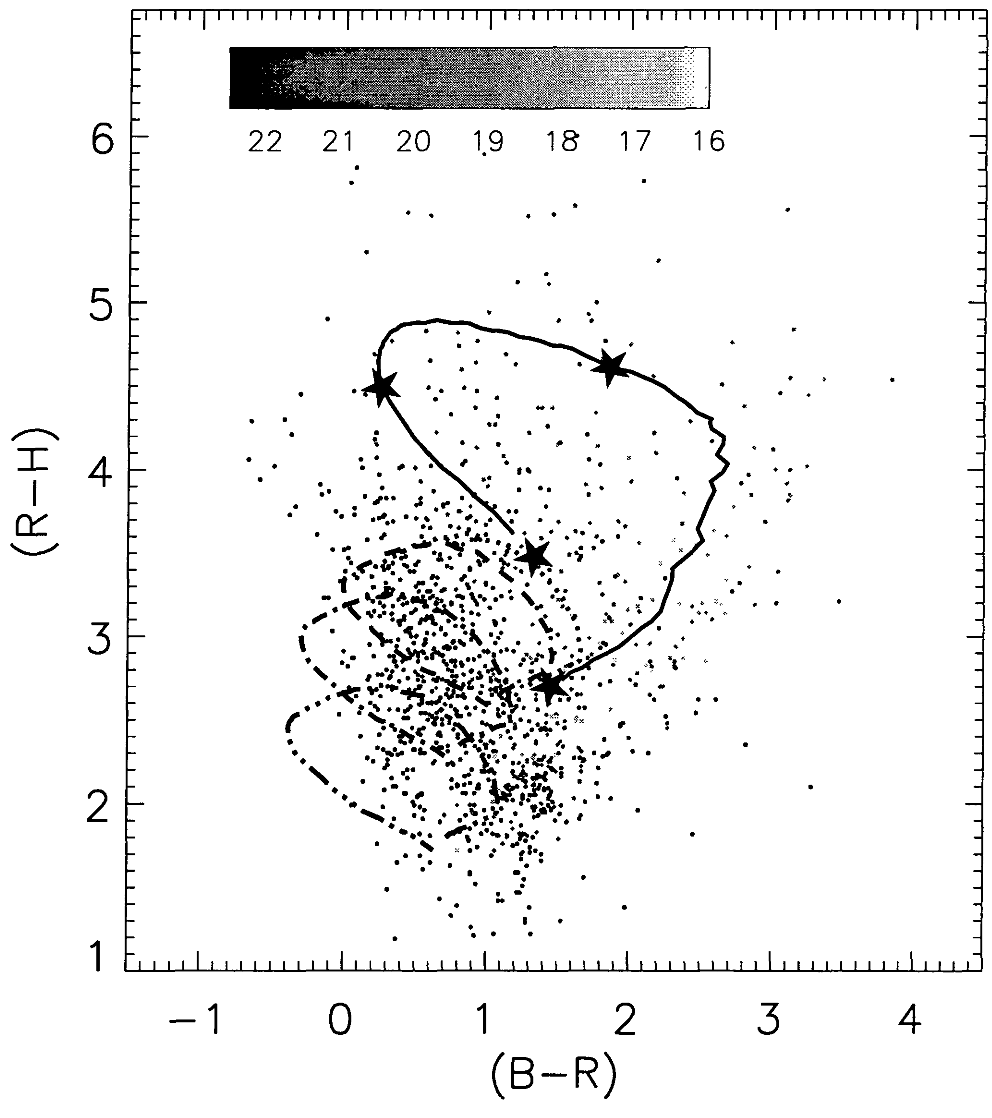

Figure 4.7: $(B - R)$ vs $(R - H)$ for all for all galaxies to $H < 22.5$. Galaxies are shaded in proportion to their magnitude; darker symbols represent fainter galaxies. Also shown are the Bruzual and Charlot tracks for E/S0 galaxies (solid line), Sab galaxies (dotted) line, Sbc, Scd, and Sdm galaxies (dashed, dot-dashed and dot-dot-dashed lines respectively). Redshift intervals of $z = 0, 1, 2, 3$ are marked with stars.

been shaded in proportion to their magnitude; darker symbols represent fainter galaxies. From this it is apparent that the faintest galaxies lie in the region of this plot occupied by spiral galaxies, as we have seen previously in Figure 2.5. In this plot, however, the transition from colours consistent with low-redshift elliptical galaxies to higher-redshift spiral galaxies is much more apparent than in our previous work.

Despite our much higher photometric precision in this work, there is still a large scatter in the colour-colour plane, with galaxies distributed over a broad range of optical-infrared colours and only approximately covering the region of the plot occupied by our tracks.

4.5 Interpretation and discussion

In this Section we will discuss and interpret our results in the context of the models we have previously presented in Chapter 2. We begin with a consideration of the H-selected optical-infrared colour distributions, and a comparison of these to our evolutionary and non-evolutionary models.

4.5.1 Colour distributions and red outliers

In Figure 4.9 and Figure 4.8 we present the $(I-H)$ and $(B-H)$ colour distributions for objects in the WHDF selected by $H-$ magnitude in four one-magnitude slices from $18 < H < 19$ to $21 < H < 22$. In both graphs the arrows represent the incompleteness limits of the B and I catalogues. The open boxes indicate how many objects are undetected in each magnitude slice. The dashed line shows the predictions of a non-evolving model, whereas the solid line shows the predictions from the $x = 3$ evolutionary model. The dotted lines shows the position of the elliptical galaxies (types E/S0 and Sab) in the $x = 3$ model.

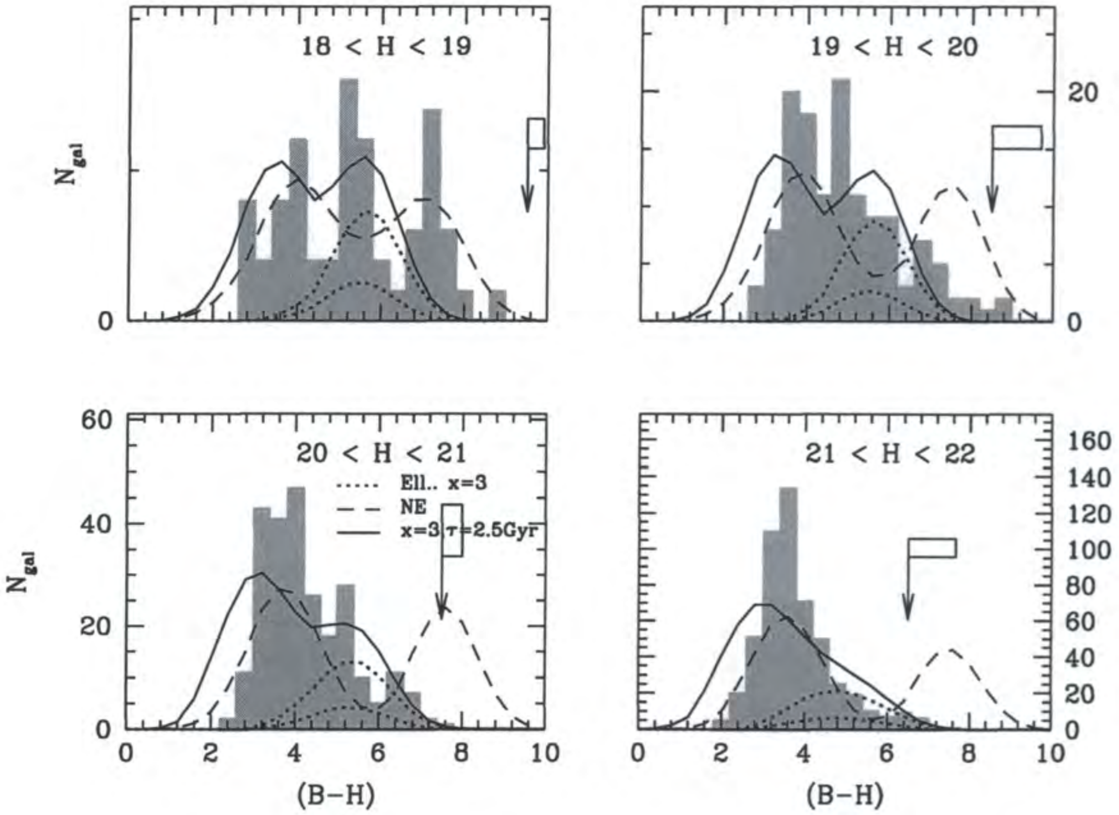

Figure 4.8: $H-$ selected $(B - H)$ distributions; arrows show the completeness limit . The lines show the predictions of various evolutionary models described in the text. The dotted lines shows the distribution of elliptical galaxies (E/S0 and Sab) in the $x = 3$ model.

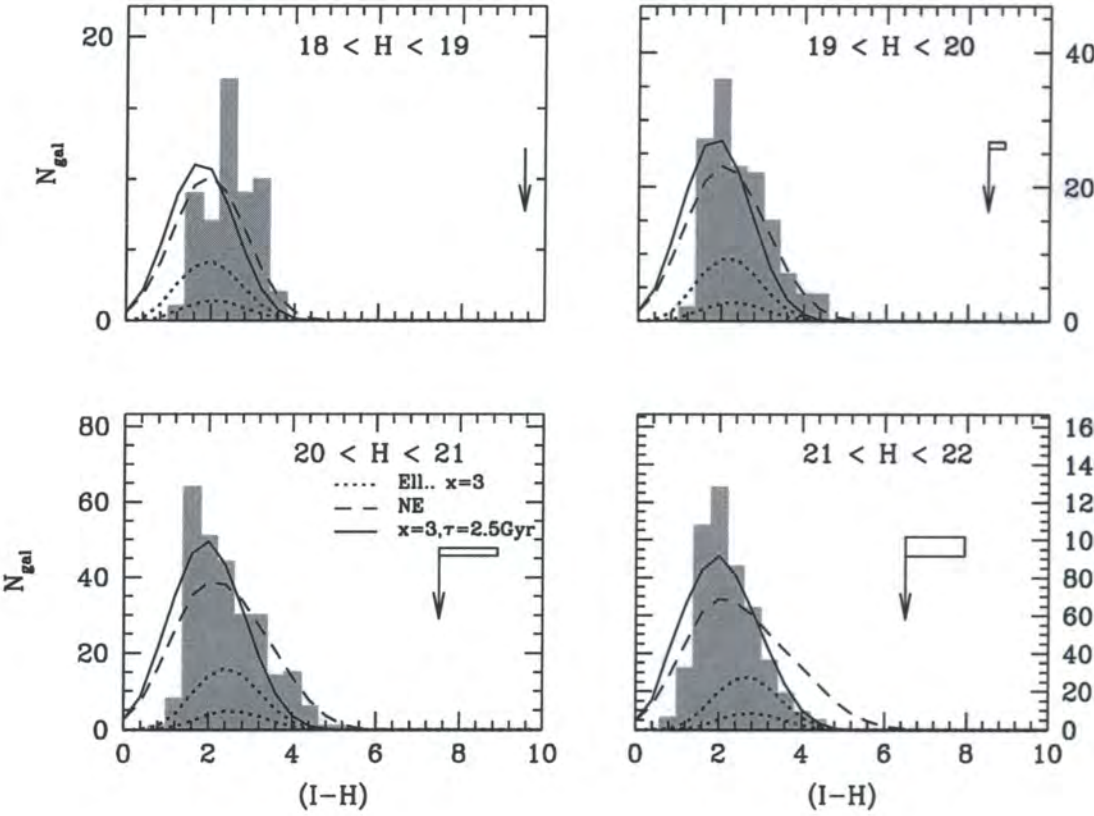

Figure 4.9: $H-$ selected $(I-H)$ distributions for the Calar Alto dataset. All symbols are identical to Figure 4.8.

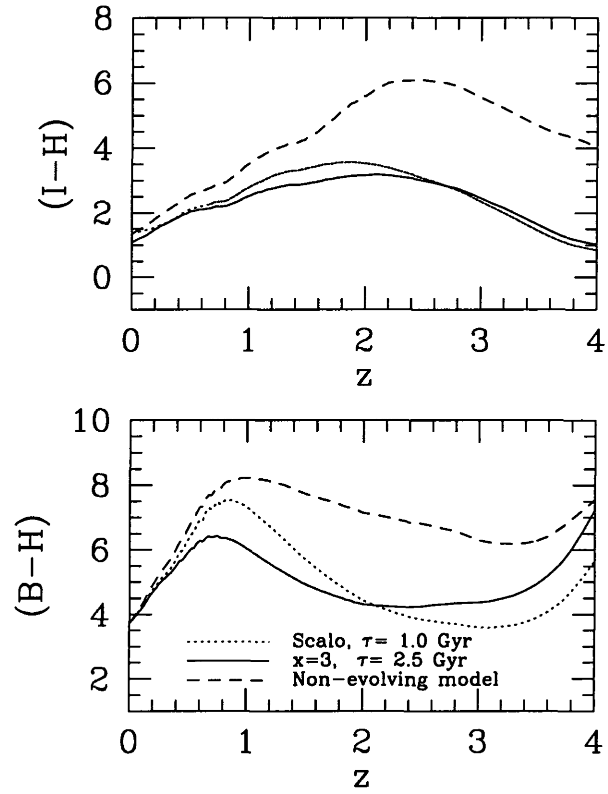

Figure 4.10: $(I-H)$ colour (upper panel) and $(B-H)$ colour (lower panel) as a function of redshift for a variety of star-formation histories and IMFs: non evolving (dashed line), $x=3$ IMF, $\tau=2.5$ Gyr (solid line), and $\tau=1.0$ Gyr, scalo IMF (dotted line).

Table 4.1: Numbers of objects with $(I - H) > 3$ per arcmin^2 with $\pm 1\sigma$ errors over the 45 arcmin^2 of the deep H- image.

Author	$19 < H < 20$	$20 < H < 21$	$21 < H < 22$
Model ($x = 3$)	0.3	0.8	1.8
Model (NE)	0.6	1.7	4.1
This work	0.7 ± 0.1	1.7 ± 0.2	2.4 ± 0.2

These diagrams confirm the broad conclusions already presented in Chapter 2; once again, we find that the numbers of extremely red, unevolved objects present in these distributions are extremely small. In Figure 4.10 we plot $(I - H)$ and $(B - H)$ colour as a function of redshift. A non-evolving galaxy track (i.e., a pure k-correction) reaches $(I - H) \sim 6$ by $z \sim 2$, or $(B - H) \sim 8$ by $z \sim 1$. Our survey shows a conspicuous lack of such objects. This is clearly seen in Figure 4.8 where the dashed line represents the colour distributions expected from a non-evolving population; the bump visible at $(B - H) \sim 8$ corresponds to the population of unevolved ellipticals present in these models.

In Table 4.1 we compare our Calar Alto observations of objects with $(I - H) > 3$ with the predictions of our models. This Table is directly comparable to Table 2.5 in which we presented numbers of objects with $(I - K) > 4$; now, however, we have many more objects. In the present case we select a colour of $(I - H) \sim 3$ as being roughly representative of an elliptical galaxy at $z \sim 1$. Once again, the same broad trend which we have observed previously we see here. However, the smaller wavelength baseline between I and H (as opposed to I and K) results in correspondingly smaller evolutionary effects. Our observed numbers of objects with $(I - H) > 3$ is greater than our non-evolving predictions only in our faintest bin, $21 < H < 22$. This is apparent in the observed H-selected $(I - H)$ distributions shown in Figure 4.9; only in the faintest slices do the evolving and non-evolving distributions diverge. However, the discrepancy

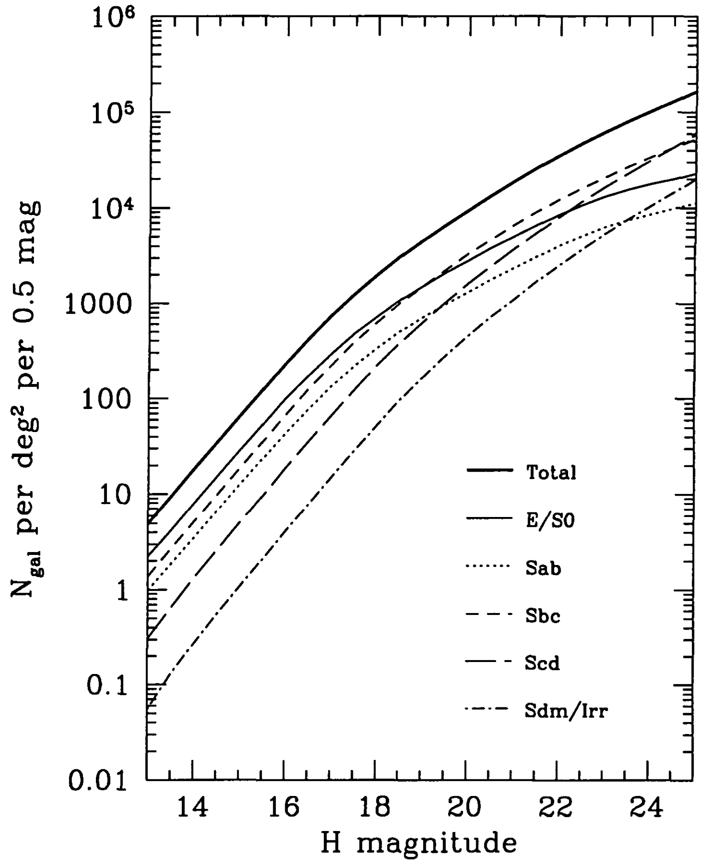

Figure 4.11: H-band number-magnitude relation as a function of morphological type for the evolutionary ($x = 3$) model. The heavy solid line shows the total predicted galaxy count.

between the observations and the non-evolving model for the $21 < H < 22$ slice is substantial, given the small errorbar on our measured numbers of $(I - H) > 3$ objects.

Finally, the large numbers of objects in our faintest $21 < H < 22$ slice potentially allows us to investigate further the rapid narrowing of the H-selected optical-infrared colour distributions towards fainter magnitudes. In Figure 4.11 we show H-selected differential galaxy number counts for the $x = 3$ evolutionary model as a function of morphological type; the heavy solid line indicates the total galaxy count. From this graph it is apparent that the elliptical counts flatten at

$H \sim 19$; faintwards of this limit spirals dominate. In Figure 4.8 and Figure 4.9 we the dotted line shows the location of these elliptical types in the colour-colour space. From these plotsit is apparent that the median $(B - H)$ (and $(I - H)$) elliptical colours for the $x = 3$ evolutionary model move bluewards quite slowly; from the $18 < H < 19$ to the $21 < H < 22$ slice the colours change from $(B - H) \sim 5.6$ to $(B - H) \sim 4.8$. Over this interval the ratio of elliptical galaxies to all galaxies moves from 0.4 at $18 < H < 19$ to 0.3 at $21 < H < 22$. Given that our final slice at $21 < H < 22$ shows an *absence* objects at $(B - H) \sim 4.8$, and is in fact in general narrower than the predictions of our evolutionary model, this would argue that more rapid evolution in $(B - H)$ is required rather than an alteration of the elliptical galaxy luminosity function parameters.

4.6 Conclusions

In this Chapter we have presented results from a H-band near-infrared survey of the WHDF. Our catalogue reaches $H(3\sigma) = 22.5$ in a $0.9''$ radius aperture and covers 45 arcmin^2. Our main conclusions from this Chapter are broadly similar to those outlined in Chapter 2.

- Our $H-$ selected number counts are consistent with the predictions of a $q_0 = 0.05$ non-evolving model; however, in the faintest bin we do detect some evidence of evolution. The large area and depth of the survey means our errors are much smaller than previous works (such as our UKIRT deep survey outlined in Chapter 2). The very faintest counts from the NICMOS camera are compatible with a "disappearing dwarf" $q_0 = 0.5$ model.

- Our survey shows a deficit of red, early-type galaxies. In the H-selected $(I - H)$ distributions there are only 2.4 ± 0.2 objects per arcmin^2 at $21 <$

$H < 22$ observed, compared with the value of 4.1 expected from the non-evolving models. We interpret this deficit as as evidence of on-going star-formation in the early-type galaxies in our sample.

Chapter 5

Galaxy clustering in the WHDF

5.1 Introduction

5.1.1 Surveying the Universe

In 1967 at Lick Observatory, astronomers Shane and Wirtanen completed what was then the most extensive and detailed mapping of the sky. Their survey consisted of 1246 photographic plates each of which covered six square degrees of sky. On every plate, galaxies were painstakingly counted in 10 arc-minute square cells. When these cells were plotted with intensities proportional to the numbers of galaxies in each, one fact became clear — galaxies were *clustered.* Shane and Wirtanen's galaxies were not spread thinly and evenly across the sky — instead they were clumped together in long sheets and filaments, and there were large areas on the plates where the numbers of galaxies were very low. This pattern of voids and filaments has been seen in every large survey conducted since then.

The human eye is very adept at finding patterns and this can make interpreting these observed galaxy distributions a hazardous affair, if one is not equipped with quantitative and reliable metrics. A major step forward in our ability to characterize the observations took place in the late 1970's with the appearance of a number of papers which presented a framework which could be used to describe and interpret the data (Peebles 1973; Hauser & Peebles 1973; Phillipps et al. 1978). The most basic estimator introduced was the projected two-point correlation function, commonly denoted by $\omega(\theta)$. This expresses the number of galaxies at given angular separation in excess of what would be expected for an uncorrelated distribution; in such a case, $\omega(\theta) = 0$. When these methods were applied to Shane and Wirtanen's catalogue an important finding was made; over a wide range in angle θ, $\omega(\theta) \propto \theta^{-\delta}$, where $\delta = 0.5 - 0.8$. At very large angular separations, $\omega(\theta)$ was observed to drop rapidly to zero (Groth & Peebles 1977).

With the introduction of automated plate scanning machines in the 1980's (such as Edinburgh's Cosmos machine and the Automated Plate Measuring Facility (APM) at Cambridge), in combination with a large amount of plate material taken at 4m-class telescopes, our knowledge of the distribution of galaxies rapidly expanded (Shanks, Fong, & Ellis 1980; Koo & Szalay 1984). These plate-based surveys regularly probed to $z \sim 0.3$. The largest of them, the APM galaxy survey, furnished the positions and magnitudes of over two million galaxies (Maddox et al. 1990a).

5.1.2 Deep pencil beam surveys

With the advent of CCD detectors in the late 1980s, measuring the clustering of galaxies to very faint limiting magnitudes became possible and many studies have now been made with CCD-based datasets (Brainerd & Smail 1998; Woods & Fahlman 1997; Hudon & Lilly 1996; Brainerd, Smail, & Mould 1994; Roche et al. 1993; Efstathiou et al. 1991). Although such surveys until recently have covered a much smaller area than their plate based-predecessors, they have been able to probe to much fainter limiting magnitudes and correspondingly higher redshifts; typically, photographic plates have quantum efficiencies of a few percent, whereas many modern CCD detectors have quantum efficiencies greater than ninety percent in the same region of the spectrum. Moreover, higher photometric accuracies are possible with electronic detectors. In the $B-$band, our WHDF reaches reaches four magnitudes fainter than the limit attainable with photographic plates. In recent years, CCD mosaic cameras such as the Canada-France-Hawaii 12K camera have offered the promise of combining the photometric accuracy of CCD-based studies with the areal coverage of earlier works.

One significant discovery which resulted from the extension of galaxy clustering measurements to deeper limits with CCD-based data was the discovery that at $B \sim 24$, the measured clustering amplitude dropped sharply below the predictions of the standard non-evolving model. To reconcile this observation with the results from redshift surveys of that time required that the galaxy population responsible for the number count excess was weakly clustered (Efstathiou et al. 1991; Brainerd, Smail, & Mould 1994; Infante & Pritchet 1995). Our clustering measurements of the WHDF, combined with our models which reproduce the observed redshift distribution of the deepest redshift survey to date (Cowie, Songaila, & Hu 1996) suggest an alternative explanation which we will discuss in Section 5.4.

5.1.3 The growth of structure

A large amount of observational evidence now suggests that a high fraction ($>$ 90%) of the total matter in the universe is unobservable, or dark. The precise nature of this dark matter remains somewhat of a mystery, but it has become clear that investigating how structures form in the universe can give us important clues concerning the properties of the dark matter. In parallel with the observations outlined above, several important theoretical advances were made in explaining the growth of structure in the Universe and its origin as the result of very small gravitational instabilities in the homogeneous Big Bang, and the role that the dark matter had in these models. The discovery by the COBE satellite of the imprint of these primordial potential fluctuations on the microwave background radiation provided a confirmation of one of the fundamental tenets of the theory (Smoot et al. 1992).

However, the formation of small-scale structure under the influence of gravity is a highly non-linear process and to model this required the development of large numerical simulations to follow the gravitational collapse of matter and its formation into dark matter halos. These simulations took place in the context of the hypothesis that the dark matter consisted of cold collisionless particles (Peebles 1982), and one of the early successes of this technique was that it was able to rule out variant theories which posited that the dark matter was hot, i.e., consisted of relativistic particles like neutrinos (White, Frenk, & Davis 1983).

This cold dark matter (CDM) hypothesis has been tested repeatedly in the past decade-and-half and the simulations have grown steadily larger (for instance, the recent simulations of Jenkins et al. (1998) contain 17 million particles) and have begun to incorporate gas as well as dark matter. Despite the deficiencies of the theory (for example, the standard CDM model under-predicts the amount of clustering seen in large galaxy surveys like Maddox et al. (1990b) and Groth & Peebles (1977) at $\sim 20h^{-1}$ Mpc by factors of a few) it remains our best description of the evolution of the distribution of dark matter. Several variants of the standard model now exist which produce better predictions for large-scale clustering than the standard model. However, making the connection between the clustering properties of the dark matter and the clustering of galaxies observed on the sky is not a straightforward affair, as it involves modelling the process of galaxy formation which, despite the claims of some practitioners in the field, is still a poorly understood process.

5.1.4 Investigating galaxy clustering with the WHDF

The WHDF is a unique dataset with which to study the two-point projected galaxy correlation function. It reaches very deep limiting magnitudes; moreover, as we have imaged extremely deeply in many bandpasses on *the same region of sky* we can investigate how galaxy clustering varies as a function of colour and bandpass selection. Finally, although the WHDF is a small region of sky, it is ~ 10 times larger than the Hubble Deep Field and reaches a similar depth in U and B bandpasses, making it unique in its ability to aid us in the investigation of galaxy clustering to very faint limits. We should be cautious when interpreting our results, however. Typically, our catalogues cover only ~ 50 arcmin^2 and so our work can only provide information about galaxy clustering at approximately $\sim 0.1^\circ$ scales. At $z \sim 2$ for $q_0 = 0.05$ this corresponds to $\sim 7h^{-1}$ Mpc. This means that the errors on the clustering measurements will be sensitive to the effects of cosmic variance. We will discuss and attempt to quantify this source of error in Section 5.3.2.

5.2 Methods and Techniques

5.2.1 Catalogue generation and star-galaxy separation

The catalogues which we use in this Chapter were produced by the same methods outlined in the previous chapters which dealt with Calar Alto and UKIRT datasets. A more detailed description of the data reduction and object detection procedures employed in the optical data discussed here will be presented in a forthcoming paper (Metcalfe et al. 1998). However, to briefly recap: after fitting and removing the sky background, deep isophotal object detection is carried out typically 1 magnitude below the 3σ sky background detection limit of the frame. Following this, Kron (1980)–style magnitudes are calculated using a local sky value for each object found on the frame. For the purposes of measuring the correlation function, masks files were also constructed to cover regions containing bright galaxies or stars. The area of the field affected by such bright objects is less than 10% of the total.

To carry out star-galaxy separation we begin by defining a star-galaxy classifier index as the difference between the total magnitude and that inside a $1''$ aperture (Metcalfe et al. 1991). Applying this estimator to our deep $B-$ frame, stars can be separated from galaxies reliably to $B \sim 24$, after which point faint stars become indistinguishable from compact galaxies. However, even beyond this limit, optical-optical and optical-near-infrared colour-colour plots were used to identify some very red stars.

As star-galaxy separation for most objects is not possible beyond $B \sim 24$, it is worthwhile to ask what fraction of our deepest catalogue could be composed of stars, as the unclustered stellar population will result in our correlation function estimates being biased lower than their "true" values. In Figure 5.1, we plot differential star-counts in the WHDF against $B-$band magnitude. The slope of the dashed line fitted to these star counts in the range $16.5 < B < 23.5$ is $\gamma \sim 0.1$, in good agreement with the value derived by Reid et al. (1996) in a study of stars in deep Keck imaging data. In the range $24 < B < 28$, there are $\sim 0.5 \times 10^5$ objects deg^{-2} (stars and galaxies) in the WHDF; extrapolating our measured stellar counts faintwards from $B \sim 24$ to $B \sim 28$ we find that at $B \sim 28$, stars comprise $< 5\%$ of the total population. Furthermore, this number should be treated as a conservative upper limit, as in all likelihood the stellar counts do not continue to rise to these faint limits but instead flatten off (Reid

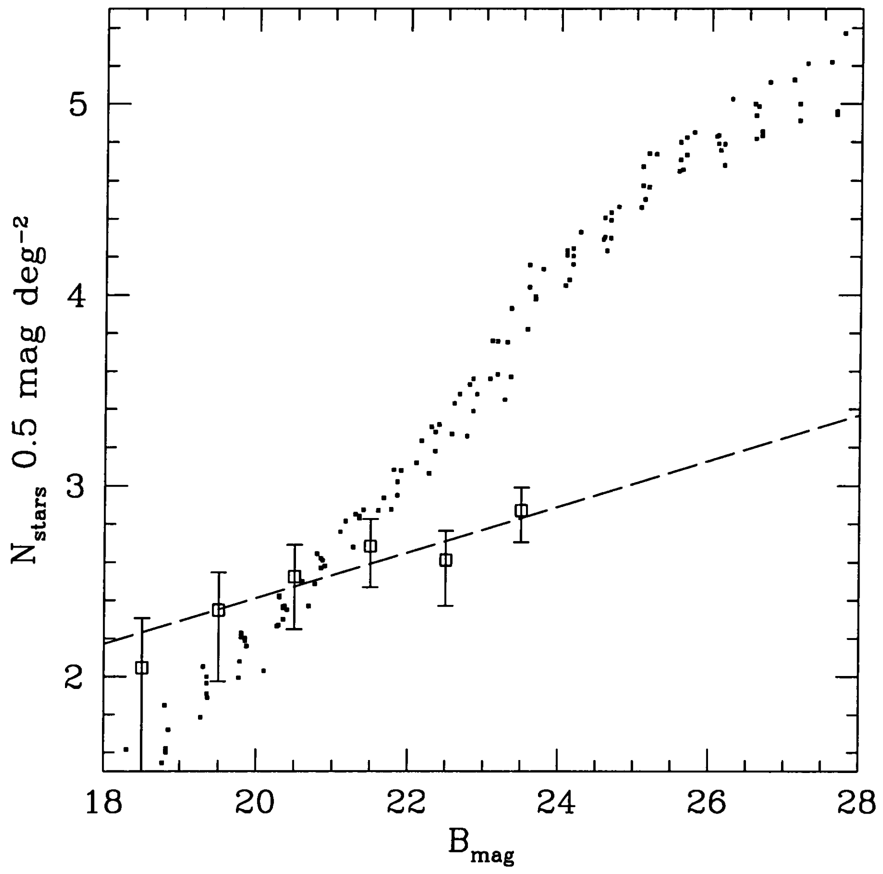

Figure 5.1: Differential star counts in the WHDF (open squares) against $B-$magnitude with $\sqrt{N}$ error bars. The fitted line, extrapolated to the $B < 28$ limit of our data, has slope 0.1 Also shown is a compilation of $B-$band galaxy number counts (small filled squares).

et al. 1996; Couch, Jurcevic, & Boyle 1993; Bahcall & Soneira 1980).

How significant is this level of contamination to our correlation function measurements? For a catalogue which contains N_{obj} objects and N_s unclustered stars with an uncorrected correlation amplitude A_ω', the "true" value of the fitted correlation amplitude is given by $A_\omega = A_\omega' N_{obj}^2 (N_{obj} - N_s)^{-2}$. If $N_s = f_s N_{obj}$ this equation reduces to $A_\omega = A_\omega'(1 - f_s)^{-2}$. Furthermore, this stellar contamination affects all bins equally. Hence our (very conservatively estimated) $\sim$ 5% stellar contamination will result our measured correlations being $\sim$ 90% of the 'true' value. Since this correction is so small (indeed it is smaller than the error bars on our fitted correlations) we have chosen not to apply it. Applying these considerations to our catalogues from other bandpasses leads us to the same conclusion.

5.2.2 Determining the angular correlation function

The angular correlation function $\omega(\theta)$ measures the excess number density of objects over a random distribution in an annulus of width $\theta + \delta\theta$. Typically, measurements are made over a range of angular separations. As our data is extremely deep, and therefore may probe to very high redshift, the amplitude of galaxy clustering in our samples is small as the projection effects are very large. Therefore, it is essential that we use a method to measure $\omega(\theta)$ which minimizes biases introduced by edge effects, the finite (and small) size of our survey, and the geometry of our masks. It is for this reason we chose to use the estimator of Landy & Szalay (1993), given in equation 5.1. Here we follow the usual notation where DD indicates the number of galaxy-galaxy pairs, DR galaxy-random pairs and RR random-random pairs for a given angular separation and bin width:

$$\omega(\theta) = \frac{\mathrm{DD} - 2\mathrm{DR} + \mathrm{RR}}{\mathrm{RR}} \tag{5.1}$$

We find that, for a given survey sample, amplitudes measured by this estimator are very similar to those computed with the Hamilton (1993) estimator, $\omega(\theta) = (DDDR/RR^2)$. The $1 - DD/DR$ estimator, as used by Roche et al. (1993), gives consistently higher (at the 20 – 30% level) values for $\omega(\theta)$, over all our bins. This has been found by other authors and is indicative of the known biases inherent in this estimator (Hamilton 1993; Landy & Szalay 1993).

For each magnitude-limited sample of each catalogue, $\omega(\theta)$ is computed using equation 5.1 for a series of bins spaced in increments of 0.2 in $\log(\theta)$, where

θ is in degrees. As we have only observed one field we cannot use the field-to-field variance to estimate the errors in each bin; instead we implement a bootstrap-resampling technique (Ling, Barrow, & Frenk 1986; Barrow, Sonoda, & Bhavsar 1984). In this method, the error in each bin is computed from the variance of the estimator as applied to a large ($\sim$ 50) number of bootstrap-resampled catalogues. As expected, these bootstrap errors are larger than the normal $\sqrt{N}$ Poisson counting errors.

To allow comparison with other workers, we fit our measured correlations as a function of angular separation to an expression of the form

$$\omega(\theta) = A_\omega(\theta^{-\delta} - C) \tag{5.2}$$

where A_ω is the amplitude of $\omega(\theta)$ at 1° and C is the "integral constraint" term. This term is a bias which arises because we are using each catalogue to determine the mean galaxy density. This would be a valid approach if galaxies were unclustered (i.e., uniformly distributed); however, they are not, and we must correct for this. This term is particularly significant in our work because the area which we survey is quite small. To calculate the integral constraint we use the expression

$$C = \frac{1}{\Omega^2} \int\int \omega(\theta) d\Omega_1 d\Omega_2 \tag{5.3}$$

where θ is the angular separation of each galaxy pair and $d\Omega_1$ and $d\Omega_2$ the solid angle subtended by each pair. If we assume a power-law correlation function, $\omega(\theta) \propto \theta^{-0.8}$ we may calculate this quantity for our fields by direct integration. Typically we find $C \sim 13A_\omega$.

The error on A, the overall fit, is determined from the method of Marquardt (1963), as described in Press et al. (1986). This method combines errors on each bin in an independent manner to calculate the total error of the fit. In order compare the results of our fitting with other workers, we take $\delta = 0.8$. Figure 5.2 shows fits made for the $B-$band catalogue.

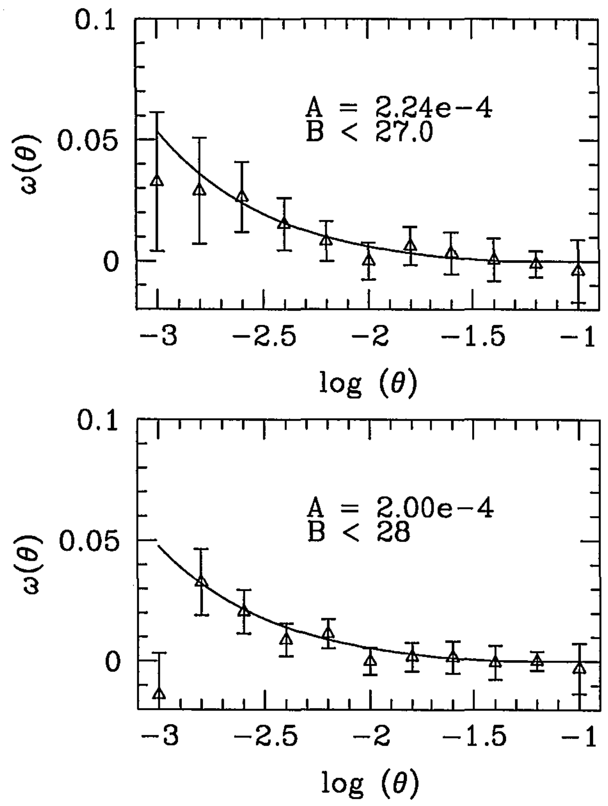

Figure 5.2: $\omega(\theta)$ as measured for samples limited at $B < 27^m$ and $B < 28^m$. The solid line shows the fit to $\omega(\theta) = A_\omega(\theta^{-0.8} - C)$ where C is the "integral constraint" term described in the text and A_ω is the value of $\omega(\theta)$ at 1°

5.2.3 Modelling the correlation function

We would like to compare our measured correlation amplitudes with those of model predictions. In order to do this we must de-project our observed correlation function by assuming a functional form for the spatial correlation function. From the results of large surveys (Maddox et al. 1990c; Davis & Peebles 1983; Groth

& Peebles 1977) it is found that $\xi(r)$ (the spatial correlation function) is well approximated by $\xi(r) = (r_0/r)^\gamma$, at least for scales $< 20h^{-1}$ Mpc. Projecting a model for $\xi(r)$ involves integrating this function over redshift space using Limber's formula (Limber 1953), employing the methods outlined in Groth & Peebles (1977) and elaborated in many recent observationally-motivated papers which have investigated the clustering of faint galaxies (Brainerd, Smail, & Mould 1994; Brainerd & Smail 1998; Roche et al. 1993; Infante & Pritchet 1995; Efstathiou et al. 1991).

In these models the amplitude of the correlation function scales with redshift in the following manner,

$$\xi(r,z) = \left(\frac{r_0}{r}\right)^\gamma (1+z)^{-(3+\epsilon)} \tag{5.4}$$

where r_0 is the correlation length at $z = 0$ and r is the proper distance. To clarify the behavior of the correlation function with z we may define x_0 as the co-moving correlation length for which $\xi(x_0, z) = 1$; from this we have

$$x_0 = r_0(1+z)^{-(3+\epsilon-\gamma)/\gamma} \tag{5.5}$$

Note that if instead we express the evolution of $\xi(r, z)$ in *proper* co-ordinates, $r_0(z)$, the correlation length measured by observers at a given epoch becomes

$$r_0(z) = r_0(1+z)^{-(3+\epsilon)/\gamma} \tag{5.6}$$

In the above formalism, the correlation length will evolve as $(1+z)^{-1}$ even if the clustering pattern is fixed in co-moving co-ordinates.

Turning to the task of deriving an expression for $\omega(\theta)$, the projected correlation function, we note that for small angles, the relation between $\omega(\theta)$ and $\xi(r)$ becomes (Efstathiou et al. 1991)

$$\omega(\theta) = \sqrt{\pi}\frac{\Gamma[(\gamma-1)/2]}{\Gamma(\gamma/2)}\frac{A}{\theta^{\gamma-1}}r_0^\gamma \tag{5.7}$$

where Γ is the incomplete gamma function, θ is the angular separation, and A is given by

$$A = \int_0^\infty g(z)\left(\frac{dN}{dz}\right)^2 dz / \left[\int_0^\infty \left(\frac{dN}{dz}\right) dz\right]^2 \tag{5.8}$$

and

$$g(z) = \left(\frac{dz}{dx}\right) x^{1-\gamma}F(x)(1+z)^{(-3+\epsilon-\gamma)} \tag{5.9}$$

An expression for $F(x)$ is given in Peebles (1980) and depends on the choice of cosmology.

In the context of this model, there are three values of ϵ which have special importance. Assuming $\gamma = 1.8$, and if the clustering is fixed in co-moving co-ordinates, then clustering does not grow with time and $\epsilon = \gamma - 3 = -1.2$. Alternatively, in the non-linear regime, $\epsilon = 0$. Here (for example) galaxy clusters maintain a fixed physical size and clustering "growth" occurs against the backdrop of an expanding universe, causing the correlations to become diluted. At larger scales, in the linear regime we expect $\epsilon = \gamma - 1$ (for a recent discussion see, for example, Colin, Carlberg, & Couchman (1997)).

From the above we see that, although the two-point correlation function may be measured to much fainter limiting magnitudes than the spatial correlation function (as it does not require redshift information), to properly interpret the results of our work we must attempt to decouple the effects of evolutionary brightening on the correlation function signal by means of an assumed redshift distribution. We compute this using the models outlined in Chapter 2. These redshift distributions agree well with the observations at brighter magnitudes. We will primarily investigate our low-q_0 models as these provide the best fit to the available data (number counts and colours). To fit counts in higher q_0 models requires either merging or the addition of an extra population; both effects could modify the measured correlation amplitudes, especially if the additional population had markedly different clustering properties.

5.2.4 Photometric redshifts and galaxy clustering

The two-point projected correlation function is a blunt instrument. Because it is a *projected* correlation function it measures the clustering of *all* the galaxies summed up along the line of sight; as we shall see, to properly interpret the measured values of $\omega(\theta)$, we must have some estimate of the underlying galaxy redshift distribution. Direct estimators such as the spatial correlation function, $\xi(r, z)$ requires redshifts to be determined for each galaxy and this is costly in telescope time; moreover, the spectroscopic limit is about three to four magnitudes brighter than the photometric limit, reducing the volume which can be probed. A few studies have been carried out using this statistic; in particular, LeFevre et al. (1996) used the Canada France Redshift Survey catalogue to estimate the evolution of galaxy clustering. However, currently these surveys only probe to modest redshifts ($z < 1$) and typically involve small numbers (~ 1000) of galaxies. Furthermore, investigating clustering as a function of galaxy properties such as morphology, luminosity or colour is generally a very difficult proposition as once the samples are segregated the numbers of galaxies involved become very small. This situation is likely to change in the very near future; there are at least four major surveys which have either started or will start in the next year or two that aim to construct very large ($\gg 10,000$) redshift surveys of both the local ($z < 0.3$) and distant Universe (Colless 1998; Le Fèvre et al. 1998; Gunn 1995). When these surveys are complete we will be able to trace the growth of clustering of galaxies over ~ 90% of the age of the Universe with high accuracy.

Photometrically generated redshifts provide an important bridge between the difficult task of spectroscopy and the paucity of information that can be derived from imaging data alone. For this reason they are an important tool with which to gain an understanding of the faint galaxy population. The main technique in the estimation for photometric redshifts involves constructing a crude galaxy spectrum using multicolour imaging; this spectrum is then fitted to a range of *template spectra* and the best-fit spectrum is used to estimate the galaxy's redshift. These template spectra are generated using either model galaxy spectra produced using stellar synthesis codes like those of Bruzual & Charlot (1993) or using empirical templates like those of Coleman, Wu, & Weedman (1980), or some combination of the above. Alternative techniques include using spectroscopic training sets to define an empirical relationship between colours and redshifts (Connolly et al. 1995).

Photometric redshifts are not a new idea, dating back at least to Baum (1962) with more modern descriptions around a decade ago (Loh & Spillar 1986; Koo 1985). Despite this, until recently they had not been either widely accepted or produced any major results. The Hubble Deep Field (Williams et al. 1996), described in Chapter 1, changed this. For the first time, a very deep catalogue of field galaxies in filters covering the whole range of the optical spectrum, from ultraviolet to (via ground-based followup) infrared wavelengths was available.[1] But how reliable were the photometric redshifts determined from this data? Hogg et al. (1998) carried out a "double-blind" test in which photometric redshift practitioners (Gwyn & Hartwick 1996; Lanzetta, Yahil, & Fernandez-Soto 1996; Sawicki, Lin, & Yee 1997; Mobasher et al. 1996; Connolly et al. 1995) were

---

[1] With the addition of the NICMOS camera, described in Chapter 4, a near-infrared capability has been added to the HST. Deep exposures from this camera are now available for the follow-up Hubble Deep Field South observations.

asked to estimate redshifts for HDF galaxies *before* the spectroscopic followup. For more than 68% of the galaxies, the measured error was $\Delta z < 0.1$.

Broadband imaging to locate the Lyman break is a simplified photometric redshift method. In this technique, direct imaging is carried out in three carefully selected filters designed to span the 912Å Lyman discontinuity; almost all but the hottest stars show a rapid drop in flux shortwards of this wavelength, as do theoretical galaxy spectra. Additionally, interstellar absorption by neutral hydrogen also causes significant attenuation. At $z \gtrsim 2.5$ this discontinuity is redshifted into optical bandpasses; therefore, by placing filters either side of this continuum break it is possible to identify candidate high-redshift objects. Searches for high redshift, star-forming objects were carried out using similar techniques in the past (Guhathakurta, Tyson, & Majewski 1990) but generally lacked sufficient sensitivity to rule out a significant population of Lyman-limit systems. With the advent of thinned, UV-sensitive wide format CCD cameras, it has become feasible to survey a large part of the sky in search of such Lyman-limit systems. Furthermore, with the advent of 8-m class telescopes it has become possible to provide spectroscopic confirmation for these high-redshift objects.

In this Chapter we will use a simplified version of the photometric redshift technique to assign redshifts to a subsample of galaxies in the WHDF. A fully-fledged photometric redshift method, involving fitting template spectra of many ($\sim 10^6$) synthetic galaxy spectral energy distributions (SEDs) — as recently carried out in ground-based data by Giallongo et al. (1998) — is beyond the scope of this present work. Instead, we will examine the distribution of galaxies in the $(U-B)-(B-I)$ and $(B-R)-(R-I)$ planes, as illustrated in Figure 5.3 and Figure 5.4. Objects which are at high redshift will be red in $(U-B)$ (as the Lyman-break is redshifted into the U-band) but have $(B-R)$-$(R-I)$ colours ~ 0 (as their spectra are relatively flat in this region).

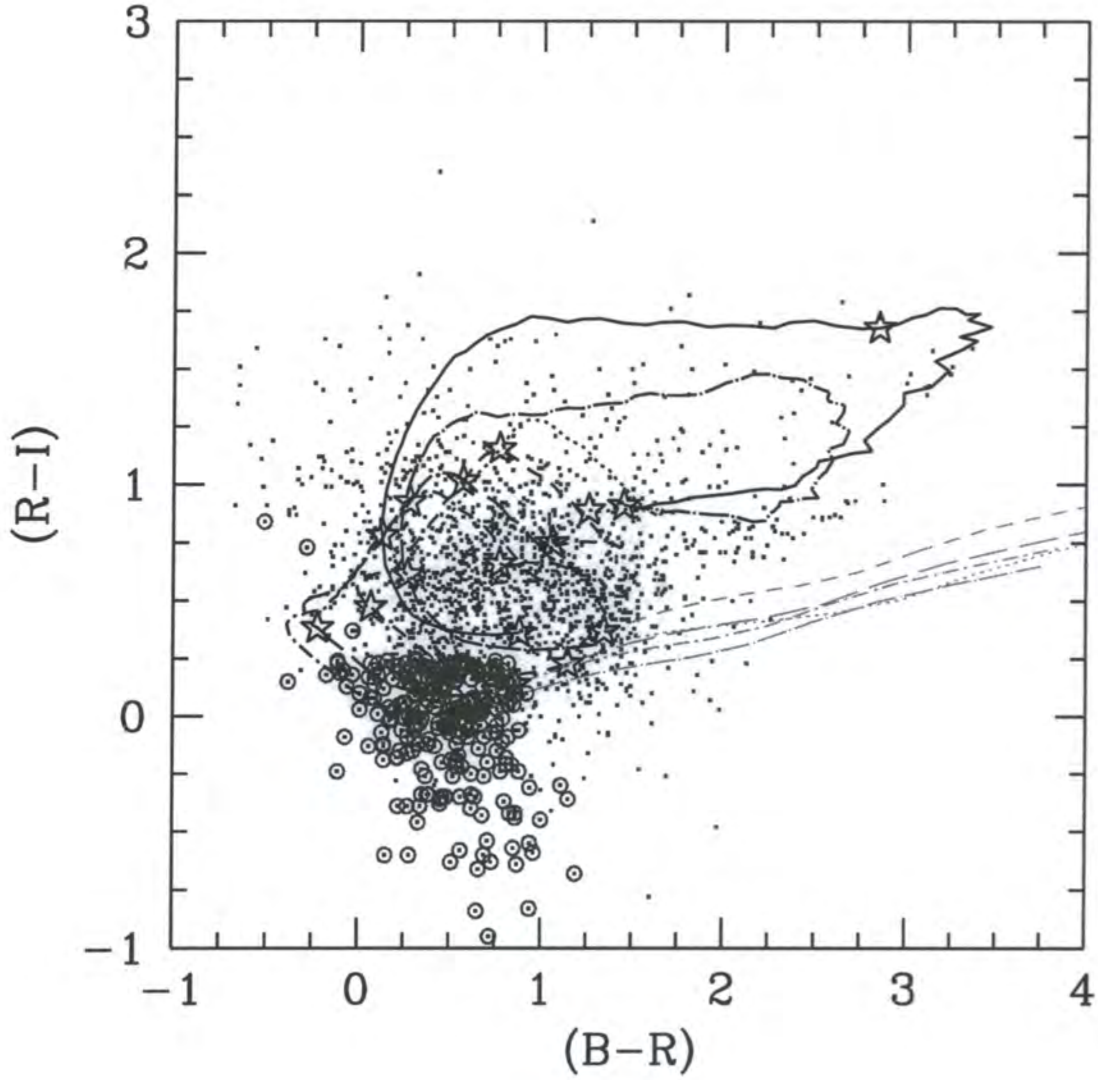

Figure 5.3: $(B - R)$ against $(R - I)$ for all galaxies in the WHDF. The circled objects have been selected to lie at $z > 2$. The solid and dotted lines show the paths of model E/S0 and Sab galaxies with the star-formation histories, internal extinction and Lyman-alpha reddening added as outlined in Chapter 2; dashed lines show the spiral tracks. Redshift intervals of $z = 0, 1, 2$ and 3 are marked with stars. Tracks with $z > 3$ are marked in light gray.

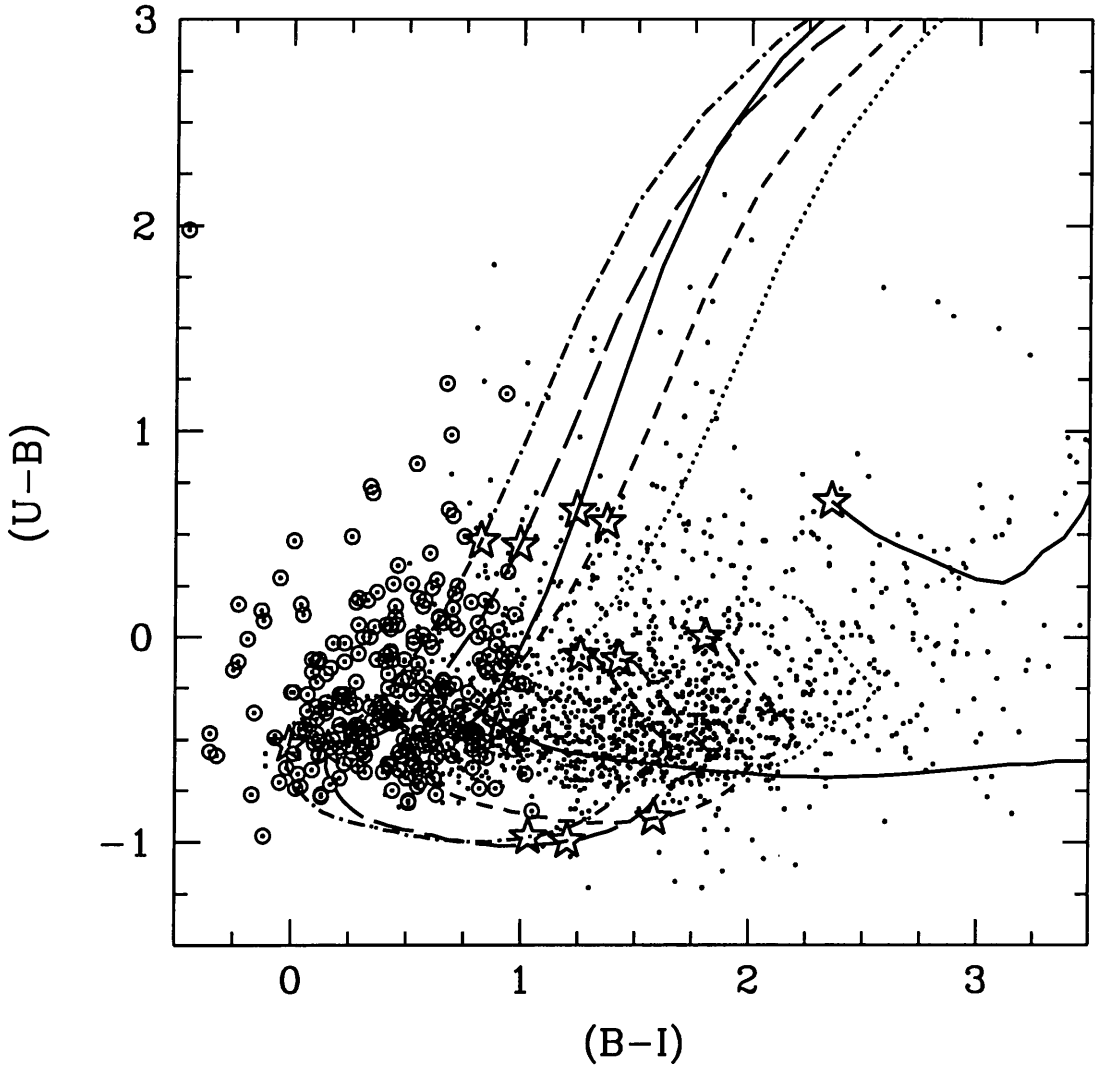

Figure 5.4: $(U-B)$ against $(B-I)$ for all galaxies in the WHDF. Tracks and symbols are identical to Figure 5.3.

These plots show *all* galaxies which have measured colours in the *UBRI* bandpasses. We also show model tracks to which Lyman-alpha reddening and (for the spiral types) internal extinction has been added. Both these effects cause the model tracks to turn sharply redwards at $z > 2$. High-redshift galaxies have been circled; these objects are selected to have $(B-I) < 1$ *and* $(U-B) > -0.4$, as well as $(B-R)$ and $(R-I) \sim 0$; this is essentially the region whose lower bound is defined by the location of the $z = 2$ symbols on each of the tracks. (Note that this selection process was carried out in an interactive manner by displaying the three-dimensional distribution of galaxies in the colour-colour-colour plane). There are 260 galaxies which lie in this region. In Note that in Figure 5.4 there are several objects at $z > 3$ but which are not circled; this is because they have large $(B-R)$ and $(R-I)$ colours. In the following Section we will measure the clustering amplitude of this subset of galaxies.

5.3 Results

5.3.1 Measured correlations

In Figures 5.5, 5.6, 5.7 and 5.8 we plot our measured correlation amplitudes A_ω extrapolated to one degree (filled circles) as a function of sample limiting magnitude. Error bars plotted on the fitted values are a combination of the error in the fit and the bootstrap errors at each individual angular bin. For each bandpass, and at each magnitude limit, our measured correlations were fitted to equation 5.2. The value of C, the integral constraint, was determined separately for each bandpass as the area covered in each filter is not exactly the same. In each bandpass we also plot all available measurements from the literature. We also plot preliminary correlation amplitudes that we have determined from the Hubble Deep Field North (Williams et al. 1996); the object catalogues determined from these catalogues were prepared using the same methods used for our WHDF data. Correlations were measured on each of the three chips of the Wide Field Camera and averaged. For the HDF data, the power-law fit was only conducted for pairs at greater than $1''$ separation. These measurements should be regarded as an *upper limit* on clustering amplitudes as the pair count and angular extent of the HDF is very small and the consequent integral constraint correction very large.

$B-$band correlations

We first consider our measured clustering amplitudes in the $B-$band. In this bandpass our sample reaches extremely high galaxy surface density—approaching $\sim 10^6$ gal deg^{-2} at $B = 28^m$, and furthermore it probes to the highest redshift; our low-q_0 models indicate that by $B \sim 28$ we reaching $z_{med} \sim 2$. Furthermore, our measurements of the $B-$band correlation function are significantly deeper than any previously published work. Our brightest bin, at $B < 27.0$, is in agreement with the correlation amplitude measured by Metcalfe et al. (1995) from a 26 hr exposure frame taken with the Isaac Newton Telescope (INT). This image overlaps the Herschel Deep Field, providing a useful check upon the reliability of the independently-written code used to analyse the current dataset. Faintwards of $B = 27$, our correlation amplitudes remain flat, a point which we discuss in detail in Section 5.4.4. The errors on our fitted correlations in B are relatively low in comparison with our other bandpasses because at $B < 28$ we detect ~ 6000 galaxies, more than in any other bandpass. Our HDF-N clustering measurement is in agreement with the measurement from the much larger area of the WHDF.

Also plotted on Figure 5.5 are the predictions for the clustering of our non-evolving models for three values of ϵ and for a low q_0 cosmology. To allow comparison with the previous work of Metcalfe et al. and Roche et al. we take the correlation length $r_0 = 4.3h^{-1}$ Mpc and (as throughout this chapter) we

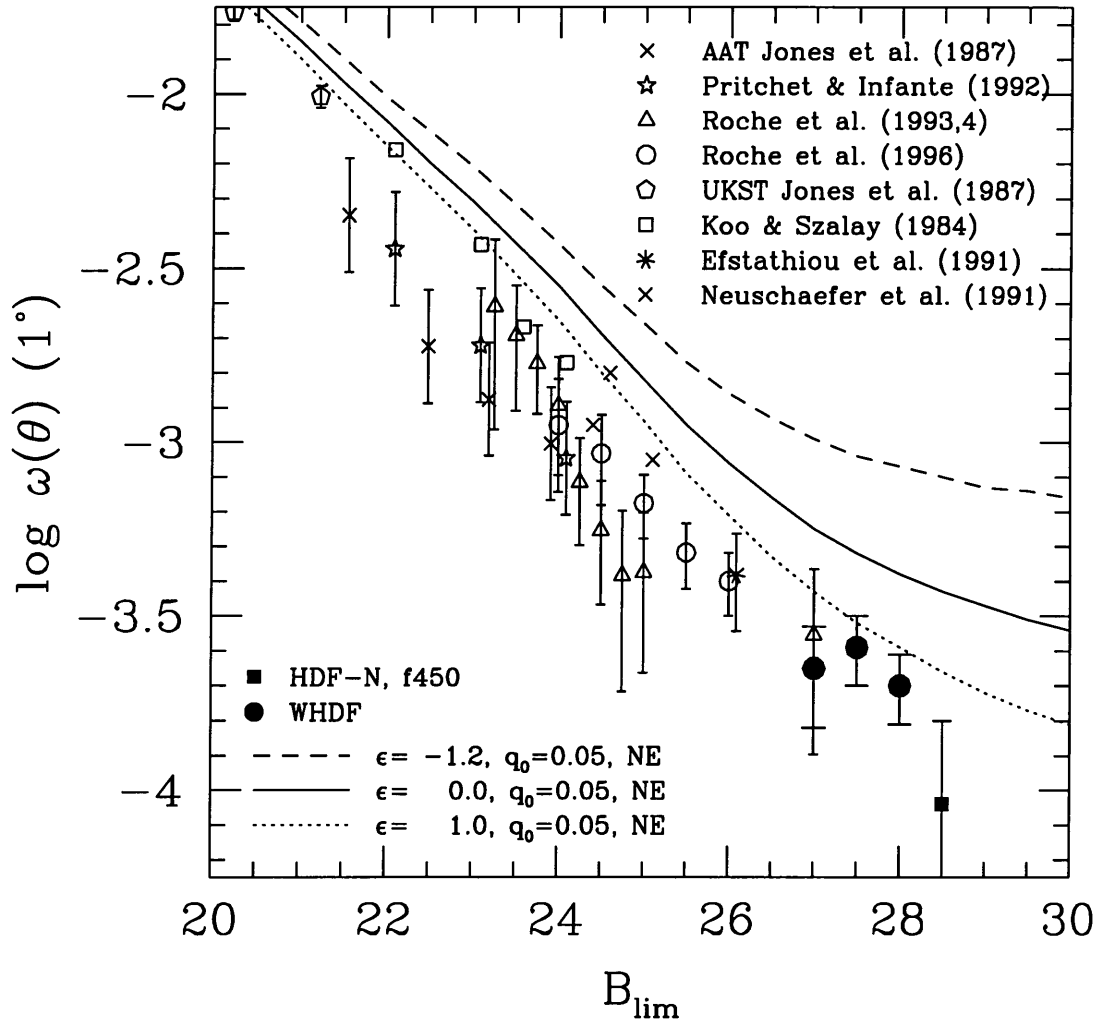

Figure 5.5: The fitted amplitude of the galaxy-galaxy angular correlation function $\omega(\theta)$ at 1° plotted against sample limiting B magnitude for our current work (filled circles). The filled square shows a correlation amplitude measurement from the HDF-N. Also shown is a compilation from the literature (open symbols), and the predictions of three $q_0 = 0.05$ non-evolving models for three different values of the clustering growth parameter ϵ: $\epsilon = 0$ (solid line); $\epsilon = 1.0$ (dotted line) and $\epsilon = -1.2$ (dashed line).

fix $\gamma = -1.8$. This value of r_0 was chosen to produce the correct clustering amplitude at brighter magnitudes as measured from early Schmidt plate surveys (Jones, Shanks, & R. 1987; Stevenson et al. 1985). We adopt the same value of r_0 for all bandpasses; in Section 5.4.2 we discuss if this is appropriate given our data. One consequence of the adopted value is that in some bandpasses the predictions of the non-evolving models appear to be *below* the data *for all magnitude limits* which we plot; this certainly appears to be be the case for the $B-$band; however, the models in fact do pass through the data at brighter magnitudes not shown on the graph.

Our non-evolving models have some important differences with those used in the earlier works of Roche et al. and Metcalfe et al.. Firstly, our non-evolving models include the effects of internal extinction by dust (corresponding to $A_B = 0.3$ mag, using the dust model of Pei (1992)) and reddening by the Lyman alpha forest (as modelled in (Madau 1995)). Both of these effects may become significant at the very faintest magnitudes we reach, where $z_{med} \gtrsim 2$. Secondly, our $k-$ corrections are computed from the models of Bruzual & Charlot (1993) for both our evolving and non-evolving models, whereas these previous works used polynomial fits to the spectral energy distributions of Pence (1976) for their non-evolving models. These fits only extend to $z \sim 2$ and are held constant at higher redshifts. Thirdly, the redshift distributions in these earlier papers were artificially truncated at $z = 3$. The sum effect of these differences is that in Roche et al. and Metcalfe et al. the slope of the A_ω – magnitude limit scaling relation remains constant whilst ours begins to level out at $B \sim 26$.

$R-$band correlations

Our $R-$band correlations plotted in Figure 5.6 also reach faint magnitude limits ($R < 26$), although the number of galaxies in this catalogue is much smaller

(~ 300) than in our $B-$ survey and consequently our error-bars are much larger. Our measured clustering amplitude at $R < 25.5$ agrees well with the faintest data point of Brainerd, Smail, & Mould (1994); unfortunately, our survey area is too small to permit us to check our clustering amplitudes with values from the literature measured at brighter magnitudes; for example, the large, ~ 2 deg^2 CCD survey of Roche & Eales (1998) is limited at $R < 23.5$.

Our measured clustering amplitudes in $R-$ are *much lower* than the predictions of the non-evolving, stable clustering model. However, they are in good agreement with the HDF clustering measurements of Villumsen, Freudling, & Da Costa (1997); our own clustering measurements in the HDF also agree with these points.

$I-$band correlations

In the $I-$band the practice in the literature has been to quote correlation amplitudes as a function of sample *median* magnitudes and not limiting magnitudes; to allow us to compare our current work with the published values we plot our clustering amplitudes at the median magnitudes of our samples. Similarly, our model correlation amplitudes are plotted at the median magnitude of each magnitude limited slice. This is shown in Figure 5.7. The model predictions for the median magnitudes of each data slice are in good agreement with our observations.

In addition to our deep $I < 26$ data, we have an additional image taken at the INT which overlaps the WHDF. This covers a total of ~ 80 arcmin^2 to $I < 23.5$ and allows us to determine A_ω from $I_{med} = 20$ to $I_{med} = 22$. These correlation amplitudes measured at brighter magnitudes agree well with the literature, and the faintest bin in this data set agrees with our measurements from the brightest bin of the WHDF dataset. However, faintwards of $I \sim 22$ a discrepancy emerges between our measurements and those from the literature, although

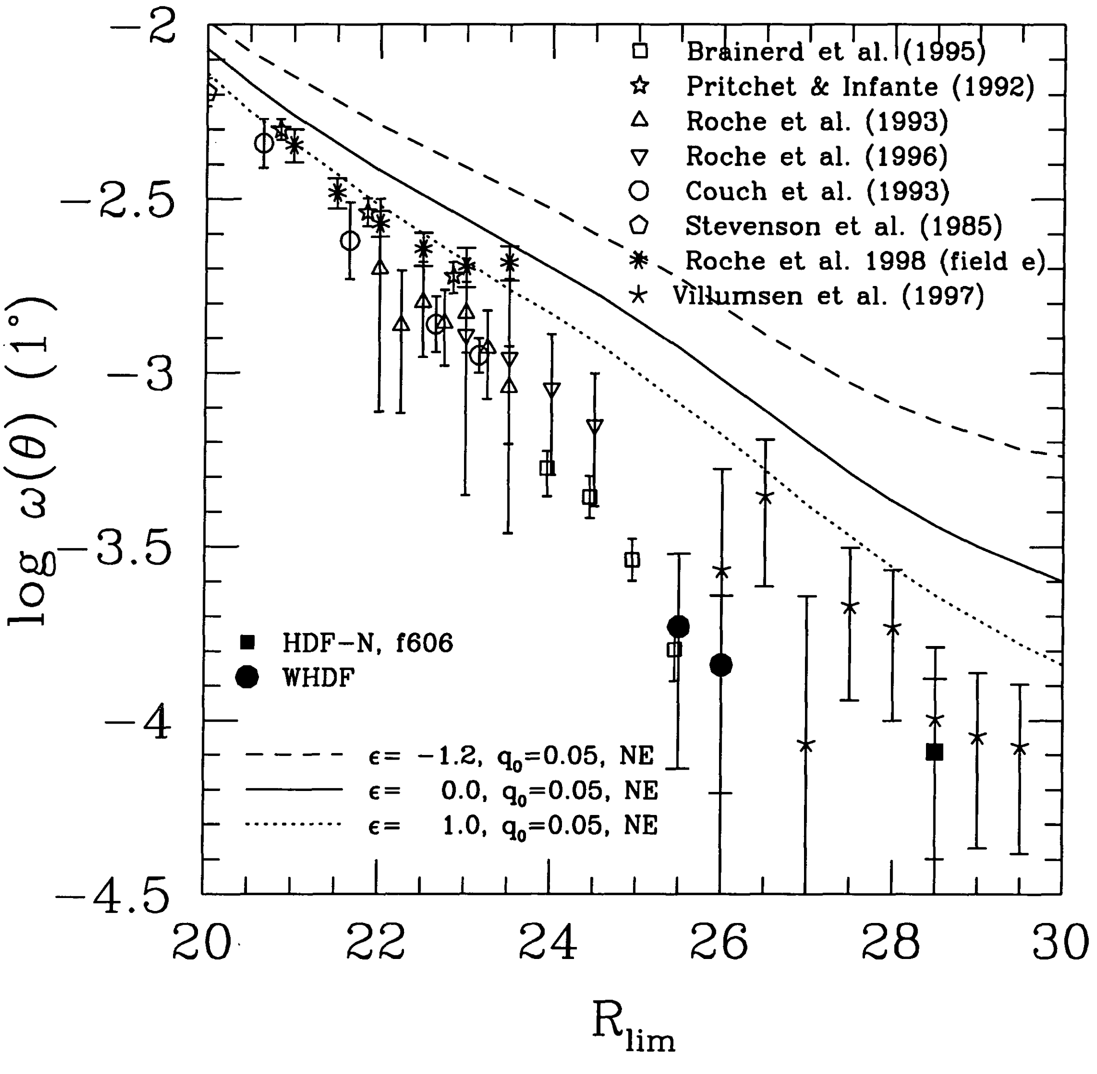

Figure 5.6: The fitted amplitude of the galaxy-galaxy angular correlation function $\omega(\theta)$ at 1° plotted against sample limiting $R-$ magnitude for our current work (filled circles and squares). Also shown is a compilation from the literature (open symbols), and the predictions of three $q_0 = 0.05$ non-evolving models for three different values of the clustering growth parameter ϵ: $\epsilon = 0$ (dotted line); $\epsilon = 1.0$ (dashed line) and $\epsilon = -1.2$ (solid line).

our amplitude measurement at $I_{med} \sim 26$ from the HDF-N is consistent with our observations. In our faintest bin, $I_{med} \sim 24$, our clustering measurements are ~ 5 times lower than the measurements made by Brainerd & Smail (1998) over two slightly smaller fields of area $\sim$ 30arcmin^2 at a similar depth. At brighter magnitudes, our points are also below the faintest bins of Postman et al. (1998). This work is a large-area CCD survey covering a contiguous 16 deg^2 area and is currently the most reliable determination of galaxy clustering over wide angles and at intermediate ($z \sim 1$) depths. In Section 5.3.2 we attempt to quantify if the discrepancies between our survey and other works could be explained in terms of cosmic variance effects.

$K-$band correlations

Until very recently measuring $\omega(\theta)$ at near-infrared wavelengths was time-consuming and difficult as the field of view of typical detectors covered only ~ 1 arcmin^2. However, wide-format IR arrays are becoming available making it now possible to conduct wide, deep surveys of the near-infrared sky.

In Figure 5.8 clustering amplitudes as determined from our faint, $H < 22.5$, wide area ($\sim$ 50 arcmin^2) Calar Alto Survey are shown (filled circles); the photometric properties of this sample were discussed in Chapter 4. Similarly, also plotted are clustering measurements from our 6×6 UKIRT IRCAM3 mosaic, discussed in Chapter 2 (filled squares).

In plotting the $H-$ limited Calar Alto points on our $K-$ limited scaling relation we make two assumptions: Firstly, at $K \sim 22$, $(H - K) \sim 0.3$; and secondly, for a given surface density, the clustering properties of $H-$ selected and $K-$ selected galaxies is identical. The first assumption seems reasonable, given that at $K \sim 20$, galaxies in our survey have $(H-K) \sim 0.3$ and it is unlikely that they become significantly bluer by $K \sim 22$. The $K-$ selected $(I-K)$ histograms

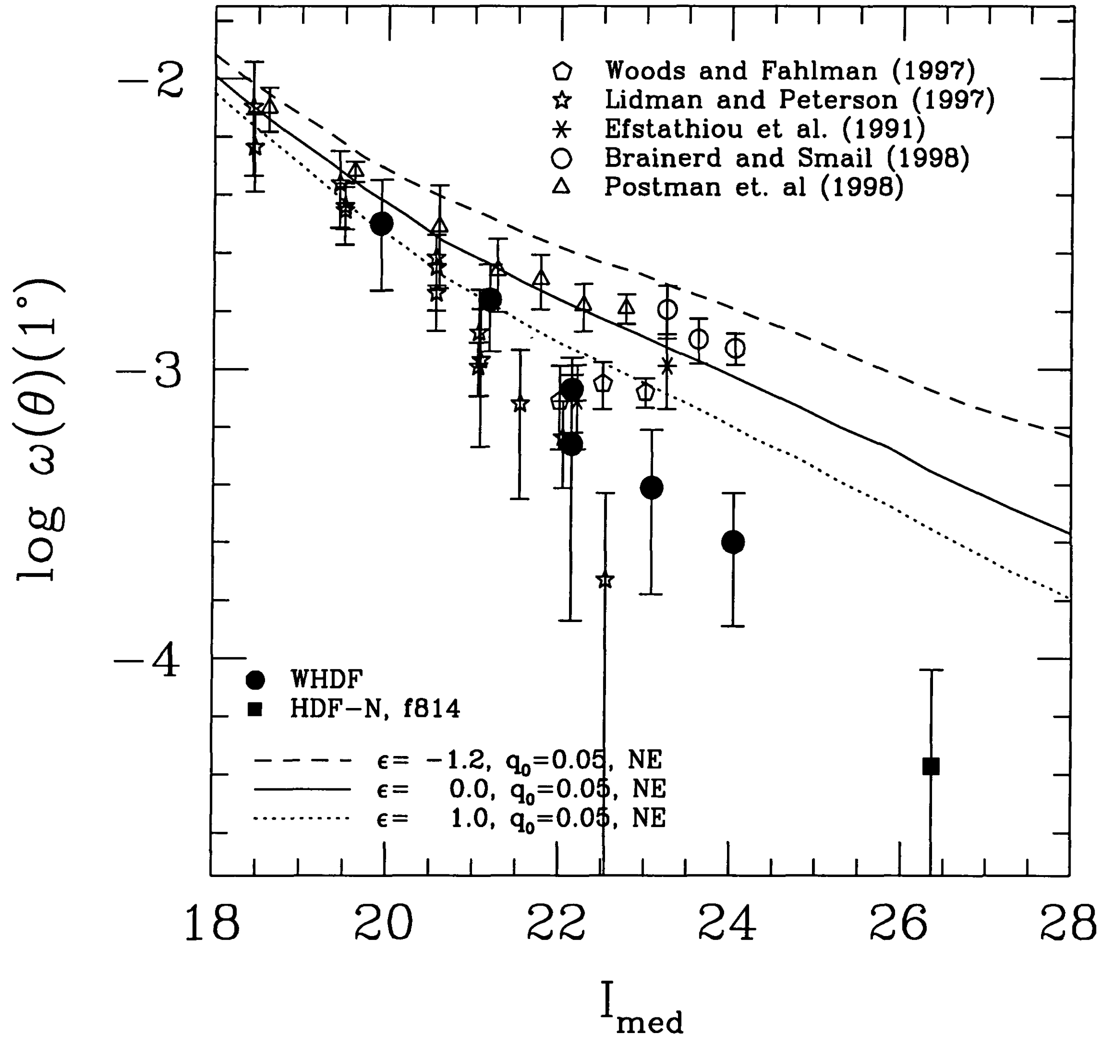

Figure 5.7: The fitted amplitude of the galaxy-galaxy angular correlation function $\omega(\theta)$ at 1° plotted against sample median $I-$ magnitude for our current work (filled circles and squares). The filled circles shown at brighter magnitudes are from a brighter survey carried out at the Isaac Newton Telescope which overlaps the WHDF. Also shown is a compilation from the literature (open symbols), and the predictions of three $q_0 = 0.05$ non-evolving models for three different values of the clustering growth parameter ϵ: $\epsilon = 0$ (dotted line); $\epsilon = 1.0$ (dashed line) and $\epsilon = -1.2$ (solid line).

shown previously in Figure 2.12 support this. Also given that our Calar Alto $H < 20$ A_ω agrees well with our UKIRT $K < 19.5$ point, we conclude that our second assumption is also valid.

Our points at $K = 19 - 20$ agree well with the survey of Roche, Eales, & Hippelein (1998) and Roche et al. (1998); however at fainter magnitudes there appears to be a large discrepancy between our amplitudes and the measurement of Carlberg et al. (1997). Once again, we defer a detailed discussion of the possible explanation of these discrepancies until Section 5.3.2.

High-redshift clustering?

Figure 5.9 shows our measured correlation amplitudes from the catalogue of objects which were selected to lie at $z > 2$. The upper panel shows $\omega(\theta)$ determined from *all* galaxies in the sample, whereas the lower panel shows a sample limited at $B < 25.5$, the completeness of the combined $UBRI$ catalogue. The dotted line shows $\omega(\theta) = 0$, i.e., what would be expected from an unclustered population, whereas the solid line shows the clustering amplitude expected for a magnitude $B < 25.5$ limited sample, according to our best-fitting evolutionary model and assuming $\epsilon = 0$. The dotted line indicates $\omega(\theta) = 0$.

In the top panel we detect an upper limit on the clustering signal: $\log(A_\omega) = -3.1^{+0.33}_{-\infty}$. This is consistent with the predictions of our $q_0 = 0.05$, $\epsilon = 0$ evolutionary model, which gives $\log(A_\omega) = -3.36$ for a B- limited catalogue with the same median magnitude B-magnitude as the matched $UBRI$ catalogue. However, for the catalogue cut at the approximate incompleteness limit of the combined $UBRI$ catalogue, we are not able to place even an upper limit on the clustering amplitude. Given the small size of our sample, we regard these results as inconclusive. without spectroscopic redshifts for a sample of galaxies we are unable to test the reliability of this technique; our sample may be contaminated with lower-redshift

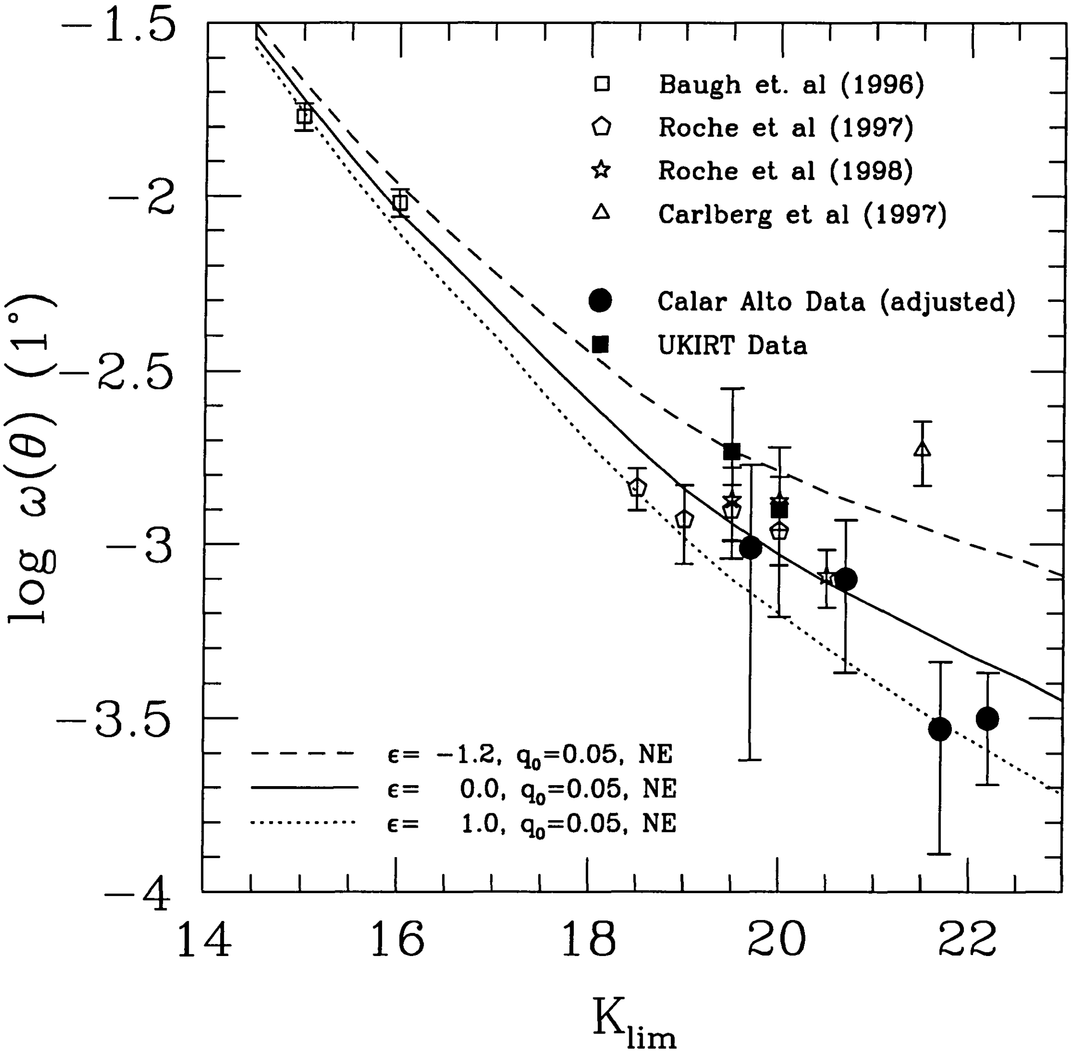

Figure 5.8: The fitted amplitude of the galaxy-galaxy angular correlation function $\omega(\theta)$ at 1° plotted against $K-$band limiting magnitude for a compilation from the literature and for our current work (filled circles,filled squares)

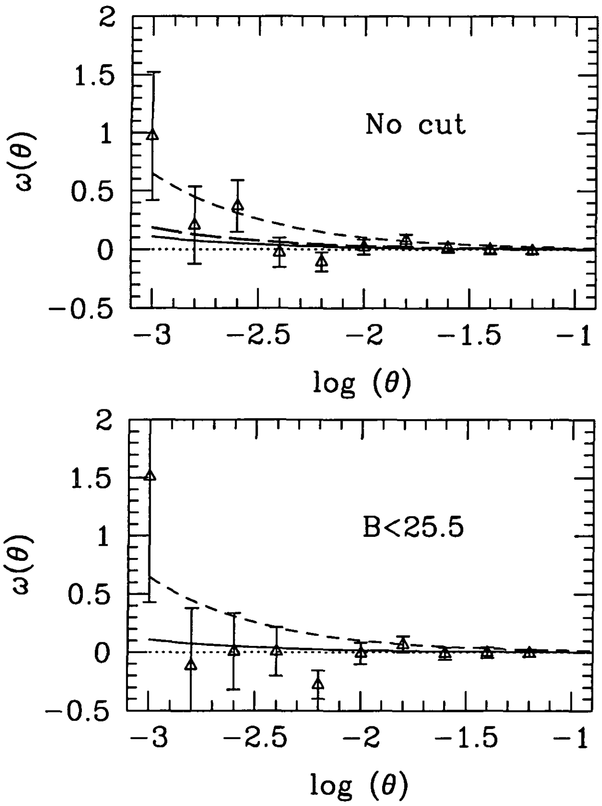

Figure 5.9: $\omega(\theta)$ measured for two high-redshift samples. The sample in the upper panel consists of all circled objects in Figures 5.3 and 5.4; in the lower panel the is cut at the approximate $B-$band incompleteness limit of the *UBRI* catalogue. The solid line show the prediction for a $B < 25$ limited catalogue calculated assuming $\epsilon = 0$. The heavy dashed line in the upper panel shows a fit to this data and corresponds to and upper limit of $\log(A_\omega) = -3.1^{+0.33}_{-\infty}$. The dashed line shows the predictions from a model in which all galaxies are at $z > 2$ and have $\epsilon = -1.2$). The dotted line indicates $\omega(\theta) = 0$.

galaxies.

We could try relaxing the selection criterion outlined in Section 5.2.4 in order to increase the numbers of galaxies in our sample; however, the topology of colour-redshift space is complicated and widening our selection area in these simplified color-redshift diagrams would lead to contaminating our catalogue with low-redshift objects. To successfully apply this technique would require imaging much more than our current ~ 50 arcmin^2. Alternatively, a complete implementation of a photometric redshift method and a calibration of this technique with spectroscopic redshifts would allow the direct measurement of $\xi(r, z)$; we defer such an undertaking for future work.

5.3.2 Quantifying errors in the correlation function

In this Section we will investigate if we have estimated the magnitude of our correlation function error bars correctly. The small size of our field means our integral constraint (equation 5.2) corrections are large, and consequently accurate measurements of $\omega(\theta)$ are dependent on an accurate determination of this quantity. Our main motivation is to see if we can explain the discrepancies between our measurements of A_ω at $I < 25$ and $K \sim 21.5$ with those of Brainerd & Smail (1998) and Carlberg et al. (1997). There are already indications that such "extra" variance could be significant at the depths of our survey. Postman et al. (1998) directly address this question at shallower depths in their work which covers ~ 15 deg^2. By extracting 250 independent $16' \times 16'$ fields from their survey (each of which is five times larger than the WHDF but at a brighter limiting magnitude) they find that the variance on $\omega(1')$ is comparable to its mean value of ~ 0.045, with extreme values reaching $\times 3$ this. Furthermore, they suggest that as the error distribution for A_ω is non-Gaussian, and skewed positively, there could be many more areas in which A_ω is below the mean value, rather than above it.

Quantifying the amount of "extra" variance which could affect clustering measurements in a very deep field like the WHDF — without going back to the telescope to gather more data — is not a straightforward affair. The box size of even the largest N-body simulations currently available is too small to simulate the depths to which our survey reaches. In this Section we will adopt a simpler approach and use the model of Soneira & Peebles (1978) to generate large mock catalogues, to measure the correlation function for each of these, and to use the variance of these measurements as an estimate for our error.

Our method starts with the generation of a catalogue covering 6.25 deg^2 with the same surface density of objects as in our real catalogue at $I < 25$; over this area this corresponds to $\sim 7.5 \times 10^5$ galaxies. Next, we measure $\omega(\theta)$ over the full simulated catalogue area using a modification of our standard correlation function program employing a linked list technique to reduce processing time (we have verified that this method gives the same results as the standard direct pair-counting technique; it is, however, much faster). Our aim is to produce a catalogue for which the fitted correlation amplitude $\log(A_\omega)$ at $I < 25$ is midway between the result of Brainerd & Smail ($\log(A_\omega) = -2.93^{+0.05}_{-0.06}$) and our own ($\log(A_\omega) = -3.61^{+0.16}_{-0.26}$). Once a catalogue with the desired correlation amplitude is produced (it is not possible, with the method of Soneira & Peebles (1978) to specify an A_ω at the outset; rather a process of trial-and-error must be conducted) it is randomly sub-sampled to produce 200 sub-areas each of which has the same field of view ($\sim$ 50 arcmin^2) and galaxy surface density at $I \sim 25$ as the WHDF (this translates to $\sim$ 2000 objects per field). On each of these sub-fields correlation amplitudes are measured using the same parameters as for the real data set, and a histogram is computed using each of these individual measurements of the simulated data.

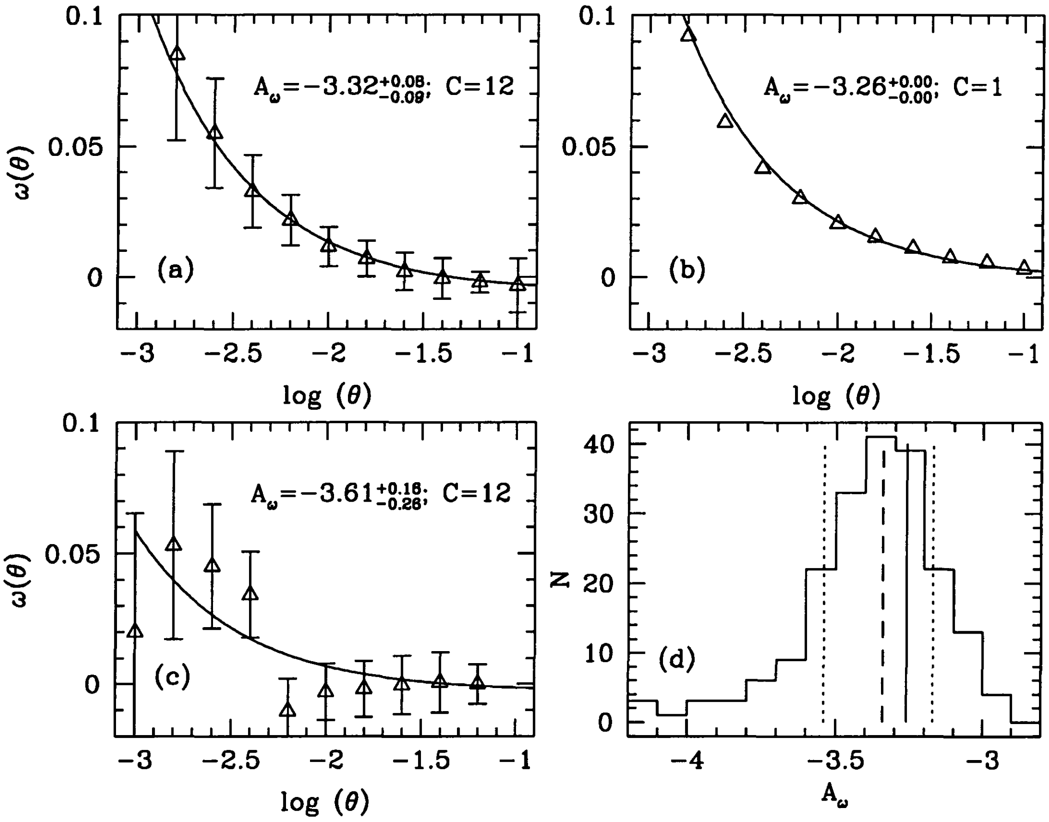

Figure 5.10: Results from simulations of a 6.25 deg^2 area with the same surface density of objects as our $I < 25$ catalogue. Panel (a) shows $\omega(\theta)$ measured from an average of two hundred sub-areas each covering 50 arcmin^2 (corresponding to the size of the WHDF); panel (b) shows $\omega(\theta)$ determined from the full simulation. Panels (c) and (d) show $\omega(\theta)$ as measured at $I < 25$ from the WHDF and the histogram of fitted values for $\log(A_\omega)$ from the simulations. The dotted lines shown on the histogram represent $\pm 1\sigma$ deviations from the median value; the full simulation value is shown as the solid line and the average value as the dashed line. From this histogram we determine $\log(A_\omega) = -3.35^{+0.18}_{-0.17}$.

Figure 5.10 presents results from one set of simulations. Panel (b) in this Figure shows the measured correlation function for a synthetic catalogue generated using the method outlined above (error bars have not been plotted as they are smaller than the symbols for all bins). For this catalogue we find $\log(A_\omega) = -3.26$ for an integral constraint $C = 1$. Panel (a) shows the average value of $\omega(\theta)$ from two hundred sub-samples of this catalogue, as well as the fitted value to this average which we find to be $\log(A_\omega) = -3.32^{+0.08}_{-0.09}$. For comparison, the fit to our $I < 25$ observations is shown in panel (c); for the real data we find $\log(A_\omega) = -3.61^{+0.16}_{-0.26}$.

This procedure tests several important aspects of our technique. Because our simulated field is so large, the integral constraint correction (Equation 5.2) which must be applied to it is much smaller than the amount required for each of the individual sub-fields. Given that the A_ω which we measure from the full survey agrees to within the fitting errors to the A_ω determined from the average of two-hundred sub-fields we conclude that errors arising from an incorrect determination of the integral constraint are not significant. However, the agreement between the sub-fields and full-survey values is perhaps not surprising as both the catalogue and C were generated and calculated assuming a power-law slope δ for $\omega(\theta)$ of -0.8. There is some indication that δ becomes flatter at fainter magnitudes (Postman et al. 1998) although we are unable to test this with our current data set. A flatter correlation function at fainter magnitudes would lead to an underestimate of the integral constraint and a consequent *underestimate* of A_ω.

More significantly for this current work, however, is the large dispersion we find for the fitted A_ω's from our simulated fields. Panel (d) of Figure 5.10 illustrates this. From this diagram, $\log(A_\omega) = -3.35^{+0.18}_{-0.17}$ (1σ errors). This corresponds to a linear error of $\pm 2.2 \times 10^{-4}$. By comparison, our errors determined from our bootstrap resamplings are $\pm 1.1 \times 10^{-4}$; Brainerd & Smail's errors are $\pm 1.5 \times 10^{-4}$. Their points are an average of two widely separated ~ 30 arcmin^2 fields and at $I < 25$ contain approximately the same numbers of galaxies as our catalogue. On the basis of these simulations we conclude both our errors and those of Brainerd & Smail underestimate the true error. Additional simulations at higher amplitudes also have higher variances; a second simulation at $\log(A_\omega) = 3.1$ has a 1σ error of $\pm 2.6 \pm 10^{-4}$. Adopting errors of this size, we find that our correlation measurement is consistent with that of Brainerd & Smail at the 2.5σ level. Finally, we also note that the scatter found by Postman et al. (1998) from 250 independent CCD fields at $21 \leq I \leq 22$ is *much* larger than any of these values — 17×10^{-4}. This may indicate that our errors determined from our simulations are in fact *lower* limits.

Turning to the K- selected correlation amplitudes plotted in Figure 5.8 we note that at $K < 21.5$ over ~ 27 arcmin^2 Carlberg et al. (1997) measure $\log(A_\omega) = -2.72^{+0.08}_{-0.10}$. This is also different from our work: at $K < 21.7$ we measure $\log(A_\omega) = -3.53^{+0.19}_{-0.36}$ in an area of ~ 44 arcmin^2. The number density of galaxies at $K \sim 21$ is approximately the same as at $I \sim 25$, and the amplitude of Carlberg et al.'s point is also within $\sim 40\%$ of Brainerd & Smail's anomalous point. Moreover, as we have described above, we find a larger variance on $\omega(\theta)$ for simulations of higher amplitude. These considerations leads us to conclude that the stated error bar on Carlberg et al.'s measurement is also an underestimate of the true error. Furthermore, we conclude that our "low" results at $I \sim 25$ and $K \sim 21$ are *not* inconsistent with the other results in the literature, given the large error bars afflicting measurements of A_ω in fields of this size and at these depths.

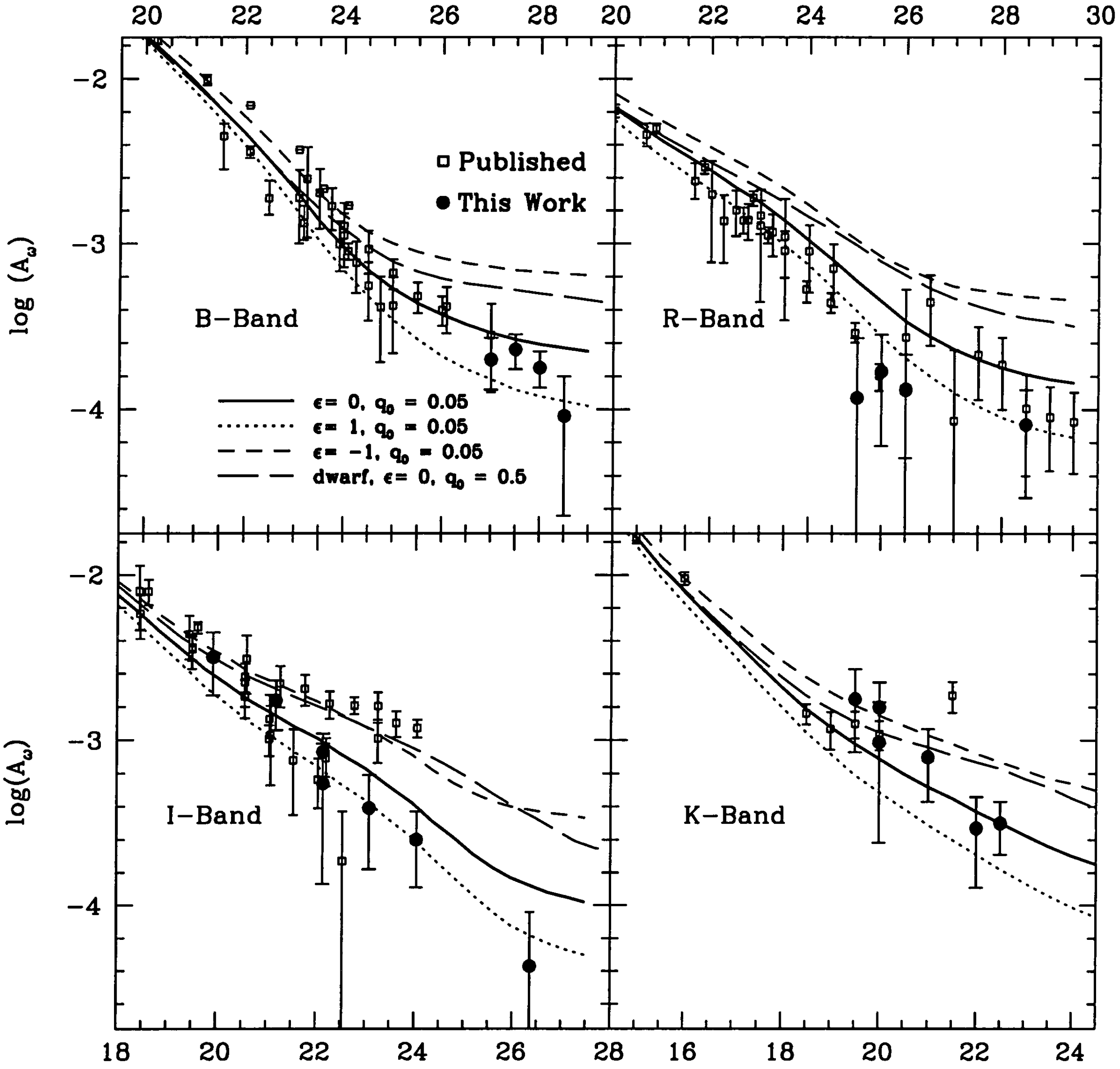

Figure 5.11: The amplitude of the angular correlation function $\omega(\theta)$ at one degree (A_ω) in the WHDF and HDF (filled symbols) shown as a function of apparent magnitude for *BRIK* selected samples (for *I*, correlations are plotted as a function of sample median magnitude); open symbols show points from the literature. Also shown are the predictions of our best-fitting evolutionary model (previous figures have shown the non-evolving models) for three values of the clustering growth parameter ϵ and for $r_0 = 4.3h^{-1}$ Mpc and $q_0 = 0.05$. The long dashed line shows the predictions of the $\epsilon = 0$, $q_0 = 0.5$ dwarf-dominated model described in Chapter 4.

5.4 Interpretation and discussion

5.4.1 Predicting $\omega(\theta)$ from the evolutionary models

In Figure 5.11 we plot the results from all bandpasses (filled symbols) in comparison with the literature (open symbols), as well as the predictions of the evolutionary models, once again with the three values of ϵ we have examined before. In comparing these four graphs, it is interesting to notice how the *shape* of the scaling relation is qualitatively different from bandpass to bandpass. To understand the origin of these differences, we start by emphasizing that the *amplitude* of the correlation function is inversely proportional to the sample median redshift; our scaling relation graphs are a direct probe of the median redshift of the model population (this may be true in the real universe too, providing the correlation function slope does not change too much with redshift; in what follows we make this assumption).

Starting with the $B-$band scaling relation, we note that in this bandpass in all magnitude slices, the model population is dominated by spiral galaxies. Brighter than $B \sim 22$, evolutionary effects are negligible; however, faintwards of this, galaxies undergo $1-2$ magnitudes of brightening, and a significant high-redshift tail becomes evident. For this reason the slope of the B-band number counts is steepest in this range. The effect of this evolutionary brightening is to cause the median redshift of the $B-$ selected redshift distributions to increase rapidly faintwards of $B \sim 24$; at $B \sim 22$, $z_{med} \sim 0.3$, but by $B \sim 24$, $z_{med} \sim 0.7$ and by $B \sim 25$, $z_{med} \sim 1$. This causes A_ω to drop rapidly below the non-evolving prediction. This extended B-band redshift distribution, confirmed in the spectroscopic survey of Cowie, Songaila, & Hu (1996), allows us to explain the observed clustering amplitudes without recourse to positing a hypothetical, weakly clustered population dominating the B- selected samples, as did some earlier authors

(Infante & Pritchet 1995; Brainerd, Smail, & Mould 1994). In redder bandpasses, the situation is slightly different; for example, in R spiral evolution is more gradual than in B-, causing a much less pronounced slope change in the A_ω-magnitude relation at $R \sim 24$. Similar considerations apply to the I-band. By the K-band, however, the form of the A_ω limiting magnitude relation is determined primarily by the elliptical population; although the elliptical counts turn over at $K \sim 20$ they still comprise more than half of the total galaxy population faintwards of this. Consequently, the A_ω-limiting magnitude relation has constant slope as these galaxy samples are dominated by slowly-evolving elliptical populations.

In Chapter 2 and Chapter 4 we saw how the low median redshift found for $K-$ selected redshift distributions (Cowie, Songaila, & Hu 1996) placed stringent limits on the amount of evolution allowable in these bandpasses. In order for our PLE models to fit Cowie, Songaila, & Hu's $K < 19$ redshift distribution (which has a very low median redshift, close to the predictions of a non-evolving model), we had to assume a steep slope ($x = 3$) for the initial mass function. This reduces the amount of passive evolution at K- for ellipticals, resulting in a total galaxy population with a lower median redshift (Figure 2.6 illustrated how the variations in IMF slope could affect the redshift distributions).

As we will describe in the following Section, our $\epsilon = 0$, low q_0 evolutionary model (incorporating a steep IMF slope) fits the observed clustering amplitudes for $K-$ selected samples quite well. Therefore, the observed clustering amplitudes are consistent with the underlying redshift distribution for K- selected samples which has a low median redshift, close to the predictions of the non-evolving model. More significantly — and beyond the spectroscopic limit of the even the Keck telescope — our Calar Alto data at $H \sim 22$ indicates that even at these very faint magnitude levels, the H- selected galaxy correlations are *still* consistent with the non-evolving prediction. Galaxy merging, however, could provide another explanation for the low median redshift we infer for our K-sample. A low median redshift for K- selected surveys is a general prediction of the models of hierarchical galaxy formation (Kauffmann & Charlot 1998).

As we have discussed our K- selected samples are dominated by elliptical galaxies. Local redshift surveys have established that such galaxies have correlation lengths $\sim$ 3 times higher than spirals (Loveday et al. 1995), so it would seem that our value of $r_0 = 4.3h^{-1}$ Mpc is perhaps inappropriate when applied to a $K-$ selected sample. This possiblity will be discussed in detail in the following section.

Finally, we examine the predictions of our $q_0 = 0.5$, dwarf-dominated model, shown in Figure 5.11 as the long dashed line. In general, the median redshift of a magnitude-limited sample is lower for a low-q_0 cosmology than for a high q_0 one, because the differential volume element ia smaller in the latter case. Consequently, for the same value of ϵ and r_0, A_ω is higher for $q_0 = 0.5$ than it is for $q_0 = 0.05$. For this reason, our $\epsilon = 0$, $q_0 = 0.5$ dwarf model predicts higher clustering amplitudes at all magnitude limits in all bandpasses than our standard $\epsilon = 0$ $q_0 = 0.05$ model. The exact magnitude of the differences between the two models depends (in addition to the cosmological considerations outlined above) on where the median redshift of galaxies in the high-q_0 model is greater than unity, where the star-formation rate for the dwarf types is constant, or less than unity, and where they rapidly fade. This high clustering amplitude leads us to reject the dwarf-dominated, $\epsilon = 0$, $q_0 = 0.5$ model. Of course, this conclusion is dependent on the dwarf population having the same intrinsic clustering properties as the normal galaxy population, which may not be the case (Infante & Pritchet 1995; Brainerd, Smail, & Mould 1994).

5.4.2 The growth of clustering

In this Section we investigate what implications our measurements of A_ω as a function of sample limiting magnitude have for the growth of galaxy clustering. As we have commented earlier, the small angular size of the WHDF means we are probing very small scales where the growth of galaxy clustering is expected to be highly non-linear. Most of the power in our correlation function signal comes from our inner bins, at angular scales of $\sim 0.2'$; at $z \sim 1$, the typical median redshift of our samples, this translates to linear dimensions of $\sim 0.05h^{-1}$ Mpc (for $q_0 = 0.05$), a very small scale indeed. Additionally, how our samples are selected may affect clustering amplitudes. In our flux-limited catalogues, a range of galaxy luminosities will be present, and local redshift surveys have shown that clustering amplitude is a function of luminosity and morphology (Loveday et al. 1995; Tucker et al. 1997).

With these caveats in mind, in Table 5.1 we present the results for best-fitting values for the parameters r_0 and ϵ in Equation (5.4) determined by χ^2 minimization using our observations and the model ($\Lambda = 0$, $q_0 = 0.05$) outlined in Section 5.2.3. As before, we use redshift distributions determined from our best-fitting evolutionary model. Because of the strong co-variance between r_0 and ϵ it is not possible to derive both parameters simultaneously from our dataset; instead we investigate what values of r_0 and ϵ are implied by "reasonable" choices of these parameters.

Our primary concern is to investigate what value of ϵ best fits our data and to do this we will fix r_0 to $4.3h^{-1}$ Mpc. This value of r_0 (as we have explained in Section 5.3.1) is chosen to agree with angular correlation measurements determined from large Schmidt plate surveys. More recent work from local redshift surveys approximately agrees with this value. For example, Loveday et al. (1995) find for the b_J selected APM an r_0 of $5.1 \pm 0.2h^{-1}$ Mpc and

Bandpass	$r_0 = 4.3\ h^{-1}$ Mpc	$\epsilon = 0$
$B-$	$0.40^{+0.35}_{-0.30}$	$3.70^{+0.45}_{0.50}$
$R-$	$2.65^{+1.30}_{-0.65}$	$2.30^{+0.75}_{-1.05}$
$I-$	$1.10^{+0.75}_{-0.50}$	$3.35^{+0.45}_{-0.45}$
$K-$	$0.05^{+0.65}_{-0.45}$	$4.30^{+0.70}_{-0.80}$

Table 5.1: Best-fit values for ϵ for $r_0 = 4.3h^{-1}$ Mpc and for r_0 for $\epsilon = 0$, using redshift distributions computed from our best-fitting evolutionary model and assuming $q_0 = 0.05$. Errors quoted are $\pm 1\sigma$.

$\gamma = 1.71$. The $R-$ selected Las Campanas Redshift Survey (Tucker et al. 1997) finds $r_0 = 5.0 \pm 0.14h^{-1}$ Mpc.

In general, we find $\epsilon \sim 0$ for $r_0 = 4.3h^{-1}$ Mpc and $q_0 = 0.05$, from our own data alone. As we have already discussed at some length, in the I- band our points are different from those of Brainerd & Smail at the $\sim 3\sigma$ level. Their survey subtends $\sim 30'$ on the sky, and reaches similar depths to our own work, and so we would expect this survey to sample the same environments as our own, and therefore to show broadly similar growth of clustering. Combining Brainerd & Smail's three I- limited points with our own, we derive $\epsilon = 0.70^{+0.70}_{-0.45}$, again for $r_0 = 4.3h^{-1}$ Mpc.

This result is in agreement with the expectations from hierarchical models of galaxy formation, which find that at the $< 1h^{-1}$ Mpc scales we are sensitive to, clustering growth is relatively rapid (Figure 1. of Baugh et al. (1998a); (Benson et al. 1999)). In comparison, at larger scales ($\sim 5h^{-1}$ Mpc) the correlation function evolves much more slowly. At such separations, the clustering pattern is "frozen in" as the galaxies are tracing higher-mass haloes whose clustering evolution is close to $\epsilon = -1.2$.

How do our results compare with clustering measurements from the literature? With deeper pencil-beam spectroscopic surveys, it has become possible to directly measure r_0 at successively earlier epochs and to use this to infer a value for ϵ. Using a statistically complete subsample of 591 galaxies from the Canada-France Redshift Survey (Lilly et al. 1995a), LeFevre et al. (1996) were able to directly measure the evolution of r_0 in the interval $0 \leq z \leq 1$. They found $r_0(z = 0.53) = 1.5 \pm 0.09\ h^{-1}$ Mpc (for $q_0 = 0.05$), implying $0 < \epsilon < 2$. Carlberg et al. (1997), using a sample of 248 galaxies, found that for $M_K \leq -23.5$ galaxies, $r_0(z \sim 0.6) = 2.0^{+0.9}_{-0.2}\ h^{-1}$ Mpc. At higher redshift, Carlberg et al. derive $r_0(z \sim 0.97) = 1.4^{+0.9}_{-0.2}\ h^{-1}$ Mpc, which, combined with the lower redshift points from their survey, leads to $\epsilon \sim 0.2 \pm 0.5$.

The large size of the errors on our χ^2 fit does not permit us to make a detailed investigation of the dependence of ϵ with sample selection. However, it is interesting that we find the rate of clustering growth to be slowest for our K-selected survey, and that our results are broadly consistent with those from the K-selected sample of Carlberg et al. (1997). We expect our K- selected galaxies to be good tracers of the underlying matter. N- body simulations (Colin, Carlberg, & Couchman 1997) have shown that in a low-density universe, the clustering of matter is expected to evolve as $\epsilon \sim 0$.

The Canadian Network for Observational Cosmology (CNOC) have recently completed a large field galaxy survey in the range $0 \leq z \leq 0.7$ with a sample size of $\sim 10^4$ galaxies (Carlberg et al. 1998). For luminous objects with corrected R-band absolute magnitudes of $M_R^{k,e} < -20$ they find a slower clustering growth: $\epsilon = -0.6 \pm 0.4$, with $r_0 = 5.15 \pm 0.15$, strongly excluding clustering growth as rapid as $\epsilon \sim 1$.

5.4.3 Clustering of high redshift galaxies

Very recently it has become possible to isolate statistically significant numbers of galaxies at much higher redshifts using the Lyman-break technique outlined in Section 5.2.4, and to use these samples to investigate galaxy clustering in a much more well-defined sample than was possible in field galaxy studies. Steidel et al. (1998a) reported the discovery of strong clustering in redshift space in one of their survey fields; more recently, Giavalisco et al. (1998) observed 871 Lyman-break galaxies over five fields; 90% of their galaxies have redshifts of $2.6 \lesssim z \lesssim 3.4$. Giavalisco et al. (1998) derive a (co-moving) correlation length for the Lyman-break galaxies from their survey of $r_0 = 3.3^{+0.7}_{-0.6}\ h^{-1}$ Mpc, for $q_0 = 0.1$, which is very similar to the values of r_0 derived from the large local redshift surveys outlined above. This implies that the Lyman-break galaxies are more strongly clustered than any object discovered in any of the previous high redshift surveys like the CFRS, and therefore a different kind of object.

Interpreting the clustering properties of galaxies at high redshift in the context of CDM models was initially confined to elucidating their relationship to the clustering of dark matter haloes (Mo & Fukugita 1996). It soon became clear that the high clustering amplitudes observed in the Lyman-break systems required that they originated in regions of moderately high over-densities — that they were strongly biased, and consequently very massive. (In "biased" galaxy formation, galaxies only form in dark matter haloes which are above a certain threshold in mass. This helps to relate the abundance of dark matter haloes produced in the N-body simulations to the (much smaller) observed numbers of luminous galaxies). Subsequent work utilising semi-analytic techniques (Baugh et al. 1998b) and semi-analytic methods combined with very large, high-resolution N-body simulations (Governato et al. 1998) indicated that the Lyman-break objects are the progenitors of the central elliptical galaxies in massive clusters at the present day.

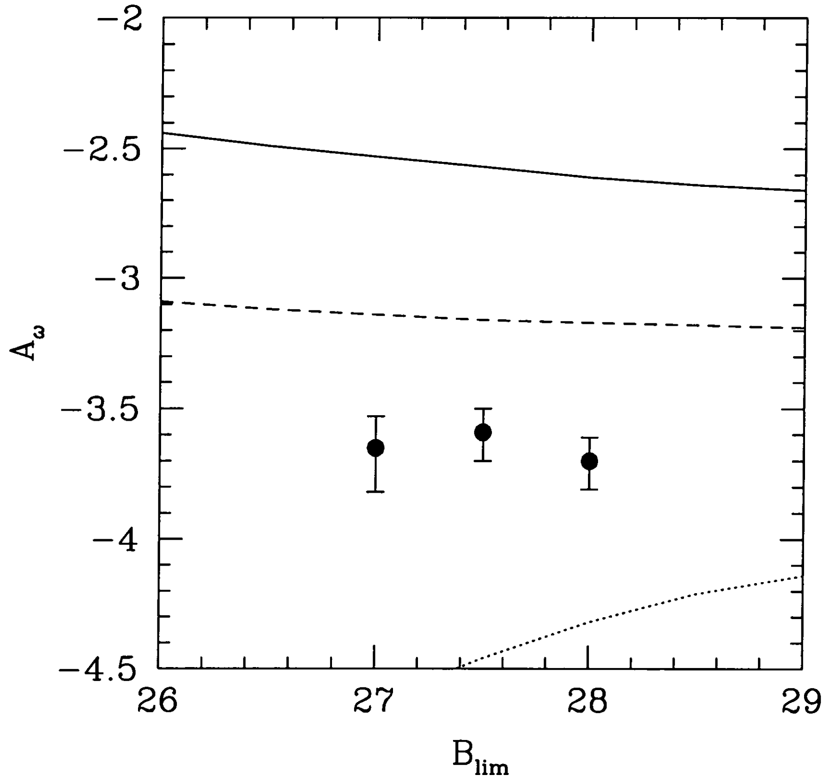

Figure 5.12: Our $B-$ selected correlation amplitudes compared with the predictions of two variants of our clustering model, one comprising only galaxies with $2 < z < 3$ (solid line) and one including dilution by foreground galaxies (dotted line). Additionally, the predictions of the standard $\epsilon = -1.2$ evolutionary model are shown (dashed line). For all these models, $q_0 = 0.05$ and $r_0 = 4.3h^{-1}$ Mpc.

Are the measurements of high clustering amplitudes for Lyman-break galaxies compatible with the *low* clustering amplitudes found in the WHDF at $B \sim 28$? These low A_ω's measured at $B \sim 28$ are, as we have seen, more consistent with $\epsilon \sim 0$ than with the constant co-moving clustering amplitudes found for Lyman-break galaxies (which require $\epsilon \sim -1$). To test this, we will isolate a sample of galaxies from our models with redshifts in the same range as the Lyman-break galaxies and compute their expected correlation amplitudes.

In Figure 5.12 we show the fitted amplitude of the angular correlation function at one degree (A_ω) plotted as a function of sample limiting magnitude. Our data is shown as the filled circles. The dashed line shows the predictions of the standard co-moving model previously presented in Figure 5.11; the solid line shows the expected correlations for a sample of $2.6 \lesssim z \lesssim 3.4$ galaxies if their clustering was constant in co-moving co-ordinates *and there were no foreground galaxies to dilute the measured clustering amplitudes.* The dotted line shows how the clustering amplitude indicated by the solid line is reduced by the presence of foreground objects. This has been calculated by making the simple assumption that the fraction f of objects in the models which are not Lyman-break galaxies (defined in terms of their redshift range) are unclustered, reducing A_ω by an amount f^{-2}, in the same way in which the presence of stars cause a reduction of A_ω as outlined in Section 5.2.1. This calculated A_ω is necessarily a lower limit; foreground galaxies of course are not unclustered. Given that the dotted line is below our A_ω measurements at $B \sim 28$ we conclude that we cannot rule out a population of objects with correlation lengths of $r_0 \sim 4h^{-1}$ Mpc at $z \sim 2-3$.

However, there is an important qualification to the above comments. In order to measure ϵ from deep pencil-beam surveys like those outlined above one must make the assumption that the high-redshift objects found in such catalogues have counterparts in the local Universe. Identifying such objects is becoming increasingly important as it is already apparent locally that galaxy clustering is a sensitive function not only of morphology but also of star-formation history and intrinsic luminosity; by extension, is likely that different classes of galaxies could have different clustering evolution.

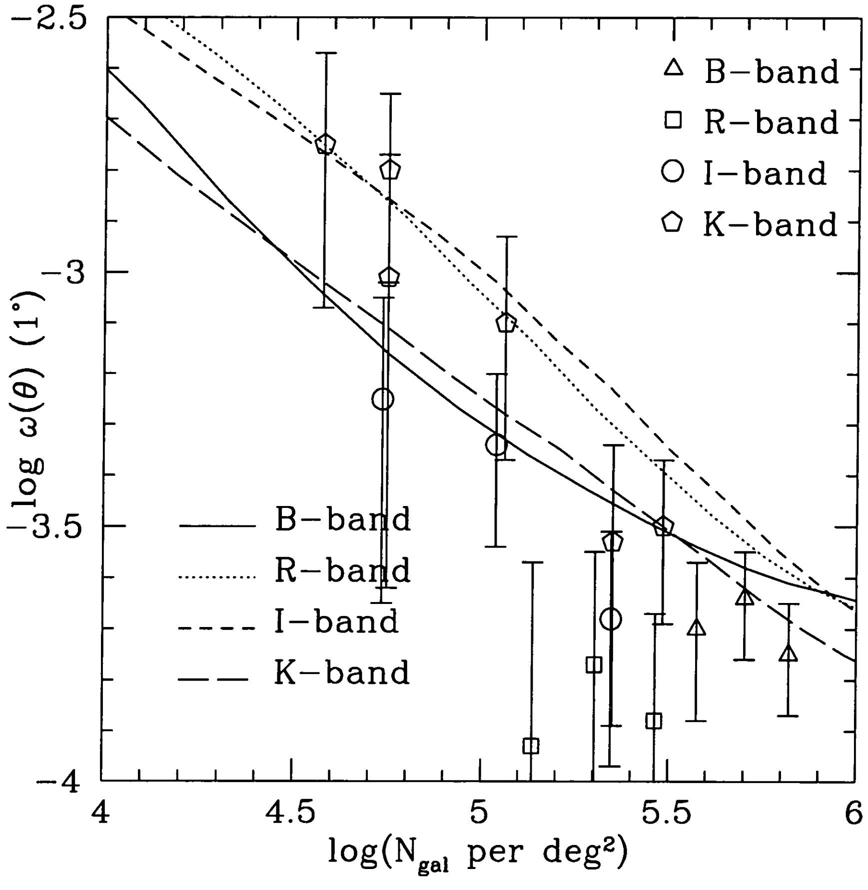

Figure 5.13: Surface density of galaxies against measured correlation amplitude for all data points in all bandpasses in the WHDF (open symbols) and for the predictions of the model (lines). The model shown has $\epsilon = 0$ and $r_0 = 4.3h^{-1}$ Mpc.

5.4.4 A consistent picture?

In Figure 5.13 we present all our clustering measurements in the WHDF, in each of the four bandpasses we have investigated, as well as the predictions of the evolutionary models discussed in the previous section, for $\epsilon = 0$, $r_0 = 4.3h^{-1}$ Mpc and $q_0 = 0.05$. In order to allow all the measurements to be plotted on the same figure, A_ω is shown as a function of galaxy surface density. Because of the small size of our survey, we compute this quantity from the model prediction for both data and models; as this model reproduces the observed number counts this is not problematic. However, because the WHDF field of view is limited, the range in number densities covered is correspondingly small, as a consequence of the difficulties of determining correlation function amplitudes at brighter magnitudes with small samples. However, this Figure does highlight some important differences between galaxy evolution as viewed in each of the different bandpasses.

For example, at low number density ($\log N_{gal} \sim 3$), the $K-$band predicted correlation amplitudes are below the predictions of the other bandpasses. This is because at $z < 1$, the $K-$band $k + e$ correction is *negative*, resulting in a higher median redshift for $K-$ selected galaxy populations than is seen in the $B-$ selected samples. However, by $\log N_{gal} \sim 4.5$, in the $B-$band evolution has raised the median redshift, causing the amplitude of the correlation function to drop below the $K-$band value. Throughout the range of the graph, the R and I scaling relations remain above the B and K curves due to the combination of mild evolution and positive $(k + e)$ corrections, at least until $z \sim 2$.

The error bars on our measurements of A_ω are larger than the differences between the model predictions in each of the bandpasses, so we are unable to test in detail this scenario . However, in the scheme outlined above, the different correlation amplitudes produced in each of the bandpasses at a fixed galaxy surface density are *entirely* a product of the different redshift distributions. But we have already seen how the morphological mix changes dramatically from B to K even while the median redshift of the sample stays approximately constant. Furthermore, we have discussed how local redshift surveys find correlation amplitudes for ellipticals $3 - 4$ times higher than for spirals, and we might expect this to be reflected in our measurements of A_ω in different bandpasses at fixed N_{gal}. There is no evidence for such a difference in the current dataset.

Finally, we examine the behaviour of the correlation function at the faintest limits. Earlier works conducted in $B-$ selected surveys suggest that by $B \sim 26$,

A_ω ceases to decline and reaches a constant, limiting value (Metcalfe et al. 1995; Roche et al. 1996; Roche et al. 1993); more recently, Brainerd & Smail (1998) claimed to have detected a similar phenomenon at $I_{med} \sim 24$. Our own correlation amplitudes at $B \sim 28$ are currently the deepest measurements of A_ω in *any* work; they are also the bandpass which probes to the faintest magnitudes. Here, A_ω does not scale with sample limiting magnitude as we find in our measurements at brighter magnitudes in other bandpasses; we will now describe how this effect can be understood in terms of the models presented here.

The scaling relation for our $B-$band evolutionary model, shown in Figure 5.11 and Figure 5.13, flattens off at very high number densities (log($N_{gal} \sim 6\,\mathrm{deg}^{-2}$) and faint magnitudes ($B \sim 28$). At these limits, the relationship between number density and median redshift levels off. This is a consequence of the steep faint-end slope luminosity function assumed for spiral galaxies and also of the reduction of the cosmological volume element at higher redshift. Moreover, in Figure 5.13 it is apparent that this effect is most pronounced in the $B-$band, and is *not* seen in the redder bandpasses. Our $B-$band correlations reach depths at which the correlation function is expected to behave in this manner, and indeed from $B = 27.0$ to $B = 28.0$ we do observe that the amplitude of A_ω is almost independent of magnitude.

Brainerd & Smail (1998) claim to have observed a flattening in the correlation amplitude at $I_{med} \sim 24$, corresponding to $\log N_{ngal} \sim 5$ and therefore at lower number densities than our $B-$ band catalogue. Based on our models, we would not expect the $I-$band correlation function at the magnitude limit of Brainerd & Smail's survey to level off, and indeed the $I-$band correlation amplitudes measured by *our* survey continues to decline. Furthermore, given the large scatter in the $I-$band measurements of A_ω we suggest that further measurements with larger surveys — preferably of the size of Postman et al.'s work

— are required to establish if indeed such a levelling off-behaviour occurs.

5.5 Conclusions and summary

In this Chapter we have measured the angular correlation function $\omega(\theta)$ in the William Herschel Deep Field to very faint limiting magnitudes. We have compared these measurements to the predictions of our evolutionary models and investigated what implications these measurements have for the growth of clustering in the Universe.

Our main conclusions are as follows:

- Our measured correlation amplitudes in BRI are lower than the predictions of our $q_0 = 0.05$, $\epsilon = 0$ non-evolving model. A model which incorporates luminosity evolution as described in Chapter 2 provides a better fit to the observations, implying that the underlying galaxy redshift distribution is more extended than the non-evolving prediction.

- Clustering amplitudes measured for our $K-$ selected samples are consistent with the predictions of our $q_0 = 0.05$, $\epsilon = 0$ evolutionary model. In K this model, which has a steep slope for the elliptical IMF, has a less extended redshift distribution than the standard model with a Salpeter IMF. This agreement indicates that our K- band clustering measurements are consistent with our K- selected samples having a low median redshift.

- If our luminosity evolution models provide an accurate description of the underlying galaxy redshift distributions (as is suggested by spectroscopic surveys at brighter magnitudes), then this indicates (for $q_0 = 0.05$) that our data is consistent with a scenario in which the growth of galaxy clustering is stable in proper co-ordinates. At the sub-Mpc scales which our survey probes, this rate of clustering growth is in accordance with the predictions of hierarchical models of galaxy formation.

- In the B-band, where our survey reaches $B < 28^m$, our measured clustering amplitude is constant for the three bins we have measured. We interpret this as arising from the reduction of cosmological volume at high redshift; this means that at very faint magnitude levels the median redshift of our survey sample ceases to increase.
- We have carried out a detailed set of simulations to assess the size of the errors on our correlation function measurements and to provide more realistic error estimates. We find that apparent discrepancies between our work and that of other authors can be explained in terms of an underestimation of statistical errors.
- The high correlation amplitudes of the Lyman-break galaxies are shown to be *consistent* with the low clustering amplitudes recorded by our survey at $B \sim 28$.

Chapter 6

Conclusions

6.1 Preliminaries

In this Thesis we have investigated the evolutionary histories of the field galaxy population. Principally we have studied photometric properties and spatial distributions of faint field galaxies. Our data comprises very deep optical and infrared images of a high galactic latitude region. These observations have been compared to the predictions of pure luminosity evolution models; in this Chapter we will summarize our main results and place our findings in the broader context of the work of other authors described in the introductory Chapter.

6.2 Photometric evolution

Throughout this Thesis we have carried out several detailed studies of both the colour distributions and number counts of the faint galaxy population. We have focussed in particular on the properties of near-infrared selected galaxy samples. To interpret our results we have employed a pure luminosity evolution (PLE) model. In this framework, present-day galaxy luminosity functions are combined with population synthesis models and a suitable cosmology (in our case, one in which $\Lambda = 0$ and $q_0 = 0.05, q_0 = 0.5$) in order to predict the colours and apparent magnitudes of the faint field galaxy population.

Number counts from our three near-infrared surveys of the WHDF are consistent with the predictions of a low q_0, non-evolving model. However, our deep, wide-field Calar Alto data and our analysis of the HDF-S and HDF-N fields shows evidence of a small amount of evolution in the faintest ($H > 22$) bins. In Chapter 2 we also saw that in order to match the observed K-band redshift distributions with our models we had to assume a steep ($x = 3$) slope for the stellar initial mass function. Our Calar Alto number counts are also fitted by a "disappearing dwarf" $q_0 = 0.5$ model. Neither this model or the low-q_0 model require a steep slope to the faint end of the galaxy luminosity function in order to match the observed number counts.

Infrared-selected optical-infrared colour distributions for all three surveys find a significant lack of extremely red, evolved galaxies. This deficiency is consistent with a small amount of on-going star-formation having occurred in such systems. However, these colour distributions do not allow us to convincingly rule out merging as an alternative explanation of the observations.

6.3 Clustering evolution

We have analysed clustering properties of galaxies in the WHDF using the two-point angular correlation function $\omega(\theta)$. This quantity has been measured in $BRIK$ bandpasses for a range of magnitude-limited samples of galaxies. Using the predicted redshift distributions from our evolutionary models we have derived expected correlation amplitudes (assuming $q_0 = 0.05$) and compared these with our observations. This comparison revealed that the observations are consistent with a model in which the growth of galaxy clustering is approximately fixed in proper co-ordinates, if our model redshift distributions are correct. Following the parametrisation of Groth & Peebles (1977), this corresponds to $\epsilon \sim 0$. At the sub-Mpc scales which our survey probes, this is the amount of clustering evolution expected from the predictions of hierarchical models of galaxy formation (Baugh et al. 1998a).

As noted in the previous Section, for elliptical galaxies we adopt an IMF slope of $x = 3$. This produces a less extended K-selected redshift distribution than the standard model incorporating a Salpeter IMF. Therefore, if the growth of galaxy clustering is accurately described by $\epsilon = 0$ (as our work indicates), and if $q_0 = 0.05$, then our high K-selected clustering measurements are consistent with K- selected samples having a low median redshift. This is in accordance with similar conclusions drawn from brighter spectroscopic work (Cowie, Songaila, & Hu 1996).

In the B- band, our deepest bandpass, our measured clustering amplitudes are independent of sample limiting magnitude, indicating a constant median redshift for these samples. We interpret these results as being indicative of the much slower increase in the cosmological volume element at high redshift.

We have carried out a detailed set of simulations designed to assess the size of the errors on our correlation function measurements and to provide more realistic error estimates. This is essential given the small size of our field. We find that apparent discrepancies between our work and that of other authors can be explained in terms of an underestimation of statistical errors.

6.4 Concluding remarks

In the introductory Chapter we described work by Madau et al. (1996) and others which suggested that the peak in the global star-formation rate occurred at intermediate ($1 < z < 2$) redshifts. However, as we explained, the effects of dust at $z > 2$ (Campos & Shanks 1997) has made the decline in star-formation rate at $z > 2$ less than certain.

In the models presented in this Thesis, the star-formation rate increases rapidly from $z = 0$ to $z = 1$; thereafter it is approximately constant. This is consistent with the revised star-formation history recently presented in Steidel et al. (1998b), derived from a large sample of B- band drop-outs. As we have seen, our PLE model incorporating this star-formation history is remarkably successful in reproducing the observed properties of the faint galaxy population, at least for $q = 0.05$, $\Lambda = 0$ cosmologies. For $q_0 = 0.5$ models an extra population of dwarf galaxies must be added in order to fit the B- counts successfully. If this population has the same clustering properties as normal galaxies then the $\epsilon = 0$ clustering model incorporating them does not match the clustering observations.

As we have seen, the low median redshift found for K-selected galaxy surveys provides a stringent test of PLE models. A low median redshift for these surveys is also consistent with the predictions of hierarchical models of galaxy formation (Kauffmann & Charlot 1998). Although it appears that our model clustering predictions and the predictions of these hierarchical models agree, it is not clear that both models share similar star-formation histories. This present work does not directly address this issue; the surveys described here are primarily infrared-selected, which are dominated by early-type galaxies. The contribution of these galaxies to the total integrated star-formation history of the Universe (as depicted by Madau's diagram) is small.

Accurately determining the star-formation history of the Universe, together with measuring galaxy clustering for large samples over wide areas with large spectroscopic (and to fainter limits) and photometric redshift surveys selected in both optical and infrared wavelengths will be the task of the new generation of

8-metre telescopes.

6.5 Future prospects

In 1999, the last year of the millennium, several surveys will begin which aim to dramatically increase our knowledge of the local and distant Universe. One is the Visible Infrared Multi-Object Spectrograph or VIRMOS project, which aims to measure redshifts for 150,000 galaxies from $z = 0$ to $z = 4$ using two of the European Southern Observatory's Very Large Telescopes. Preparatory imaging for this survey will start in January 1999 using the Canada-France-Hawaii-Telescope's wide-field mosaic CCD camera, the largest CCD camera yet constructed. The photometric database for the VIRMOS project alone will be an important resource. It will cover 25 square degrees of sky in five bandpasses from the optical to the infrared and contain over a million galaxies with sub-arcsecond imaging. This will allow detailed studies of the evolution of the galaxy correlation function and galaxy luminosity function out to very high redshifts. Meanwhile, the Sloan and 2DF surveys will provide a detailed census of our local Universe and provide an important reference point against which to measure evolutionary changes observed in faint galaxy samples.

Early in the next century the NASA are planning to launch a successor to the Hubble Space Telescope. Named the Next Generation Space Telescope (NGST) this mission will be optimised for operation at near-infrared wavelengths and it will be placed in an orbit far from Earth to minimize the sky background. With its six to eight metre mirror the NGST will be able to directly observe the epoch of galaxy formation and to provide definitive answers to some of the questions posed in this Thesis.

Bibliography

Abraham R. G., Tanvir N. R., Santiago B. X., Ellis R. S., Glazebrook K., Van Den Bergh S., 1996, MNRAS, 279, L47

Allington-Smith J. et al., 1994, PASP, 106, 983

Babul A., Rees M. J., 1992, MNRAS, 255, 364

Bahcall J. N., Soneira R. M., 1980, ApJ, 238, L17

Barger A., Cowie L. L., Trentham N., Fulton E., Hu E., Songaila A., 1998, AJ, in press

Barrow J. D., Sonoda D. H., Bhavsar S. P., 1984, MNRAS, 210, 19P

Baugh C. M., Benson A. J., Cole S., Frenk C. S., Lacey C. G., 1998a, astro-ph/9811222

Baugh C. M., Cole S., Frenk C. S., 1996, MNRAS, 282, L27

Baugh C. M., Cole S., Frenk C. S., Lacey C. G., 1998b, ApJ, 498, 504

Baugh C. M., Gardner J. P., Frenk C. S., Sharples R. M., 1996, MNRAS, 283, L15

Baum W., 1962, in G.C.McVittie , ed, IAU Symposium 15, Problems of Extra-galactic Research. Macmillan

Benson A., Baugh C., Frenk C., Cole S., 1999, MNRAS, in preparation

Bershady M. A., Lowenthal J. D., Koo D. C., 1998, ApJ, 505, 50

Bertin E., Arnouts S., 117, 393

Bertin E., Dennefeld M., 1997, A&A, 317, 43

Bond J. R., Kaiser N., Cole S., Efstathiou G., 1991, ApJ, 379, 440

Bower R. G., 1991, MNRAS, 248, 332

Brainerd T. G., Smail I., 1998, ApJ, 494, L137

Brainerd T. G., Smail I., Mould J., 1994, MNRAS, 244, 408

Brinchmann J. et al., 1998, ApJ, 499, 112

Broadhurst T. J., Ellis R. S., Glazebrook K., 1992, Nat, 355, 55

Broadhurst T. J., Ellis R. S., Shanks T., 1988, MNRAS, 235, 827

Bruzual G., Charlot S., 1993, ApJ, 405, 538

Bruzual G., Kron R. G., 1980, ApJ, 241, 25

Campos A., 1997, ApJ, 488, 606

Campos A., Shanks T., 1997, MNRAS, 291, 383

Carlberg R. G., Cowie L. L., Songaila A., Hu E. M., 1997, ApJ, 484, 538

Carlberg R. G. et al., 1998, astro-ph/9805131

Casali M. M., Hawarden T., 1992, in JCMT-UKIRT Newsletter, p. 33

Cole S., 1991, ApJ, 367, 45

Cole S., Aragon-Salamanca A., Frenk C., Navarro J., Zepf S., 1994, MNRAS, 271, 781

Coleman G. D., Wu C.-C., Weedman D. W., 1980, ApJS, 43, 393

Colin P., Carlberg R. G., Couchman H. M. P., 1997, ApJ, 490, 1

Colless M., 1998, in Wide Field Surveys in Cosmology, 14th IAP meeting held May 26-30, 1998, Paris. Publisher: Editions Frontieres. ISBN: 2-8 6332-241-9, p. 77., p. 77

Colless M., Ellis R. S., Taylor K., Hook R. N., 1990, MNRAS, 244, 408

Connolly A. J., Csabai I., Szalay A. S., Koo D. C., Kron R. G., Munn J. A., 1995, AJ, 110, 2655

Couch W. J., Jurcevic J. S., Boyle B. J., 1993, MNRAS, 260, 241

Cowie L. L., Gardner J. P., Hu E. M., Songaila A., Hodapp K. W., Wainscoat R. J., 1994, ApJ, 434, 114

Cowie L. L., Songaila A., Hu E. M., 1996, AJ, 112, 839

Davis M., Peebles P. J. E., 1983, ApJ, 267, 465

Djorgovski S. et al., 1995, ApJ, 438, L13

Doel A., Andrews N., Dunlop C., Buscher D., Myers R., Major J., Sharples R., McCracken H., 1999, in preparation

Driver S. P., Fernandez-Soto A., Couch W. J., Odewahn S. C., Windhorst R. A., Phillips S., Lanzetta K., Yahil A., 1998, ApJ, 496, L93

Driver S. P., Windhorst R. A., Griffiths R. E., 1995, ApJ, 453, 48

Efstathiou G., Bernstein G., Katz N., Tyson J., Guhathakurta P., 1991, ApJ, 380, L47

Ellis R. S., 1997, ARA&A, 35, 389

Ellis R. S., Colless M., Broadhurst T., Heyl J., Glazebrook K., 1996, MNRAS, 280, 235

Ferguson H., McGaugh S., 1995, ApJ, 440, 470

Gardner J., Cowie L., Wainscoat R., 1993, ApJ, 415, L9

Gardner J. P., 1995, ApJS, 98, 441

Gardner J. P., Sharples R. M., Carrasco B. E., Frenk C. S., 1996, MNRAS, 282, L1

Giallongo E., D'Odorico S., Fontana A., Cristiani S., Egami E., Hu E., McMahon R. G., 1998, AJ, 115, 2169

Giavalisco M., Steidel C. C., Adelberger K. L., Dickinson M. E., Pettini M., Kellogg M., 1998, ApJ, 503, 543

Glazebrook K., Ellis R., Colless M., Broadhurst T., Allington-Smith J., Tanvir N., 1995a, MNRAS, 273, 157

Glazebrook K., Ellis R., Santiago B., Griffiths R., 1995b, MNRAS, 275, L19

Glazebrook K., Peacock J. A., Miller L., Collins C. A., 1995c, MNRAS, 275, 169

Governato F., Baugh C. M., Frenk C. S., Cole S., Lacey C. G., Quinn T., Stadel J., 1998, Nat, 392, 359

Griffiths R. E. et al., 1994, ApJ, 437, 67

Groth E. J., Peebles P. J. E., 1977, ApJ, 217, 385

Guhathakurta P., Tyson J. A., Majewski S. R., 1990, ApJ, 357, L9

Gunn J. E., 1995, American Astronomical Society Meeting, 186, 4405

Gwyn S., Hartwick F. D. A., 1996, ApJ, 468, L77

Hamilton A. J. S., 1993, ApJ, 417, 19

Hauser M. G., Peebles P. J. E., 1973, ApJ, 185, 757

Heydon-Dumbleton N. H., Collins C. A., Macgillivray H. T., 1989, MNRAS, 238, 379

Hogg D. W. et al., 1998, AJ, 115, 1418

Huang J., Cowie L. L., Gardner J. P., Hu E. M., Songaila A., Wainscoat R. J., 1997, ApJ, 476, 12

Hudon J. D., Lilly S. J., 1996, ApJ, 469, 519

Hunt L. K., Mannucci F., Testi L., Migliorini S., Stanga R. M., Baffa C., Lisi F., Vanzi L., 1998, AJ, 115, 2594

Infante L., Pritchet C., Quintana H., 1986, AJ, 91, 217

Infante L., Pritchet C. J., 1995, ApJ, 439, 565

Jenkins A. et al., 1998, ApJ, 499, 20

Jones L. R., Fong R., Shanks T., Ellis R. S., Peterson B. A., 1991, MNRAS, 249, 481

Jones L. R., Shanks T., R. F., 1987, in High Redshift and Primeval Galaxies, eds Bergeron J., Kunth D., Rocca-Volmerange B., Tran Thanh Van J., Editions Frontieres, Gif-sur-Yvette, p.29, p. 29

Kauffmann G., Charlot S., 1998, MNRAS, 297, L23

Kauffmann G., Colberg J. M., Diaferio A., White S. D. M., 1998, astro-ph/9809168

Kauffmann G., Guiderdoni B., White S., 1994, MNRAS, 267, 981

Koo D. C., 1985, AJ, 90, 418

Koo D. C., Gronwall C., Bruzual G., 1993, ApJ, 415, L21

Koo D. C., Kron R. G., 1992, ARA&A, 30, 613

Koo D. C., Szalay A. S., 1984, ApJ, 282, 390

Kron R. G., 1980, ApJS, 43, 305

Landy S. D., Szalay A. S., 1993, ApJ, 412, 64

Lanzetta K. M., Yahil A., Fernandez-Soto A., 1996, Nat, 381, 759

Le Fevre O., Crampton D., Felenbok P., Monnet G., 1994, aap, 282, 325

Le Fèvre O. et al., 1998, in Wide Field Surveys in Cosmology, 14th IAP meeting held May 26-30, 1998, Paris. Publisher: Editions Frontieres. ISBN: 2-8 6332-241-9, p. 327., p. 327

LeFevre O., Hudon D., Lilly S., Hammer F., Tresse L., 1996, ApJ, 461, 534

Lidman C. E., Peterson B. A., 1996, MNRAS, 279, 1357

Lilly S. et al., 1998, ApJ, 500, 75

Lilly S. J., Cowie L. L., Gardner J. P., 1991, ApJ, 369, 79

Lilly S. J., Le Fevre O., Crampton D., Hammer F., Tresse L., 1995a, ApJ, 455, 50

Lilly S. J., Tresse L., Hammer F., Crampton D., Le Fevre O., 1995b, ApJ, 455, 108

Limber D. N., 1953, ApJ, 117, 134

Ling E. N., Barrow J. D., Frenk C. S., 1986, MNRAS, 223, 21P

Loh E. D., Spillar E. J., 1986, ApJ, 303, 154

Loveday J., Maddox S. J., Efstathiou G., Peterson B. A., 1995, ApJ, 442, 457

Madau P., 1995, ApJ, 441, 18

Madau P., Ferguson H. C., Dickinson M. E., Giavalisco M., Steidel C. C., Fruchter A., 1996, MNRAS, 283, 1388

Maddox S. J., Efstathiou G., Sutherland W. J., Loveday J., 1990a, MNRAS, 243, 692

Maddox S. J., Efstathiou G., Sutherland W. J., Loveday J., 1990b, MNRAS, 242, 43P

Maddox S. J., Sutherland W. J., Efstathiou G., Loveday J., Peterson B. A., 1990c, MNRAS, 247, 1P

Marquardt D., 1963, Journal of the Society for Industrial and Applied Mathematics

Metcalfe N., Fong R., Shanks T., 1995, MNRAS, 274, 769

Metcalfe N., Fong R., Shanks T., Kilkenny D., 1989, MNRAS, 236, 207

Metcalfe N., Shanks T., Campos A., Fong R., Gardner J. P., 1996, Nat, 383, 263

Metcalfe N., Shanks T., Campos A., McCracken H., Gardner J., Fong R., 1998, MNRAS, in preparation

Metcalfe N., Shanks T., Fong R., Jones L. R., 1991, MNRAS, 249, 498

Metcalfe N., Shanks T., Fong R., Roche N., 1995, MNRAS, 273, 257

Mo H. J., Fukugita M., 1996, ApJ, 467, L9

Mobasher B., Rowan-Robinson M., Georgakakis A., Eaton N., 1996, MNRAS, 282, L7

Moustakas L. A., Davis M., Graham J. R., Silk J., Peterson B. A., Yoshii Y., 1997, ApJ, 475, 445

Neuschaefer L. W., Windhorst R. A., Dressler A., 1991, ApJ, 382, 32

Oke J. B. et al., 1994, Proc. SPIE, 2198, 178

Peebles J., 1980, The Large-Scale Structure of the Universe. Princeton

Peebles P. J. E., 1973, ApJ, 185, 413

Peebles P. J. E., 1982, ApJ, 263, L1

Pei Y., 1992, ApJ, 395, 130

Pence W., 1976, ApJ, 203, 39

Peterson B. A., Ellis R. S., Efstathiou G., Shanks T., Bean A. J., Fong R., Zen-Long Z., 1986, MNRAS, 221, 233

Peterson B. A., Ellis R. S., Kibblewhite E. J., Bridgeland M. T., Hooley T., Horne D., 1979, ApJ, 233, L109

Phillipps S., Fong R., Fall R. S. E. S. M., Macgillivray H. T., 1978, MNRAS, 182, 673

Postman M., Lauer T. R., Szapudi I., Oegerle W., 1998, ApJ, 506, 33

Press W. H., Flannery B. P., Teukolsky S. A., Vetterling W. T., 1986, Numerical Recipes. Cambridge University Press

Press W. H., Schechter P., 1974, ApJ, 187, 425

Rauscher B., Sharples R., McCracken H. J., Peletier R., EMIR report

Reid I. N., Yan L., Majewski S., Thompson I., Smail I., 1996, AJ, 112, 1472

Rocca-Volmerange B., Guiderdoni B., 1990, MNRAS, 247, 166

Roche N., Eales S., 1998, astro-ph/9803331

Roche N., Eales S., Hippelein H., 1998, MNRAS, 295, 946

Roche N., Eales S., Hippelein H., Willott C., 1998, astro-ph/9809271

Roche N., Shanks T., Metcalfe N., Fong R., 1993, MNRAS, 263, 360

Roche N., Shanks T., Metcalfe N., Fong R., 1996, MNRAS, 280, 397

Sandage A., 1988, ARA&A, 26, 561

Saracco P., Iovino A., Garilli B., Maccagni D., Chincarini G., 1997, AJ, 114, 887

Sawicki M. J., Lin H., Yee H. K. C., 1997, AJ, 113, 1

Scalo J. M., 1986, Fundamentals of Cosmic Physics, 11, 1

Schade D., Carlberg R. G., Yee H. K. C., Lopez-Cruz O., Ellingson E., 1996a, ApJ, 465, L103

Schade D., Lilly S. J., Crampton D., Hammer F., Le Fevre O., Tresse L., 1995, ApJ, 451, L1

Schade D., Lilly S. J., Le Fevre O., Hammer F., Crampton D., 1996b, ApJ, 464, 79

Shanks T., 1989, in The Galactic and Extragalactic Background Radiation, IAU

Shanks T., Fong R., Ellis R., 1980, MNRAS, 192, 209

Shanks T., Metcalfe N., Fong R., MCCracken H. J., Campos A., Gardner J. P., 1998, in ASP Conf. Ser. 146: The Young Universe: Galaxy Formation and Evolution at Intermediate and High Redshift, p. 102

Shanks T., Stevenson P. R. F., Fong R., Macgillivray H. T., 1984, MNRAS, 206, 767

Shanks T., Tanvir N. R., Major J. V., Doel A. P., Dunlop C. N., Myers R. M., 1992, MNRAS, 256, 29P

Simard L., Pritchet C. J., 1998, ApJ, 505, 96

Smoot G. F. et al., 1992, ApJ, 396, L1

Soneira R. M., Peebles P. J. E., 1978, AJ, 83, 845

Steidel C. C., Adelberger K. L., Dickinson M., Giavalisco M., Pettini M., Kellogg M., 1998a, ApJ, 492, 428

Steidel C. C., Adelberger K. L., Giavalisco M., Dickinson M., Pettini M., 1998b, astro-ph/9811399

Steidel C. C., Giavalisco M., Pettini M., Dickinson M., Adelberger K. L., 1996, ApJ, 462, L17

Steidel C. C., Hamilton D., 1993, AJ, 105, 2017

Stevenson P. R. F., Shanks T., Fong R., Macgillivray H. T., 1985, MNRAS, 213, 953

Tanvir N. R. et al., 1991, MNRAS, 253, 21P

Teplitz H. I., Gardner J. P., Malumuth E. M., Heap S. R., 1998, ApJ, 507, L17

Thompson R. I., Rieke M., Schneider G., Hines D. C., Corbin M. R., 1998a, ApJ, 492, L95

Thompson R. I., Storrie-Lombardi L. J., Weymann R. J., Rieke M. J., Schneider G., Stobie E., Lytle D., 1998b, astro-ph/9810285

Tinsley B. M., 1972, ApJ, 178, 319

Tucker D. L. et al., 1997, MNRAS, 285, L5

Tyson J., Seitzer P., 1988, ApJ, 335, 552

Tyson J. A., Jarvis J. F., 1979, ApJ, 230, L153

Tyson J. A., Seitzer P., Weymann R. J., Foltz C., 1986, AJ, 91, 1274

Villumsen J. V., Freudling W., Da Costa L. N., 1997, ApJ, 481, 578

Vogt N. P., Forbes D. A., Phillips A. C., Gronwall C., Faber S. M., Illingworth G. D., Koo D. C., 1996, ApJ, 465, L15

Wainscoat R. J., Cowie L. L., 1992, AJ, 103, 332

White S. D. M., Frenk C. S., 1991, ApJ, 379, 52

White S. D. M., Frenk C. S., Davis M., 1983, ApJ, 274, L1

White S. D. M., Rees M. J., 1978, MNRAS, 183, 341

Williams R. E. et al., 1996, AJ, 112, 1335

Woods D., Fahlman G. G., 1997, ApJ, 490, 11

Yan L., McCarthy P. J., Storrie-Lombardi L. J., Weymann R. J., 1998, ApJ, 503, L19

Zehavi I., Riess A. G., Kirshner R. P., Dekel A., 1998, ApJ, 503, 483

Zepf S. E., 1997, Nat, 390, 377